Final Report
NSG-3025
USC 53-4514-8122

UNIVERSITY OF SOUTHERN CALIFORNIA

SCHOOL OF ENGINEERING

"BASIC NOISE RESEARCH PROGRAM"

SHEAR LAYER STRUCTURE OF A LOW SPEED JET

by

Robert Allen Petersen

FINAL REPORT TO:

NATIONAL AERONAUTICS AND SPACE ADMINISTRATION
LEWIS RESEARCH CENTER

June 28, 1974 to December 31, 1975

John Laufer
Principal Investigator

DEPARTMENT OF AEROSPACE ENGINEERING

(NASA-CR-146810) SHEAR LAYER STRUCTURE OF A LOW SPEED JET Ph.D. Thesis. Final Report, 28 Jun. 1974 - 31 Dec. 1975 (University of Southern Calif.) 171 p HC $6.75 CSCL 20D
N76-21429
Unclas
G3/34 21585

SHEAR LAYER STRUCTURE OF A LOW SPEED JET

by

Robert Allen Petersen

This Report was Written in

Partial Fulfillment of the

Requirements for the Degree

DOCTOR OF PHILOSOPHY

Under the Direction of Professors

R.E. Kaplan and John Laufer

and Under the Financial Support of

National Aeronautics and Space Administration
Lewis Research Center

February 1976

ABSTRACT

A series of measurements of near field pressures and turbulent velocity fluctuations were made in a low speed jet with a Reynolds number near 50,000 in order to investigate more quantitatively the character and behavior of the large scale structures and their interactions with each other.

Time averaging techniques and simple eduction techniques were insufficient to detect interactions between vortex structures beyond a diameter downstream. More sophisticated detection schemes were investigated with little success. Finally, the near field measurements were modelled according to the "vortex pairing" hypothesis to deduce the distribution of pairings along the jet axis and the variances about the mean locations.

The hodograph plane description of turbulence was explored in some detail, and a complex correlation quantity was synthesized which has useful properties for turbulence in the presence of mean shear.

TABLE OF CONTENTS

Chapter Page

1 INTRODUCTION

2 FACILITIES

3 STATISTICAL TECHNIQUES

4 PRELIMINARY JET SURVEY

5 NEAR FIELD MEASUREMENTS

6 MIXING LAYER STATISTICS

7 EVIDENCE FOR PAIRING HYPOTHESIS

Appendix

A X-WIRE CALIBRATION

LIST OF TABLES

LIST OF FIGURES

1. INTRODUCTION

1.1 Motivation

There is substantial evidence that there are large scale organized structures within the jet mixing layer. They are large scale in the sense that they are spatially coherent over a major fraction of the mixing layer thickness, and they are organized in the sense that their associated flow field is induced by inherently compact regions of concentrated vorticity. We feel that their existence has been adequately demonstrated at least during the initial stages of shear layer growth. We are interested in the contribution of these structures to turbulent mixing beyond the potential core as well as their contribution to the radiated noise.

In the past, the interpretation has been that noise is radiated by local fluctuations of momentum flux, and the resultant acoustic radiation is the linear superposition of these purely local contributions. It would be of great interest to examine whether these fluctuating momentum fluxes are associated primarily with interactions between the large structures. There are a number of observations that seem to suggest this possibility:

1) From flow visualization experiments conducted by Browand, Chu, and Laufer (1975), it is apparent that at least for moderate Reynolds numbers (Re < 10,000), the initial growth of the jet mixing layer is dominated by vortex ring structures that coalesce as they interact. The coalescence is sudden and results in an explosive production of smaller scale radial and azimuthal flow. Both the exchange of momentum between rings and the radial accelerations are plausible noise mechanisms.

2) A collection of total acoustic power spectra compiled by Howes (1960) and discussed in detail below, indicates that for large Reynolds numbers and moderate Mach numbers (Re > 100,000 and M > .6) the spectral peak scales with jet diameter independent of viscous, compressible, or thermal influences. This scaling is consistent with the observed ring structures since their size and spacing is intrinsically related to jet geometry.

3) Recent shear layer measurements of Winant and Browand (1974) indicate large intermittent increases in momentum flux associated with passage of vortex structures and with interaction of adjacent structures. Intermittent momentum fluxes, after all, are the contributing noise sources according to the Lighthill (1952) formulation.

4) Powell (1964) has shown that when a free vortex ring stretches it radiates acoustically like a dipole, with a far field amplitude proportional to the second time derivative of its Kelvin impulse. The kinematics of vortex coalescence suggests that impulse is exchanged between rings. In that case vortex coalescence would appear acoustically like a longitudinal quadrupole radiator.

Although this evidence is at best indicative, it suggests a conclusive experiment: if it were possible to detect vortex coalescence with probes in the shear layer or near field of the jet, then simultaneous directional far field measurements would establish any causal relationship. Detecting vortex coalescence in a high Reynolds number compressible jet using a small number of probes is a formidable task. Consequently, this work is an investigation of techniques aimed at detecting such events.

1.2 Parametric survey of jet noise spectra

For the present investigation a low speed (100 fps), moderate Reynolds number (50,000) jet was selected. This size jet seemed a reasonable compromise in that flow visualization experiments have demonstrated vortex pairing up to a Reynolds number of about 10,000, while noise measurements have been made on jets down to a Reynolds number of about 100,000. Since the jet is essentially incompressible at these low speeds, hot wires respond directly to flow velocity.

The question remains whether measurements made on a low Reynolds number, incompressible jet are applicable to a high speed, compressible jet. A way of approaching this question is to examine jet noise scaling with Reynolds number and Mach number. Such a parametric survey of total acoustic power spectra, derived from a compilation by Howes (1960) are summarized in figures 1 through 4. The spectra represent a wide range of geometries and experimental conditions. They include both air jets and engines, exhausting through both parallel and convergent nozzles. The test facilities included reverberant chambers (Fitzpatrick and Lee, 1952; Tyler and Perry, 1954; Waterhouse and Berendt, 1958), as well as free field surroundings (Lee, 1953; Rollin, 1958; and Howes, 1960).

Figures 1 and 2 show acoustic power spectra as a function of jet Strouhal number (fD/U_e), with Reynolds number (U_eD/ν) as the parameter, for both moderate and high Mach number jets (M = .60 and .90). Exit Mach number ,based on local sonic velocity, is the parameter in figures 3 and 4 for both moderate and high Reynolds number jets (Re = .20 and 2.0 E 6). The power spectra are normalized to unity

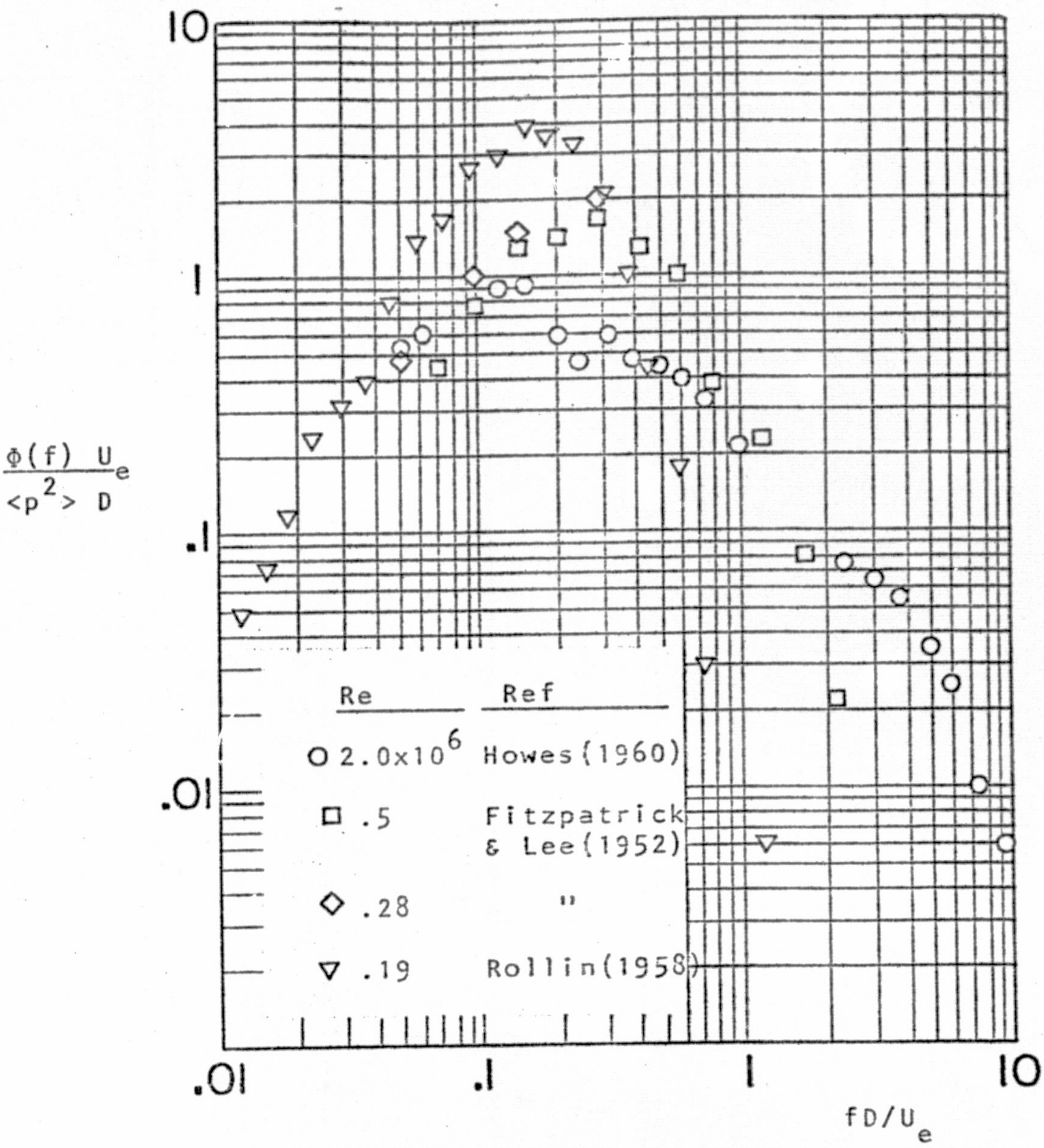

Figure 1. Parametric study of jet noise spectra $M = .6$ and $Re = .2\text{-}2.0\times10^6$

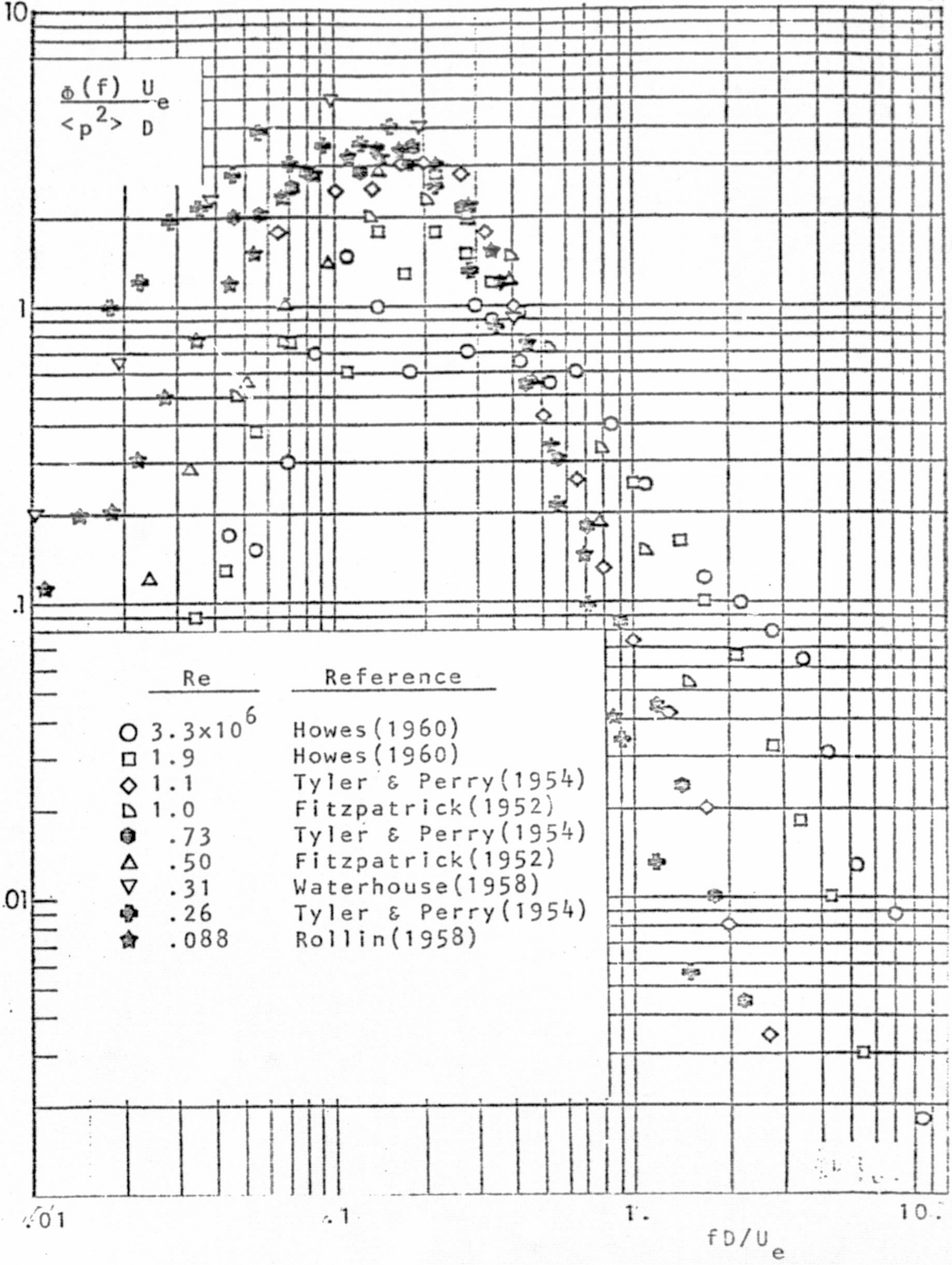

Figure 2. Parametric study of jet noise spectra

$M = .9$ and $Re = .09\text{-}3.3 \times 10^6$

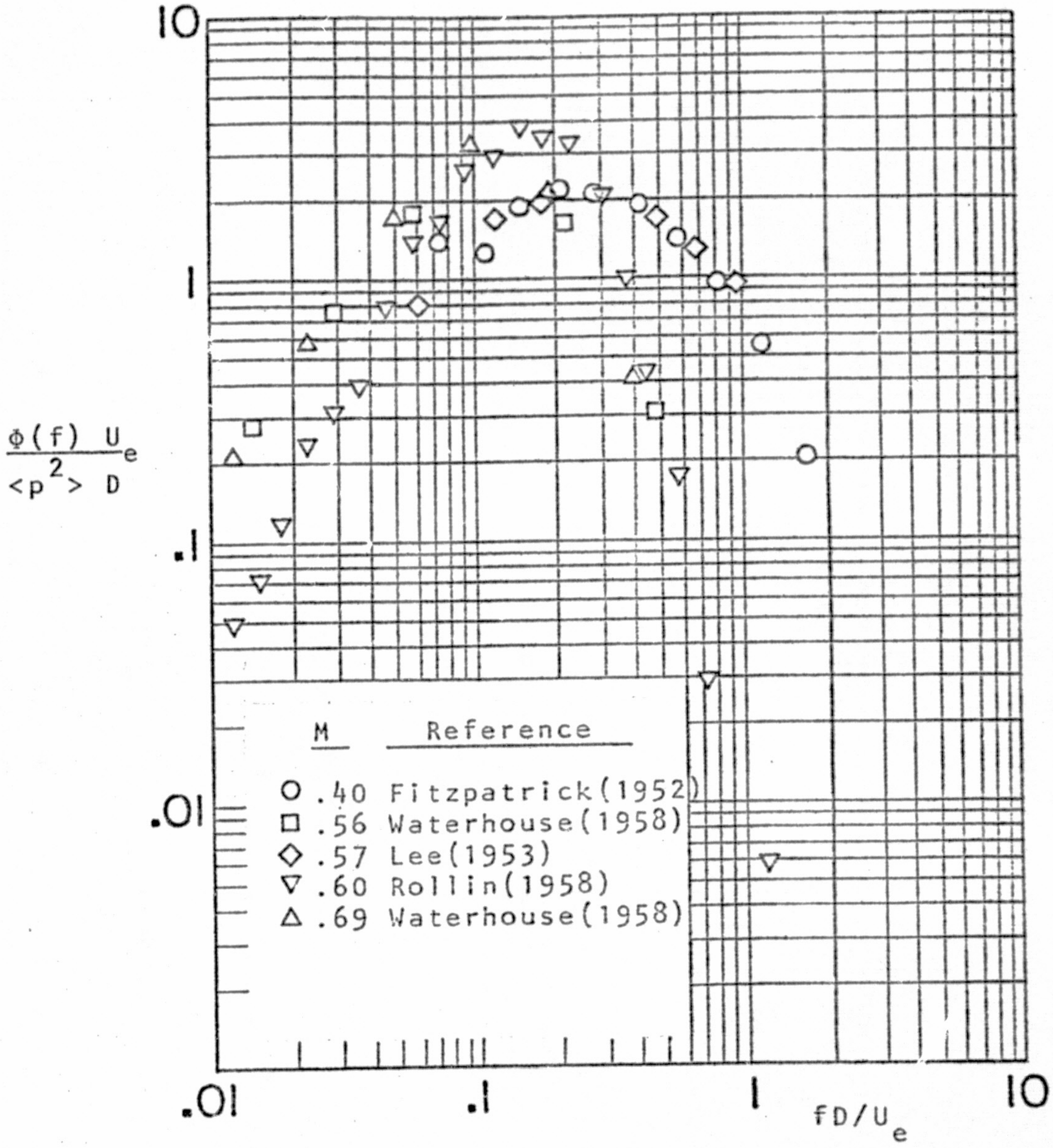

Figure 3. Parametric study of jet noise spectra

$Re = .2\times10^6$ and $M = .4-.7$

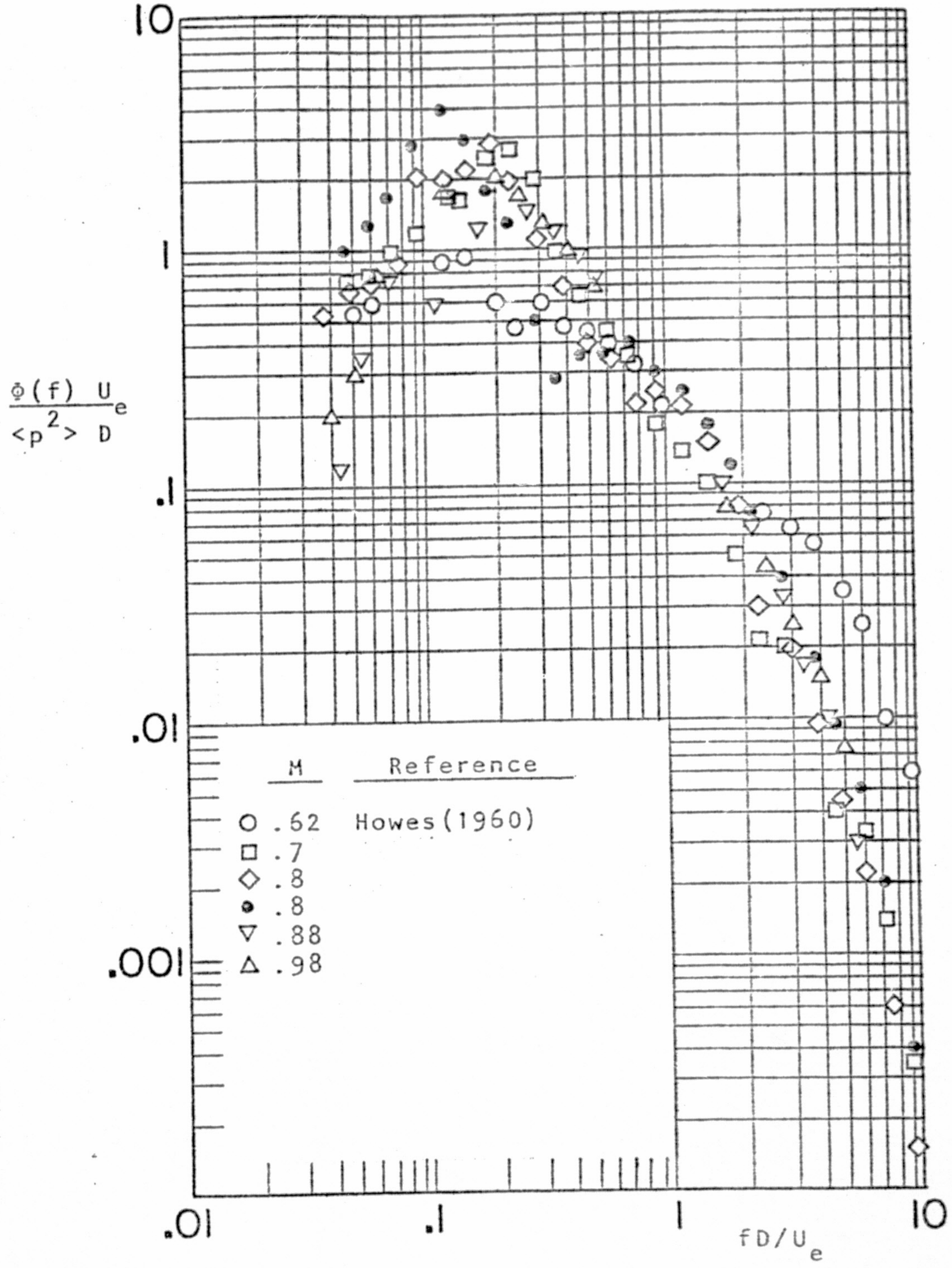

Figure 4. Parametric study of jet noise spectra

$Re = 2.\times10^6$ and $M = .6 - 1.0$

area, so the relative levels are less important than the locations of the spectral peaks, and the slopes of the high and low frequency asymptotes. The effect of Reynolds number on spectral similarity is clear: there is a consistent viscous influence in that the high frequency asymptotes flatten with increasing Reynolds number while the low frequency asymptotes steepen, implying a transfer of acoustic energy from larger to shorter wavelengths. The value of the spectral peak, however, remains relatively constant with Reynolds number. If the spectral peak represents the characteristic time scale of the radiating jet structure, the implication is that the structure scales independently of Reynolds number. Figures 3 and 4 indicate that the effect of compressibility on acoustic scaling is less certain. There does appear to be some shift towards smaller scales at the lowest Mach numbers. This may simply indicate a departure from purely quadrupole radiation, for instance by acoustic sources interior to the nozzle as has been often suggested for explaining departures from the eight power law at low velocities.

1.3 Review of flow visualization studies

The existence of vortex rings and their mutual interaction in a low Reynolds number (10,000) jet were observed as early as 1955 by A. B. C. Anderson. He was interested in the physics of pipe tones produced in a jet issuing through an orifice plate, and used a double spark shadowgraph to visualize the jet structure. He observed that the primary vortex shedding frequency produced the fundamental pipe tone, and the pairing mechanism excited various subharmonics.

Rockwell and Niccolls (1972) recognized vortex pairing as the mechanism for the shear layer growth in the potential core region of a two-dimensional jet. They used the hydrogen bubble technique to visualize the flow, and included a Reynolds number range of 1860 to 10,800. Both symmetrical and asymmetrical pairings were observed.

That vortex pairing is the mechanism responsible for shear layer growth was amplified by Winant and Browand (1974) in their flow visualization work with a two-dimensional, turbulent mixing layer. They injected dye into the mixing layer formed between two parallel streams of water moving at different speeds. In particular they observed that the onset of pairing marked the transition of the shear layer from laminar to turbulent growth and that vortex pairing inherently produces linear shear layer spreading.

Similar dye studies by Browand, Chu, and Laufer (1975) in a circular water jet demonstrated that the spreading rate of the mixing layer can be increased by artificially driving the jet core at a subharmonic of its initial instability. Forcing seems to increase the spatial coherence of the flow and perhaps hastens the transition from laminar to turbulent spreading. This study was conducted at jet Reynolds numbers up to 15,000.

1.4 Review of mixing layer measurements

Flow visualization studies have proved invaluable in providing a physical model but are fundamentally qualitative techniques, and are confined to low and moderate Reynolds number flows. Quantitative turbulence measurements in moderate to high Reynolds number jets have until recently lacked a direct connection with the flow visualization work.

J. C. Laurence (1955) compiled a statistical survey of the mixing layer of a 3.5-inch circular jet. He used single wire and x-wire probes to measure moments and correlations at varying radial positions along the potential core and transitional mixing regions of the jet. The correlation measurements were used to define lateral and longitudinal length scales, which were observed to be insensitive to Reynolds number over a range 37,500 to 350,000, and insensitive to Mach number over a range .2 to .7. He found that the peak turbulence level occurs at the radial position $r/D = .5$.

Hot wire measurements by Bradshaw, Ferris, and Johnson (1964) indicated that irrotational velocity fluctuations outside the jet near the nozzle are due to large scale eddies within the mixing layer. From measurements of the correlation $<v^2w^2>/<v^2><w^2>$ they determined that the radial (v) and azimuthal (w) components are generally either in phase or in antiphase, implying that the flow associated with the eddies is not axisymmetric, but that the large eddies are characterized by random swirl evenly distributed so that the mean $<vw> = 0$.

Mollo-Christensen (1967) was interested in the contribution of the large eddies to the near field static pressure fluctuations. He placed microphones at the edge of a low speed jet and made both broadband and narrowband crosscorrelations between microphones that were separated axially and azimuthally along the potential core. From these measurements he postulated an intermittent, spatially regular structure with random phase. Furthermore the frequency of the regular structure was observed to shift discontinuously to its own subharmonic with downstream distance. From comparisons between crosscorrelations of narrowband pressure signals which had been filtered about different center frequencies, it was inferred that the transfer of energy within a wave packet from smaller to larger wavelengths was a nonlinear process.

Mollo-Christensen's observations were supported by Ko and Davies (1971) who made hot wire measurements inside the potential core of a low speed jet over a velocity range $U_e = 165 - 335$ fps. They found that the velocity fluctuations in the core were characterized by a relatively narrow power spectrum and a mean convection speed ratio $U_c/U_e = .60 - .65$, independent of exit speed U_e. The convection speed is so low that the velocity fluctuations could not be carried by the local mean flow, implying that the fluctuations are induced from within the mixing layer. As a spatially integrated effect the induced fluctuations would be most sensitive to organized structure even if the latter did not dominate the turbulence locally.

Crow and Champagne (1971) investigated the influence of initial conditions on the mixing layer structure over a jet Reynolds number range 62,000 to 124,000. Their jet plenum chamber was driven acoustically at various harmonic resonances, introducing fluctuations into the core with amplitudes as large as 5% of the exit velocity U_e. When the jet was driven at a Strouhal number of .3, which had been observed to be the dominant mode, the resulting disturbance, when filtered around St = .3, grew exponentially in the first couple of diameters downstream, reached a peak level near the end of the potential core, and thereafter declined. Crow and Champagne interpreted this in terms of a linear wave instability followed by non-linear saturation. However when they drove the jet at a Strouhal number of .6, the .3 Strouhal disturbance was driven more efficiently than at its own wave number. This apparent subharmonic amplification is consistent with vortex pairing, which can also account for the observed non-linear saturation. Crow and Champagne found the jet shear layer to be non-dispersive at frequencies greater than Strouhal .3, the dominant mode, and dispersive at smaller wavenumbers, raising a possible connection between dispersion and the observed concentration of turbulent energy about a dominant Strouhal number.

Lau, Fisher, and Fuchs (1972) identified the mean structure within a circular jet shear layer at axial position x/D=2 as a series of vortex rings moving at a mean speed $U_c/U_e = .6$, and with a mean spacing of 1.2 diameters. They used x-wire probes to measure velocity fluctuations inside the core, in the entrainment region, and inside the mixing layer of their jet which was operated at a Reynolds number of 210,000. The vortex model was deduced from phase relationships between radial and axial velocity fluctuations measured in the entrainment and core regions. Correlation measurements between a microphone and the hot wire probes indicated that vortex passage manifests itself in the near field as a static pressure trough. In particular they proved for the first time that the near field pressure fluctuations are produced by the passage of vortex rings through the mixing layer.

Davies et al (1974) were particularly interested in obtaining quantitative information about the interactions between vortex rings that are so evident in the flow visualization studies. Arrays of single and x-wire probes were placed inside the mixing layer and space-time correlation as well as eduction techniques were utilized to bring out the interactions. At moderate Reynolds numbers (Re = 20,000) they were successful in detecting one or two coalescences near the nozzle exit, which they called "laminar" pairings. However vortex pairings could not be detected further downstream than a couple of diameters, and even the laminar pairings could not be detected at higher Reynolds numbers (Re = 200,000). From flow visualization studies of their own, using smoke jets, and individual smoke rings, strong azimuthal structure was demonstrated. In particular there were occasional events that appeared like secondary, radial jets that are possible noise mechanisms.

1.5 Scope of present work

This study is an investigation of techniques aimed at detecting organized, intermittent events inside the mixing layer of a moderate Reynolds number circular jet using a small number of probes. Particular emphasis is placed on pressure signatures in the near field, and on the use of conditional statistics to describe the mixing layer turbulence.

The investigation was only moderately successful in detecting interactions between vortex rings, and was unsuccessful in detecting any organized structure at all in the transitional mixing region. However, based on the measurements, an indirect case can be made supporting the vortex pairing hypothesis as the mechanism responsible for the linear spreading of the jet shear layer just as it is the mechanism for free mixing layer growth. Chapter 7 is a summary of this evidence, while overall conclusions appear in chapter 8. The actual near field and mixing layer measurements are discussed separately in chapters 5 and 6, respectively. The special statistical techniques used in obtaining these measurements are discussed in chapter 3. Chapter 4 contains a preliminary survey of the jet in terms of profiles of mean velocity and rms turbulence, which is intended to establish the model jet as normal. The problems and procedures involved in calibrating the x-wire probes are discussed in the appendix.

2. FACILITIES

2.1 Model jet

Most of the experiments described in this investigation have been carried out in the low speed model jet shown in figure 5. It consists of a vacuum cleaner blower, a settling chamber with damping screens, and a circular nozzle. The contraction ratio of the nozzle is 36:1 and the exit diameter is 1.00 inch. The maximum attainable exit velocity is 220 fps, but most of the work was carried out at velocities near 100 fps, corresponding to a Reynolds number (U_eD/ν) of 52,000.

The exit boundary layer is laminar and its thickness is measured to be .05 diameter. The exit plane mean velocity profile is flat to better than 0.5% and the exit plane turbulence level is 0.3% of exit velocity U_e. This relatively high level was considered satisfactory for the type of measurements planned.

2.2 Instrumentation

Mean velocity measurements were made with a total pressure Pitot tube. Depending on the application, total pressure was either read from a BETZ manometer, or recorded

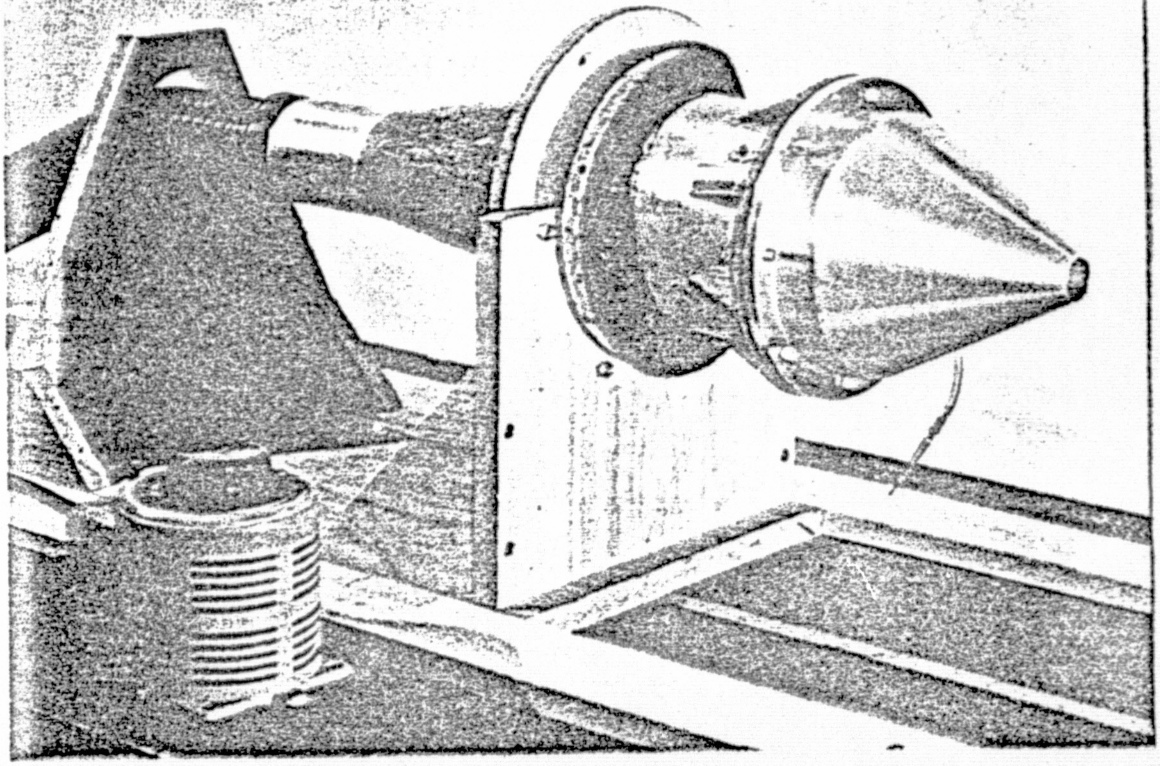

Figure 5. The model jet.

off of a VALIDYNE Model DP15TL capacitance type differential pressure transducer.

Near field pressure measurements were made using BRUEL & KJAER model 4138 eighth-inch capacitor microphones with a nominal sensitivities of -80 dB re 1 volt/μbar, and a nominal bandwidth of 20 Hz to 150 kHz at levels below 170 dB. Microphone output was amplified through a BRUEL & KJAER model 2618 cathode follower.

Turbulence measurements were made with constant temperature hot wire anemometers. The wires were .0001 inch diameter Platinum, with an aspect ratio of about 400. The bridge circuit, shown in figure 6, was designed for an overheat ratio of 2. In the presence of a large ratio of mean velocity to r.m.s. fluctuating velocity, the wire responds to the velocity component parallel to the mean flow. Consequently, a single wire is sufficient to record axial velocity fluctuations. However, an x-wire probe is needed to decompose the turbulence into axial and radial components. It is necessary to determine calibration polynomials in order to obtain orthogonal velocity components from the outputs of the two wires. As particular care must be exercised in deriving and measuring these polynomials, the calibration procedure is described in detail in the appendix.

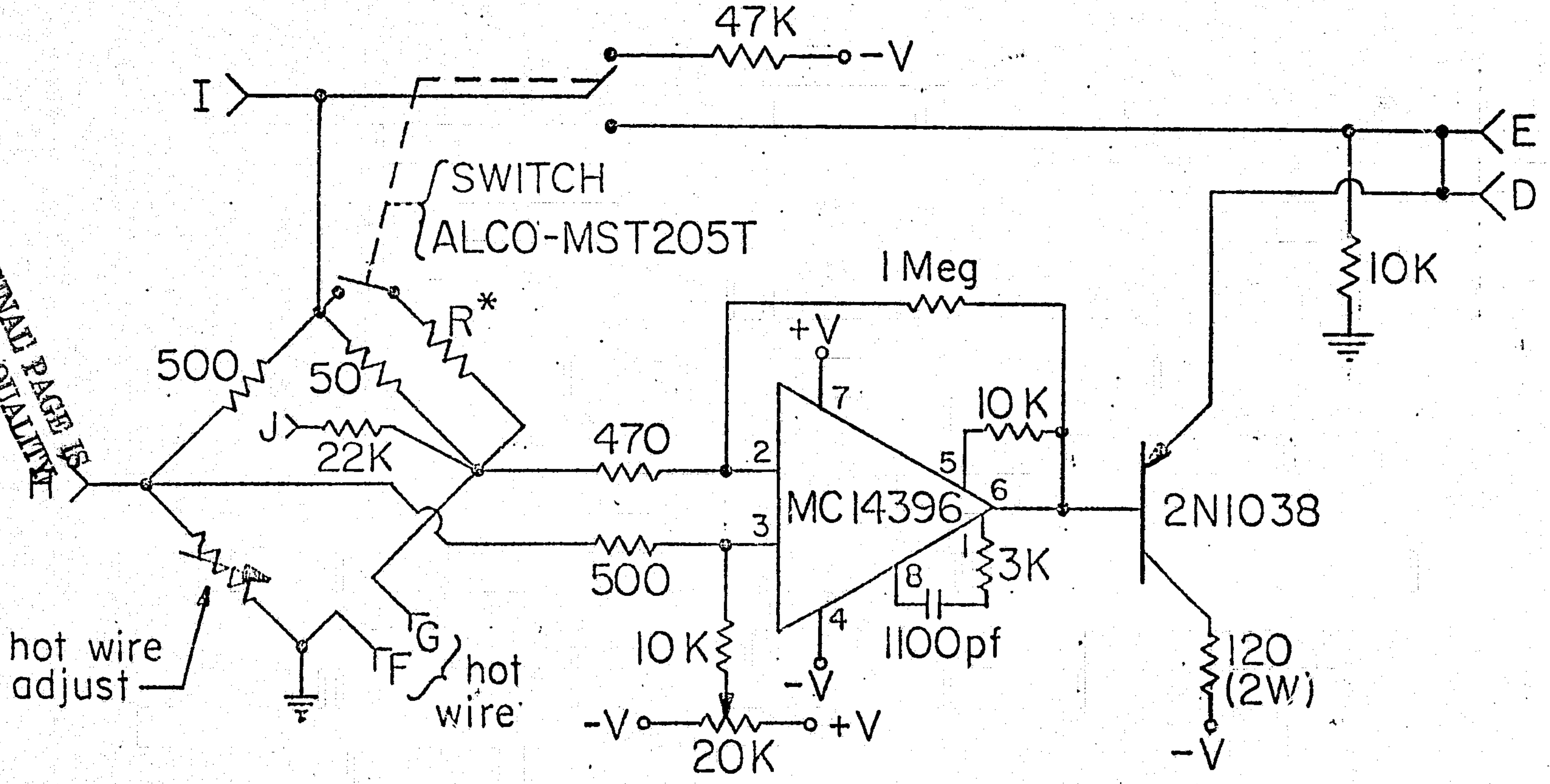

Figure 6. Hot wire bridge: schematic diagram

A traversing mechanism of our own design was used for radial positioning of probes, and the model jet itself was moved for axial positioning. When greater precision was required, a PRIOR three-dimensional micropositioner was used; with this instrument a probe can be positioned to within .1 mm.

2.3 Digital equipment

Most of the correlations and educted signals were measured with a HEWLETT-PACKARD model 3721A digital correlator. This device has the capabilities of generating autocorrelations, crosscorrelations, and histographs, as well as signal recovery provided an appropriate trigger can be generated. The correlator has a sampling rate that is adjustable in steps from 1 Hz to 1 MHz. It was used for most of the near field pressure measurements and for the single wire turbulence measurements.

For measurements of joint statistics, we chose to linearize the x-wire signals digitally. The raw signals were digitized using a subsystem of our own design, described by Jentes (1975). It consists of 16 sample and hold circuits and an analog to digital converter interfaced with an INTERDATA 5 programmable minicomputer. The maximum sampling rate in microseconds is 100 + 20*(# channels). the digitized record is written onto disk, then transferred to digital tape.

A PDP 10 general purpose computer was used for most of the data reduction and analysis.

3. STATISTICAL TECHNIQUES

3.1 Correlation techniques

Correlation measurements have been the traditional means of determining time and length scales inside mixing layers. The two point space-time correlation is defined:

$$<e_1(\underline{x})e_2(\underline{y})>(\tau) = \lim_{T\to\infty} \frac{1}{2T} \int_{-T}^{T} e_1(\underline{x},t)e_2(\underline{y},t+\tau)\,dt \qquad (1)$$

and in general contains information about the spectral content of the turbulence, the coherence length scales, and the mean convection speed of the turbulence.

The coordinate system is defined in figure 7, and will be referred to throughout this paper.

3.2 Two point eduction

Two point eduction is a type of flow visualization, and consists of generating a trigger pulse from conditions at one point in the flow field and sampling the flow at a second location after some fixed time delay relative to the pulse. When the sampling is done over an ensemble, the average as a function of time delay is referred to as the "educted" signal; a number of educted signals at various positions in the flow field determine the relationship

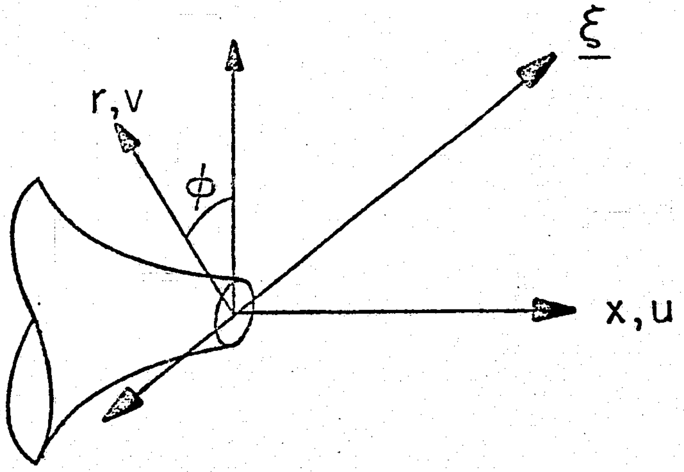

Figure 7. Coordinate system

between any spatial structures in the field and the triggering condition at the triggering location.

The most difficult aspect of two point eduction is in choosing an appropriate triggering condition. There are two main considerations in selecting the condition:

1) it should be exclusively characteristic of the flow field structure one is trying to visualize,
2) and it must be temporally narrow to provide a precise time reference.

The trigger must be derived from some feature of the basic random signals. The simplest form of such a criterion is signal slope and level, in much the same manner as an oscilloscope trigger signal is formed. However such an inclusive condition can bring out only very regular structures. In such cases eduction provides little more information than conventional crosscorrelations. The real advantage in eduction techniques lies in detecting 'subprocesses', such as interactions between regular structures, that are intermittent, and lack a consistent phase relationship to the mean structure. Obviously, the better the subprocesses are understood, the easier it is to choose an exclusive trigger condition.

3.3 Joint statistics

One potentially useful method of generating a trigger condition, borrowed from pattern recognition, is to study statistical properties of the flow at a point as it appears in the hodograph plane, with the intent of identifying subprocesses. The conceptual basis for such an approach derives from the nature of the dynamical equations. If the flow is incompressible, the pressure term in the equation of motion can be expressed as a volume integral over the flow field at that instant. Consequently, the field equation involves only first differences in time, which implies that the entire field at a given time is completely described by the entire field at the previous instant in time. However, if the field is known only at a single point in space, it is uncertain how the field at that point will change over the next instant. It is plausible, however, that the *statistics* of the field at a point depends only on the statistics of the field at that point in the previous instant. Our approach has been to measure various first differences of the field at a point, and to attempt to associate them with deterministic subprocesses.

The two joint statistical quantities of interest are the joint probability density $\underline{P}(u,v)$ and the joint conditional probability density $\underline{Q}(\tilde{u},\tilde{v};u,v)$. The joint probability density, when suitably normalized, is the fraction of time the field occupies position (u,v) in the hodograph plane. Measured $P(u,v)$ is independent of the sampling rate provided the sampling is faster than the power spectral bandwidth of the turbulence. The joint conditional probability density represents the probability that the field would occupy position $(\tilde{u},\tilde{v})$ after time step "dt", provided it started from position (u,v). The dependence of $Q(\tilde{u},\tilde{v};u,v)$ on sampling rate will be discussed later in this section.

The proper normalizations for the probability densities are

$$\iint_{-\infty}^{\infty} P(u,v)\ dudv = 1 \tag{2a}$$

and

$$\iint_{-\infty}^{\infty} Q(\tilde{u},\tilde{v};u,v)\ dudv = 1 \tag{2b}$$

Time averages of the turbulence can be computed as moments of the joint probability distribution. Specifically, mean velocities are defined

$$< q_i > \equiv \iint_{-\infty}^{\infty} q_i\ P(u,v)\ dudv \tag{3}$$

variances are defined

$$\sigma_i^2 \equiv \iint_{-\infty}^{\infty} \{ q_i^2 - \langle q_i \rangle^2 \} P(u,v)\, dudv \qquad (4)$$

and stresses are defined

$$\langle q_i q_j \rangle \equiv \iint_{-\infty}^{\infty} q_i q_j\, P(u,v)\, dudv \qquad (5)$$

The correlation coefficient is defined

$$R \equiv \{ \langle uv \rangle - \langle u \rangle \langle v \rangle \} / u'v' \qquad (6)$$

where q ', the rms fluctuating component, is

$$q_i' \equiv \sqrt{\sigma_i^2} \qquad (7)$$

The hodograph plane description of turbulence is not a new technique. It was used for example by Liepmann and Laufer (1947). However, joint probability densities are difficult measurements using analog equipment, and it hasn't been until the advent of the high speed digital computer that these kinds of measurements have become practical. In practice they are among the easiest calculations to program. Pre-recorded recorded x-wire signals $e_1(t)$ and $e_2(t)$ are converted to parallel digital records using sample and hold circuits. The records are linearized using an appropriate calibration scheme, resulting in parallel records of axial (u) and radial (v) velocities. The hodograph plane is divided into the desired number of cells (in this case 2500 cells) of dimension $\Delta u \times \Delta v$, and each occurrence of (u,v) within the range $(u_m \pm \Delta u/2, v_n \pm \Delta v/2)$ generates a unique index associated with cell (u_m, v_n). By counting the number of such occurrences a joint histogram is generated, which is normalized according to equation (2a) to produce the joint probability density.

At the same time the joint probability is being generated it is easy to look forward one time step "dt" to measure the average forward differences $\langle du \rangle$, $\langle dv \rangle$, $\langle du^2 \rangle$, $\langle dv^2 \rangle$, $\langle dudv \rangle$ associated with each cell (u,v). These average differences describe the mean properties of the joint conditional probabilities $Q(\tilde{u},\tilde{v};u,v)$. For example the vector $(u+\langle du \rangle, v+\langle dv \rangle)$ defines the mean conditional $(\langle u \rangle, \langle v \rangle)$ associated with the cell (u,v). The tensor T_{ij} defined by

$$T_{ij}(u,v) \equiv \left(\langle dq_i dq_j \rangle - \langle dq_i \rangle \langle dq_j \rangle\right)_{(u,v)} \qquad (8)$$

can be diagonalized to describe the principal axis rotation and second moments of each $Q(\tilde{u},\tilde{v};u,v)$. This use of forward differences to estimate Q is illustrated in figure 8, and saves the prohibitive amount of computer storage that would be necessary to directly measure the conditional probability associated with each cell. Note that the magnitudes of first and principal second moments depend directly on the magnitude of the time step dt; however if dt is sufficiently small, the direction of the first moment and the principal

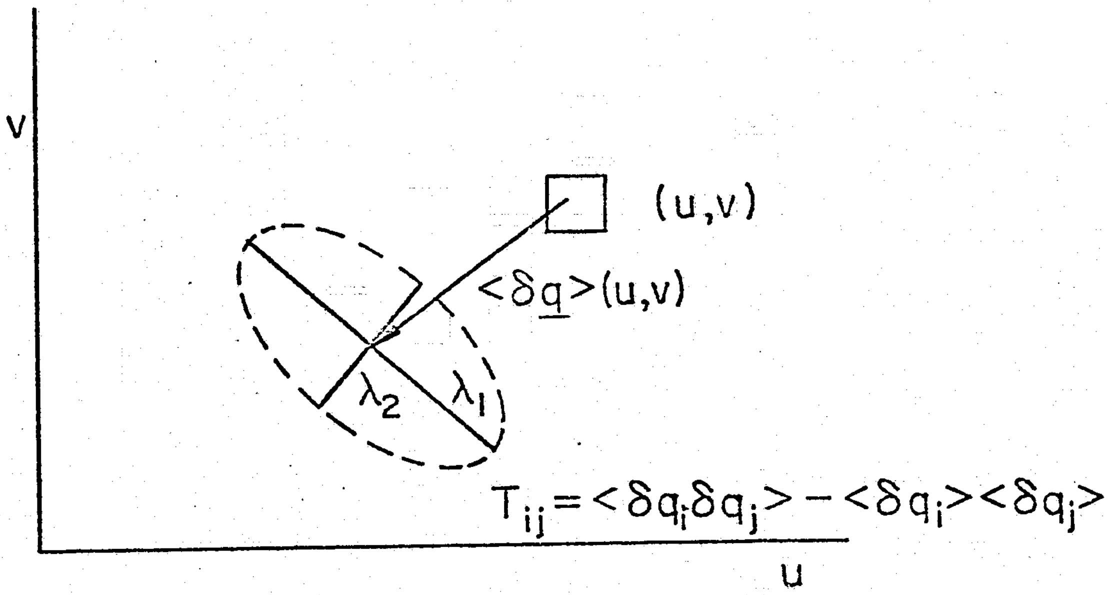

Figure 8. Synthesis of joint conditional probability density from forward differences.

axis rotation of T_{ij} are invariant with sampling rate.

From figure 8, the vector $\{<du>,<dv>\}_{(u,v)}$ can be visualized as describing the 'drift' of the mean of the conditional probability density, while the tensor $T_{ij}(u,v)$ describes its 'diffusion'. If the magnitude of the drift is much larger than the eigenvalues of the diffusion, the motion associated with that position in the hodograph plane can be considered largely deterministic; if it is the other way around the motion can be considered noise driven. Based on this concept, one can formulate the time averaged drift:

$$\mathrm{DRIFT} \equiv \iint_{-\infty}^{\infty} \sqrt{<dq_k><dq_k>} \quad P(u,v)\ dudv \tag{9}$$

and diffusion

$$\mathrm{DIFFUSION} \equiv \iint_{-\infty}^{\infty} \sqrt{T_{kk}}\ P(u,v)\ dudv \tag{10}$$

Then the ratio DIFFUSION/DRIFT is a measure of the overall 'noisiness' of the measured velocity field.

3.4 Complex correlation

There are two general properties of the drift vectors $d\underline{q}(u,v)$ that are predictable. First, the drift will be largest in magnitude from cells (u,v) farthest from the mean $(<u>,<v>)$. Second, they will generally point radially towards the probability peak, in the sense that the most

ORIGINAL PAGE IS
OF POOR QUALITY

probable drift will be towards the most probable state. However, if there is some intermittent subprocess present with an associated, repeatable trajectory in the hodograph plane there ought to be some deviation from purely stochastic behavior.

It would be useful to formulate quantities sensitive to such subprocesses. There are two cumulative quantities that come to mind: the integrals

$$\iint_{-\infty}^{\infty} \underline{q} \cdot \langle d\underline{q} \rangle \ P(u,v) \ dudv \tag{11a}$$

and

$$\iint_{-\infty}^{\infty} \underline{q} \times \langle d\underline{q} \rangle \ P(u,v) \ dudv \tag{11b}$$

The magnitude of the latter integral in comparison with the former provides a quantitative measure of how much "swirl" is present among the drift vectors.

In addition to being possible pattern recognition tools, integrals (11) have an interesting physical interpretation in terms of a generalized autocorrelation. If complex velocity W(t) is defined

$$W(t) \equiv u(t) - jv(t) \tag{12}$$

an the complex, scalar autocorrelation $\langle WW^* \rangle(\tau)$ can be defined

$$<WW^*>(\tau) = \{<uu> + <vv>\}(\tau) + j\{<uv> - <vu>\}(\tau) \tag{13}$$

The one dimensional autocorrelation $<uu>(\tau)$ can be expressed directly in terms of measured forward differences $<du>(u,v)$:

$$<uu>(\tau) = \iint_{-\infty}^{\infty} u\,\{u + <du>(\tau)\}\,P(u,v)\,du\,dv \tag{14}$$

where time step τ is the time delay. From equations (13) and (14)

$$\begin{aligned} <WW^*>(\tau) &= \iint_{-\infty}^{\infty} \underline{q}\cdot\{\underline{q} + <d\underline{q}>(\tau)\}P(u,v)\,du\,dv \\ &\quad + j\iint_{-\infty}^{\infty} \underline{q}\times\{\underline{q} + <d\underline{q}>(\tau)\}\,P(u,v)\,du\,dv \\ &= \left((u')^2 + (v')^2 + \iint_{-\infty}^{\infty} \underline{q}\cdot <d\underline{q}>(\tau)\,P(u,v)\,du\,dv\right) \\ &\quad + j\iint_{-\infty}^{\infty} \underline{q}\times <d\underline{q}>(\tau)\,P(u,v)\,du\,dv \end{aligned} \tag{15}$$

Equation (13) is related to the ordinary two dimensional time correlation tensor

$$R_{mn}(\tau) = <q_m q_n>(\tau) \tag{16}$$

Specifically,

$$<WW^*>(\tau) = R_{kk} + j\{\varepsilon_{mn3}R_{mn}\} \tag{17}$$

Comparison of equations (11), (15), and (17) shows that the amount of "swirl" present in the drift field is directly related to the amount of asymmetry in the R_{mn} matrix.

The complex correlation $\langle WW^* \rangle(\tau)$ is a scalar since it is invariant under coordinate rotation, and it has a magnitude and phase, which will be represented $S(\tau)$ and $\phi(\tau)$ respectively:

$$\langle WW^* \rangle(\tau) \underline{=} S(\tau)e^{j\Phi(\tau)} \qquad (18)$$

We make the following hypotheses about S and :

a. $S(\tau)$ is a measure of the correlation between coherent structures, and

b. $\Phi(\tau)$ is a measure of the local rotational distortion of the velocity field.

The physical basis for these statements is illustrated in figure 9. The figure shows the complex correlation (normalized by $\langle u^2 \rangle + \langle v^2 \rangle$, the mechanical energy) measured at the location x/D = .3 and r/D = .5. This is the position in the jet where the initially laminar shear layer has rolled up into regularly spaced, discrete lumps of vorticity which give rise to periodicity in the u and v autocorrelations. The data points shown in the figure are evaluated at multiples of the digitization period. The correlation is real and unity at zero time delay, and traces out a decaying spiral with increasing τ. Phase angle $\Phi(\tau)$ is a monotonically increasing function of time delay, which presumably reflects the large local shear, while magnitude

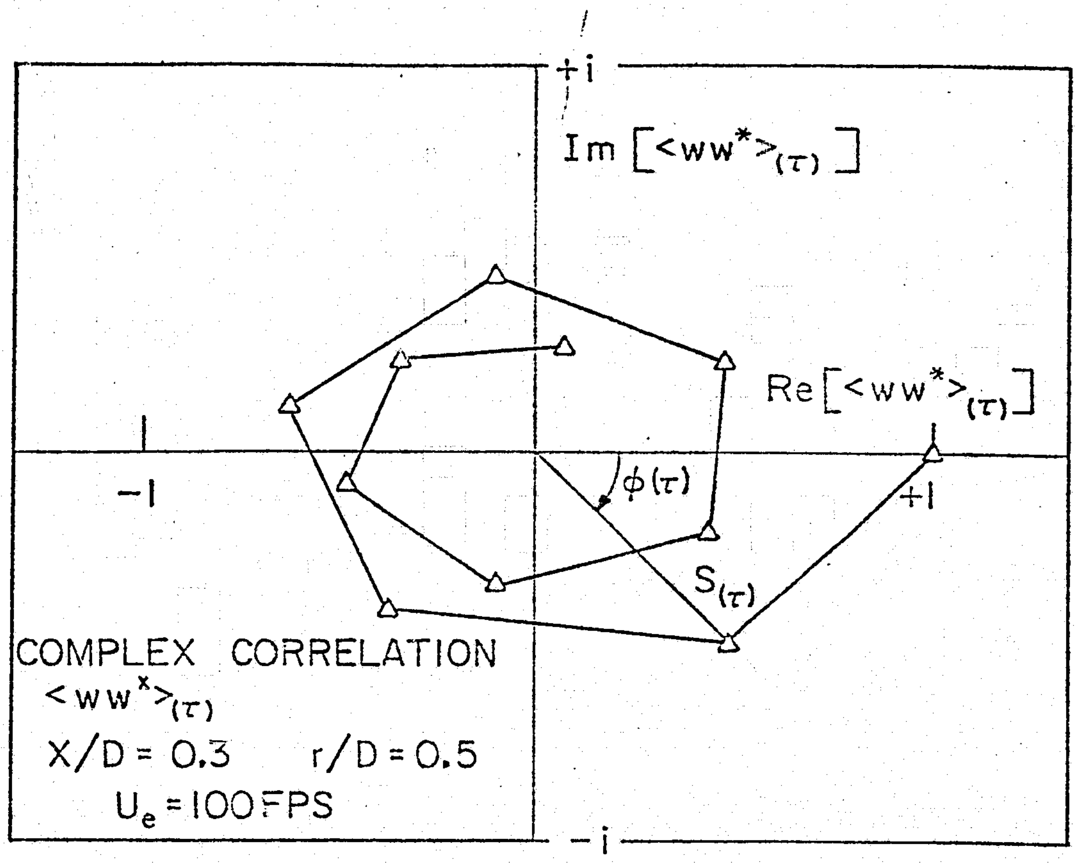

Figure 9. Complex correlation: x/D=0.3, r/D=0.5

$S(\tau)$ is a generally (although not monotonically) decreasing function of τ. It should be emphasized that there are two independent time scales present: the time scale of the periodicity, which is the time for the spiral to make one revolution, and the time scale associated with the decay of $S(\tau)$. This latter scale depends on how well the discrete lumps of vorticity are correlated with each other.

The limitations of the concept should be examined. There are two extremes where the complex correlation supplies little new information over ordinary u and v autocorrelations. First, if the flow is periodic and correlated over many periods, as in figure 9, then the autocorrelations appear as damped cosines, and their envelope contains essentially the same information present in the decay of $S(\tau)$. Second, if the flow is well-developed turbulent flow, the u autocorrelation is always positive and contains most of the information present in the $S(\tau)$ decay. Between these extremes, where the autocorrelations are periodic but highly damped, the complex correlation is a useful, and consistent method of measuring the correlation over the field as a whole, rather than over a single structure.

The measured forward differences are evaluated at one delay time, namely the sampling period dt. It would be useful to be able to use that vector field to estimate the forward differences for longer time delays in order to estimate the correlation at arbitrary τ. Whatever scheme is devised, there are two constraints that serve as confidence checks on the estimate. First the magnitude $S(\tau)$ of the correlation must generally decrease (usually monotonically), and second, the time averaged forward difference must be zero,

$$\iint_{-\infty}^{\infty} \langle d\underline{q} \rangle (u,v)\ P(u,v)\ du dv = 0 \qquad (19)$$

in order that the mean $(\langle u \rangle, \langle v \rangle)$ be time invariant.

4. PRELIMINARY JET SURVEY

4.1 Mean velocity profiles

In order to establish that the model jet is similar to those of other experimenters, radial profiles of mean velocity were measured with a hot wire probe and traverse at axial positions of 2, 4, 8, and 16 diameters downstream from the nozzle exit plane. The mean velocity profiles, along with profiles of rms turbulence are shown in figure 10.

The decay with axial distance of centerline mean velocity is plotted logarithmically in figure 11. Note that the asymptotic 1/x decay begins about eight diameters downstream. Data from Crow and Champagne (1971) exhibits good agreement.

Linear shear layer spreading, observed along the potential core region of the jet, is evident in figure 12. The local shear layer thickness h(x), derived from the mean profiles, is defined by the boundaries $<u>/U_o = .10$ and $<u>/U_o = .99$. Note that the initial shear layer thickness at the nozzle exit is .05 diameters.

The self-preservation of mean velocity profiles is examined in figure 13. The similarity parameter η is

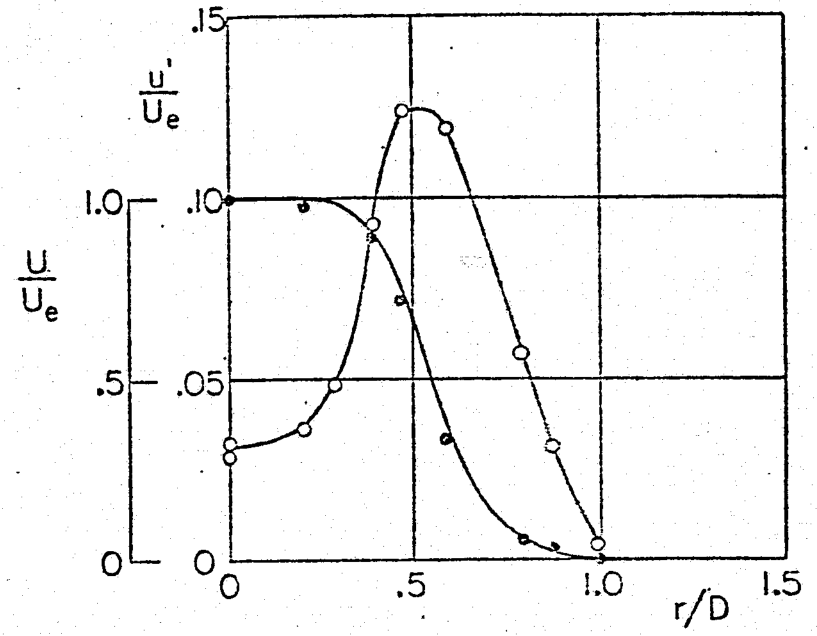

(a) x/D = 2.0

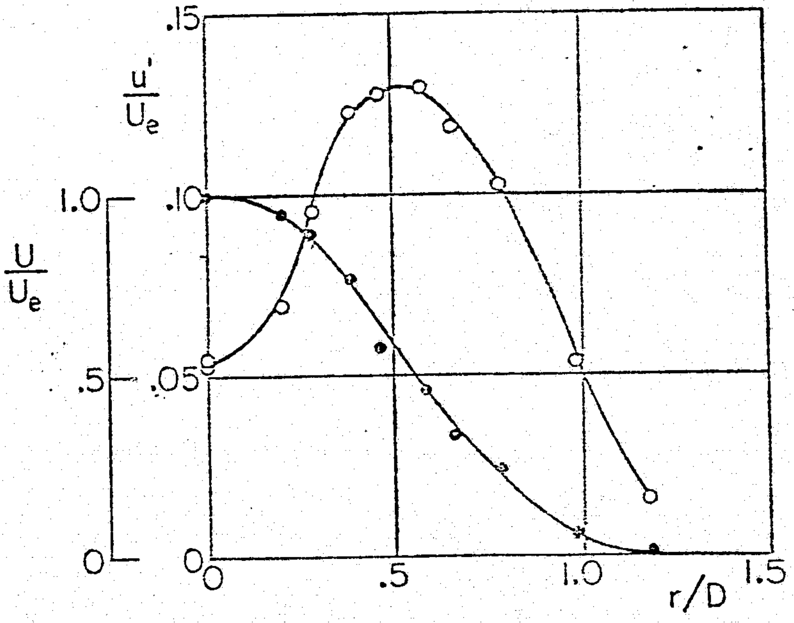

(b) x/D = 4.0

Figure 10. Profiles of mean velocity and turbulent velocity. Closed symbols refer to mean velocity and open symbols refer to turbulent velocity.

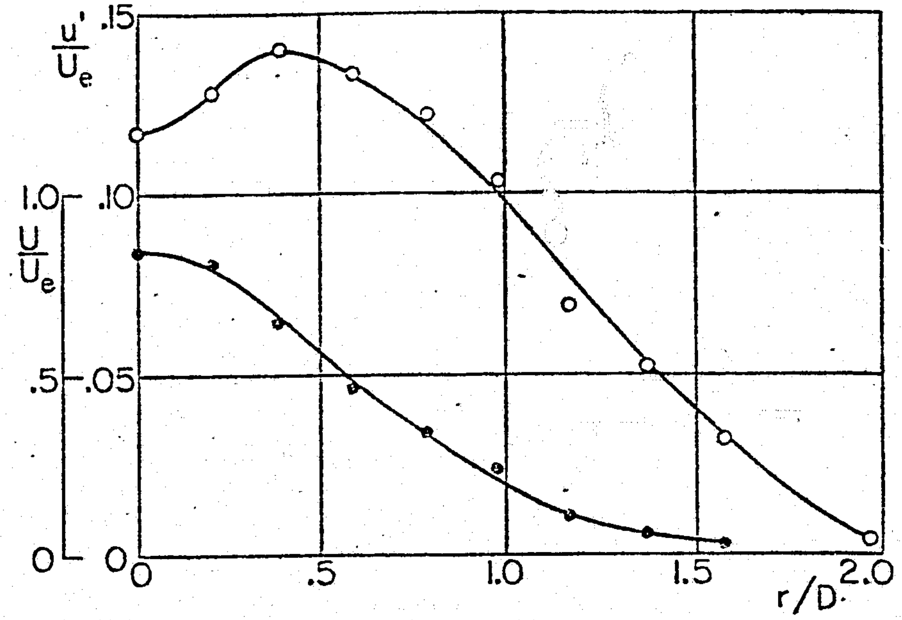

(c) x/D = 8.0

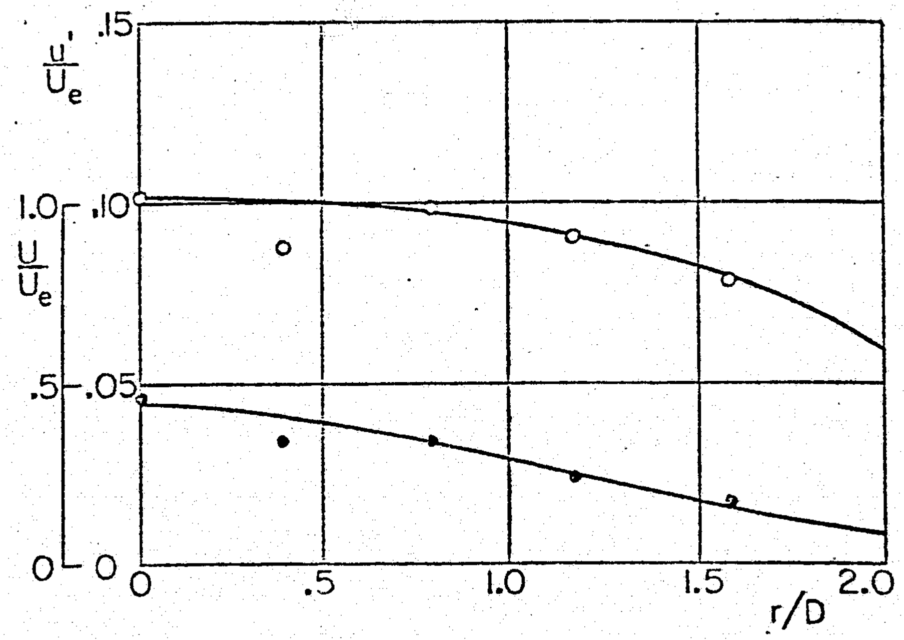

(d) x/D = 16.0

Figure 10. Continued.

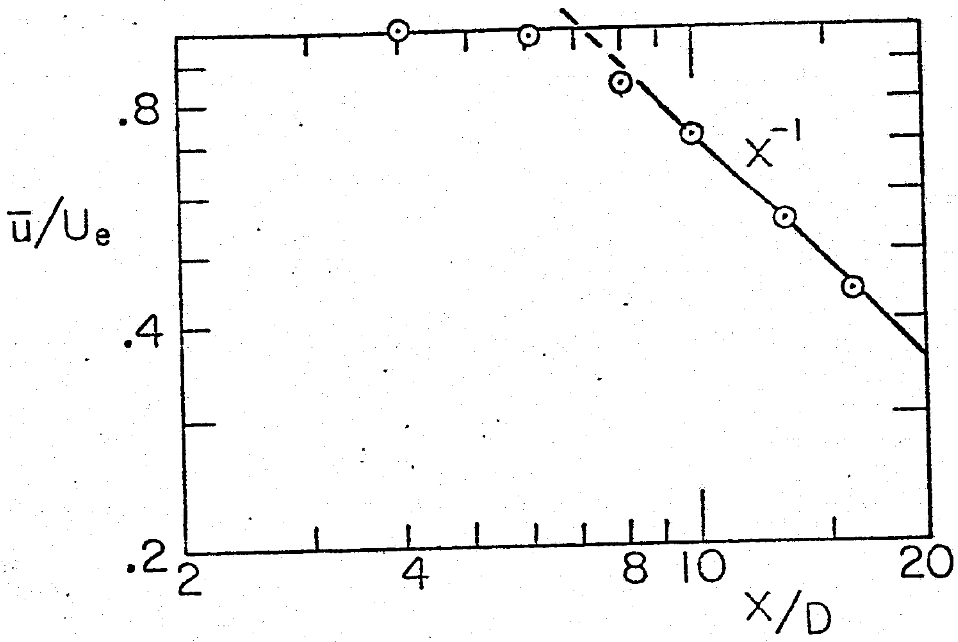

Figure 11. Axial decay of centerline velocity

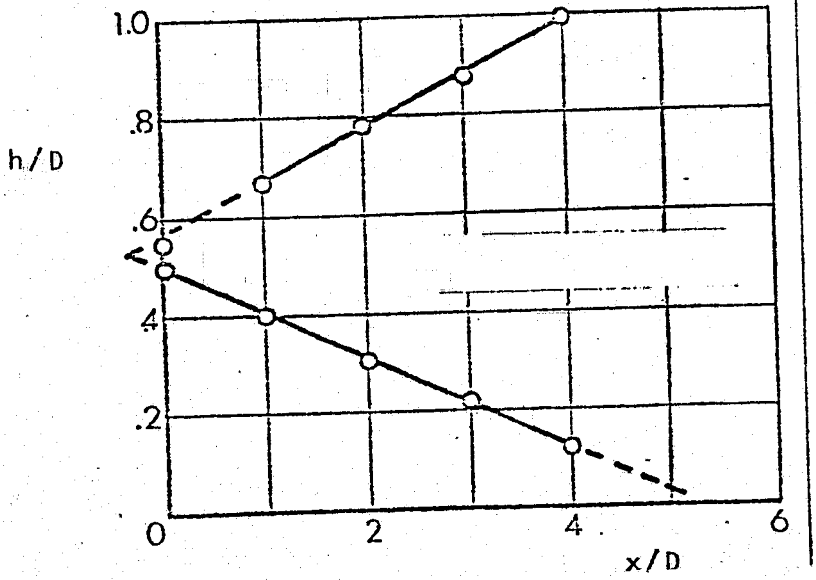

Figure 12. Shear layer spreading

defined:

$$\eta = \frac{r/D - .5}{x/D} \tag{20}$$

Reasonably good collapse is observed as far downstream as eight diameters.

4.2 Mean turbulence profiles

The profiles of rms fluctuating axial velocity, plotted on figure 10, were measured with the hot wire probe at the same time as the mean velocities. They are compared with turbulence profiles measured by other investigators, and will serve as a comparison for the joint velocity measurements presented in chapter 6.

The turbulence level measured at the nozzle exit plane is shown in figure 14 over a range of exit velocities. For most of our measurements, an exit velocity of U_e = 100 fps was selected; this corresponds to an exit plane turbulence level of .3%.

Self-preservation of turbulence profiles, figure 15, is evident at least as far downstream as eight diameters.

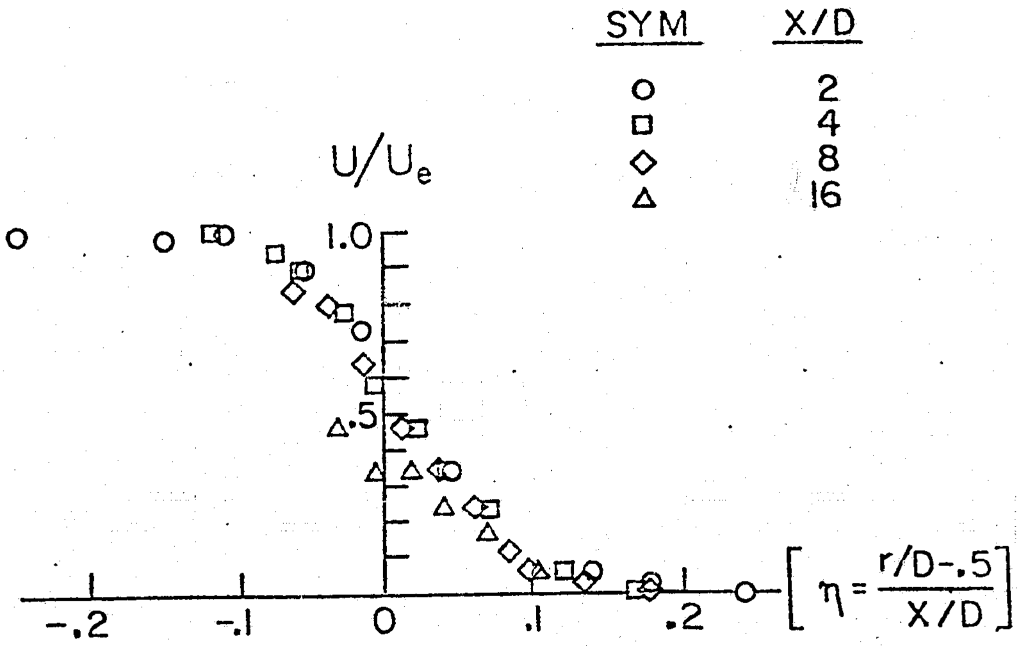

Figure 13. Self-preservation of velocity profiles

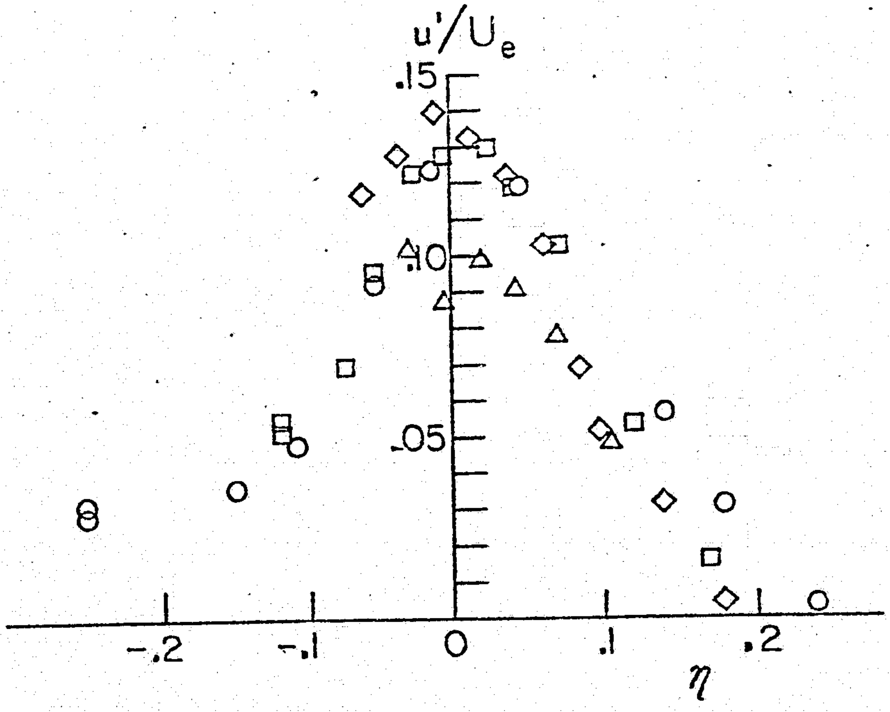

Figure 15. Self-preservation of turbulence profiles

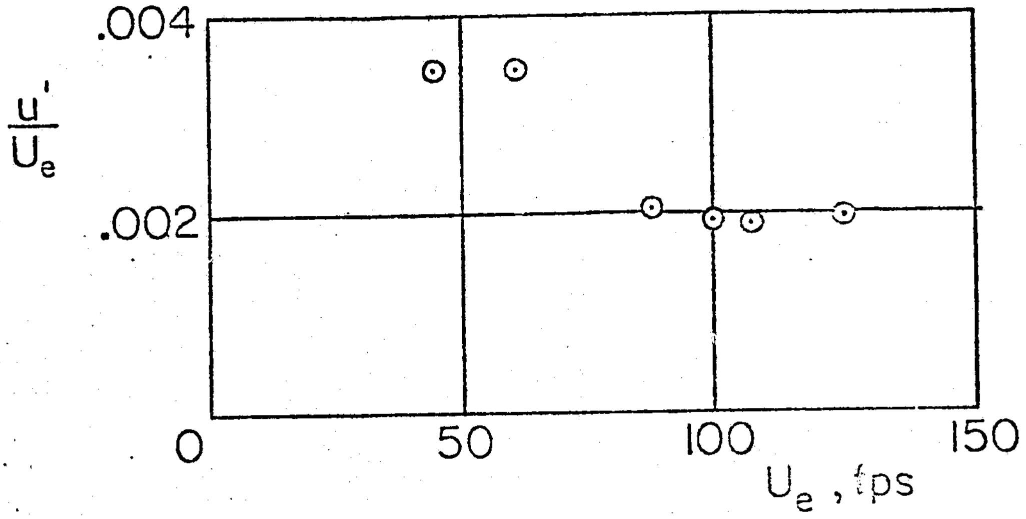

Figure 14. Exit plane turbulence

5. NEAR FIELD MEASUREMENTS

5.1 Near field static pressure

There is always some question as to what a microphone measures in the presence of mean flow. Work by Siddon (1969) and later by Fuchs (1972) indicate that there are probe configurations that allow microphones to respond mainly to static pressure fluctuations. For the measurements to follow the microphones were placed just outside the edge of the jet where mean velocities were small, and were oriented so that the plane of the diaphragm was roughly parallel to the mean flow.

Near field static pressure fluctuations can be expressed as a volume integral over momentum fluxes inside the mixing layer. The consequent spatial averaging makes static pressure particularly sensitive to large scale coherent structures, as indicated by Lau, Fisher, and Fuchs (1972).

5.2 Near field time scales

In order to characterize the mean shear layer structures from their near field pressure signatures, various statistical methods were used to derive characteristic time scales. It was possible to measure mean convection times from crosscorrelations between two microphones, while information about the time scales of the turbulent structures was derived from autocorrelations, and from wave counting. The microphones were located on the surface of an imaginary cone with a 10° half-angle and intersecting the inside diameter of the nozzle exit. Auto- and crosscorrelations of microphone signals were measured using the digital correlator, while a counter and oscilloscope were used for the wave counting.

The measured crosscorrelations are shown in figure 16 for various downstream positions. The two microphones were separated 5.0 mm axially; the time delay τ_c corresponding to the crosscorrelation peak is taken to be the average convection time between the microphones. The mean convection speeds, defined as separation distance divided by convection time, appear in figure 17 as a function of downstream position. The convection speeds are normalized by the jet exit speed, and the ratios are in good agreement with previous measurements along the potential core. Downstream of the core the convection speed decays asymptotically as $1/x$ with a magnitude of about half the local centerline speed.

The autocorrelations measured at various downstream

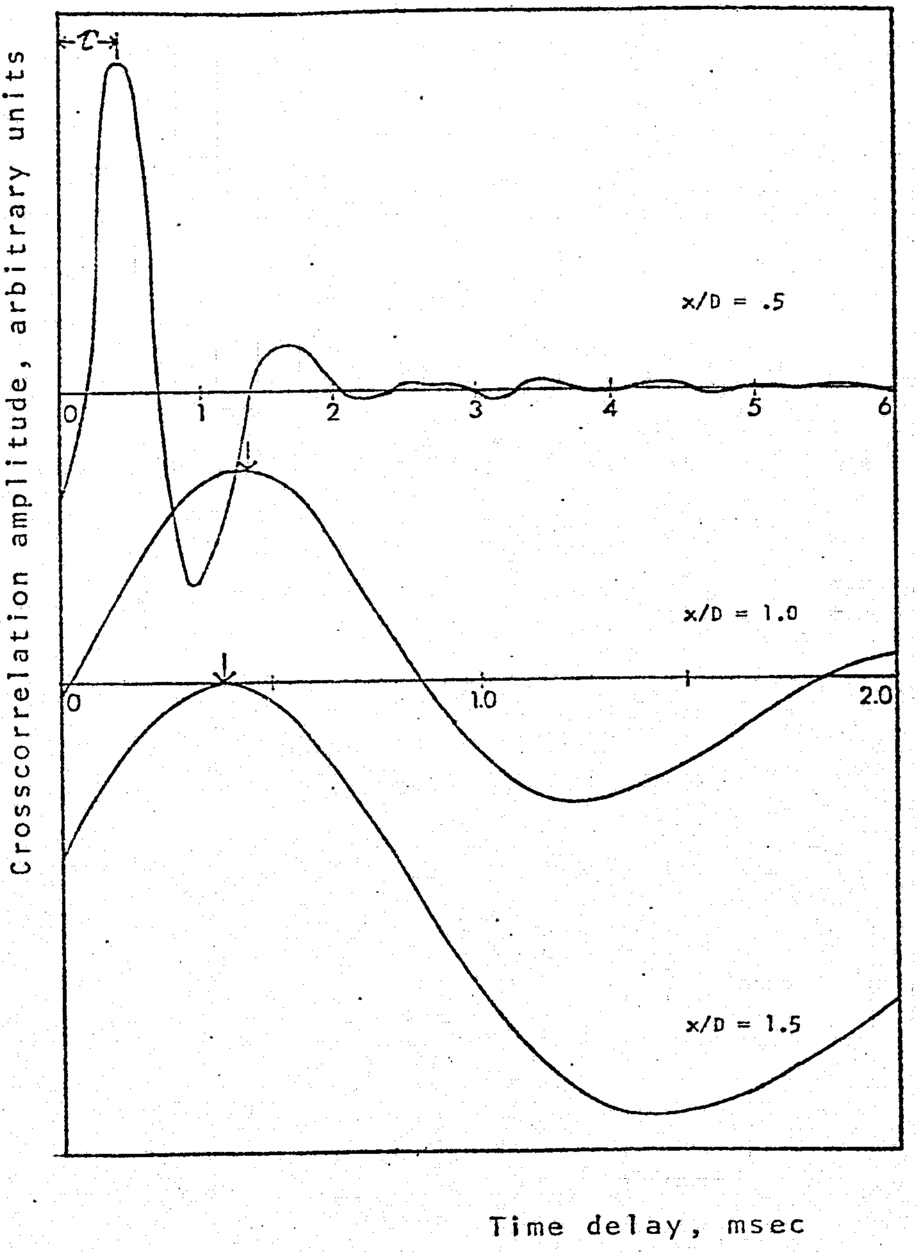

Figure 16. Near field crosscorrelations.

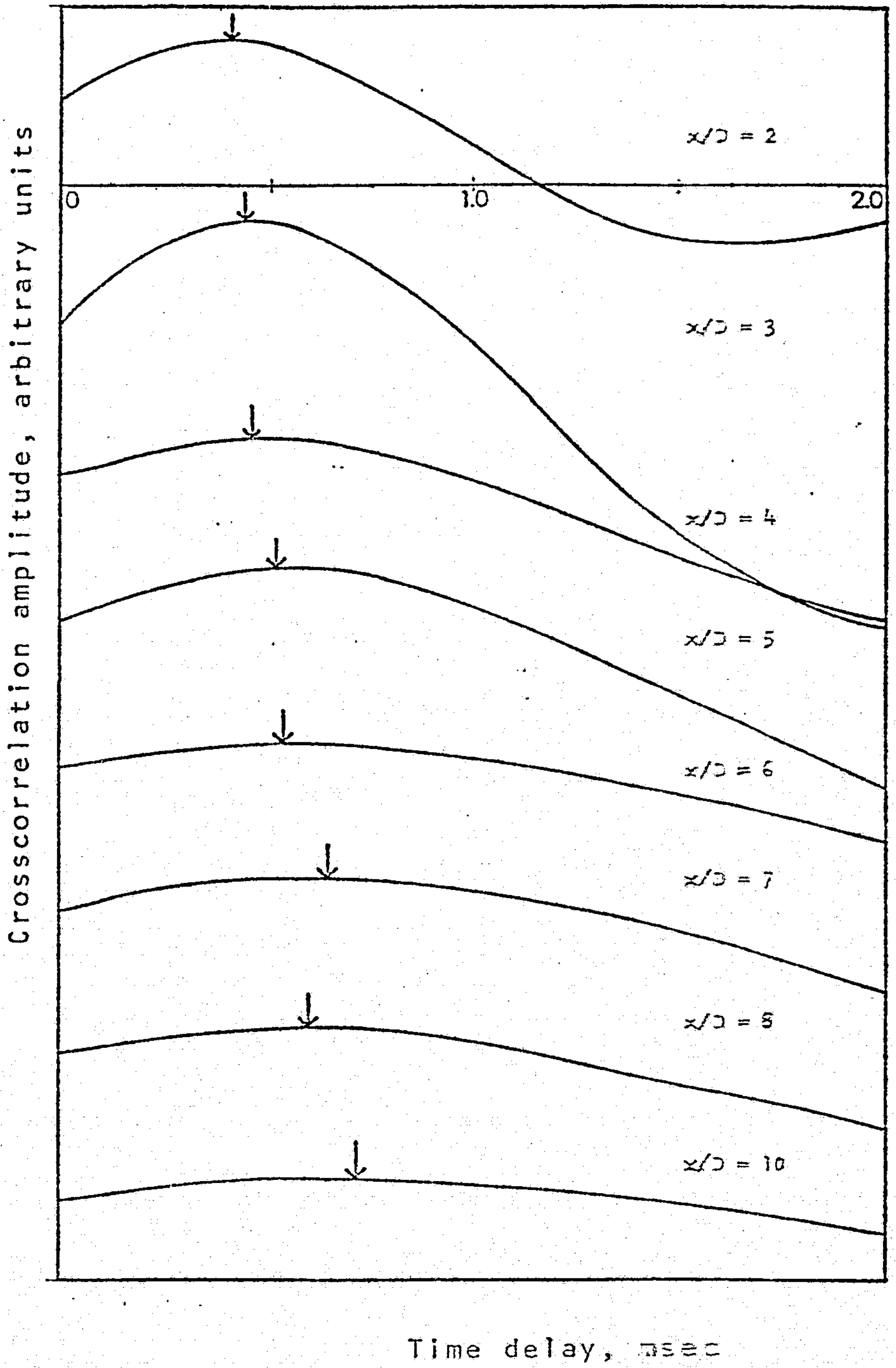

Figure 16. Concluded.

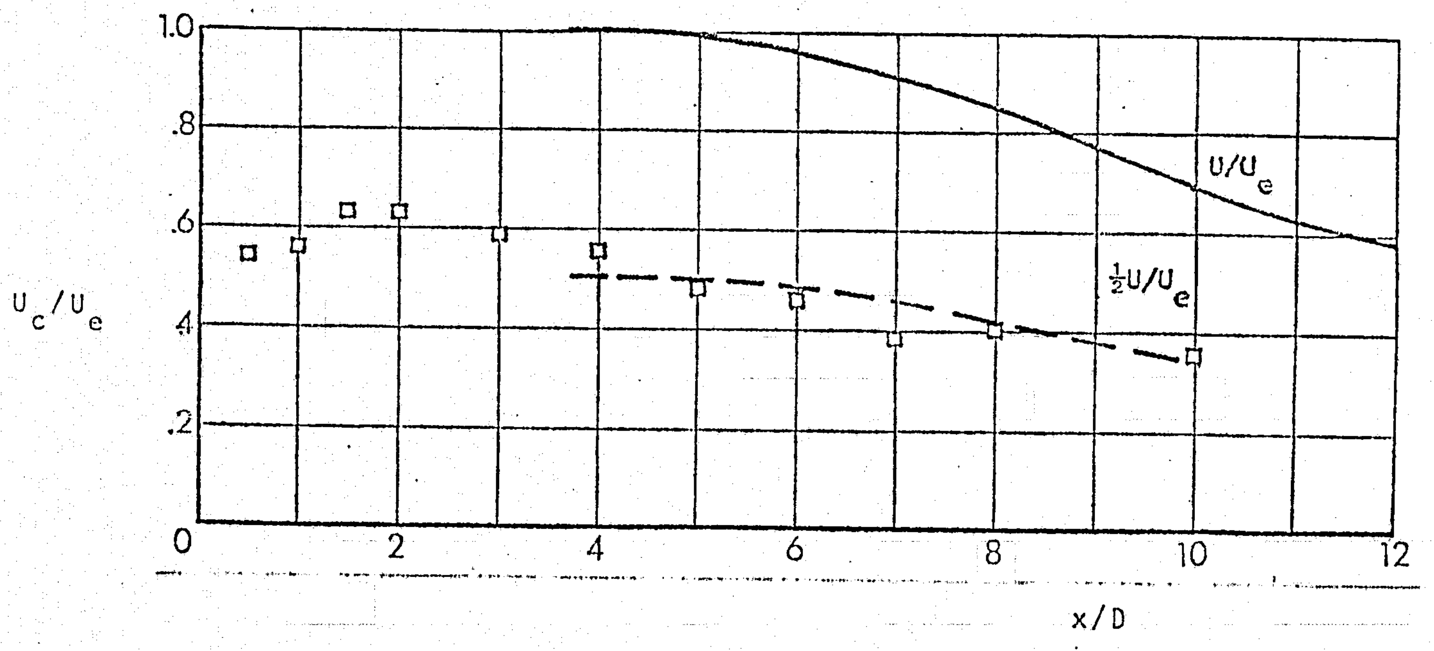

Figure 17. Turbulence convection speed vs x/D

positions are shown in figure 18, normalized by the rms signal. Interpretation of the associated time scales is more difficult than with the crosscorrelations. Along the potential core (x/D < 4) the autocorrelation appears like a damped cosine, and the associated time scale should be the period of the mean structure. For a couple of diameters downstream of the core there is no characteristic time scale at all, while even farther downstream (x/D > 7) there reappears a region of anticorrelation. Since there is no periodicity in these latter autocorrelations, the associated time scale is a measure of the coherence of the mixing layer turbulence at that point. The axial distribution of the time scales as they have been defined appears in figure 19, normalized by exit speed and jet diameter to form an inverse Strouhal number. In figure 20 the time scales are multiplied by the local convection speed to provide as estimate of the coherence length. The length scale appears to grow linearly with downstream distance in keeping with observed linear mixing layer spreading.

As an attempt to measure a time scale more closely associated with the spacing between successive coherent structures in the transitional mixing region of the jet, a wave counting technique was devised. A microphone was placed in the jet entrainment region, and Schmidt triggers were used to produce a narrow pulse each time the pressure

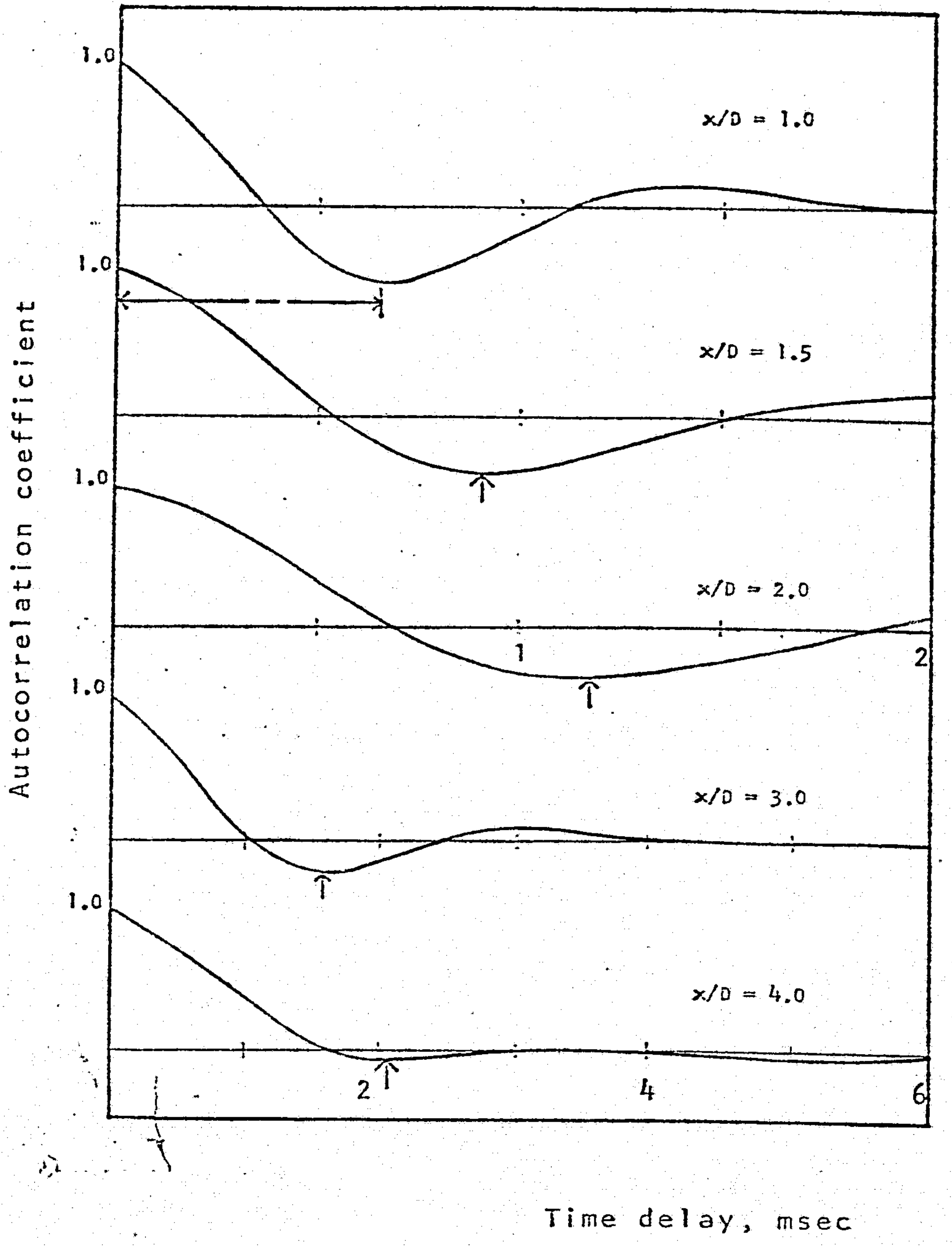

Figure 18. Near field autocorrelations.

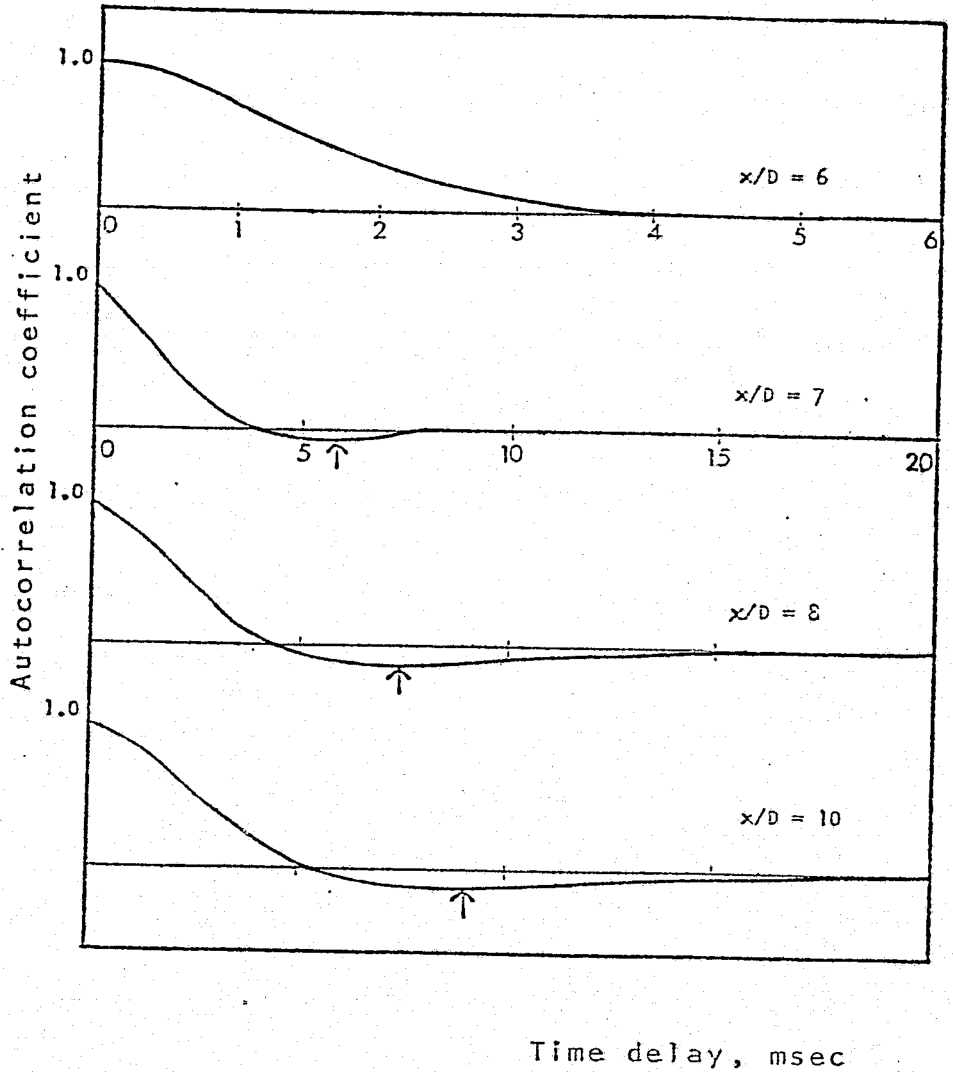

Figure 18. Concluded.

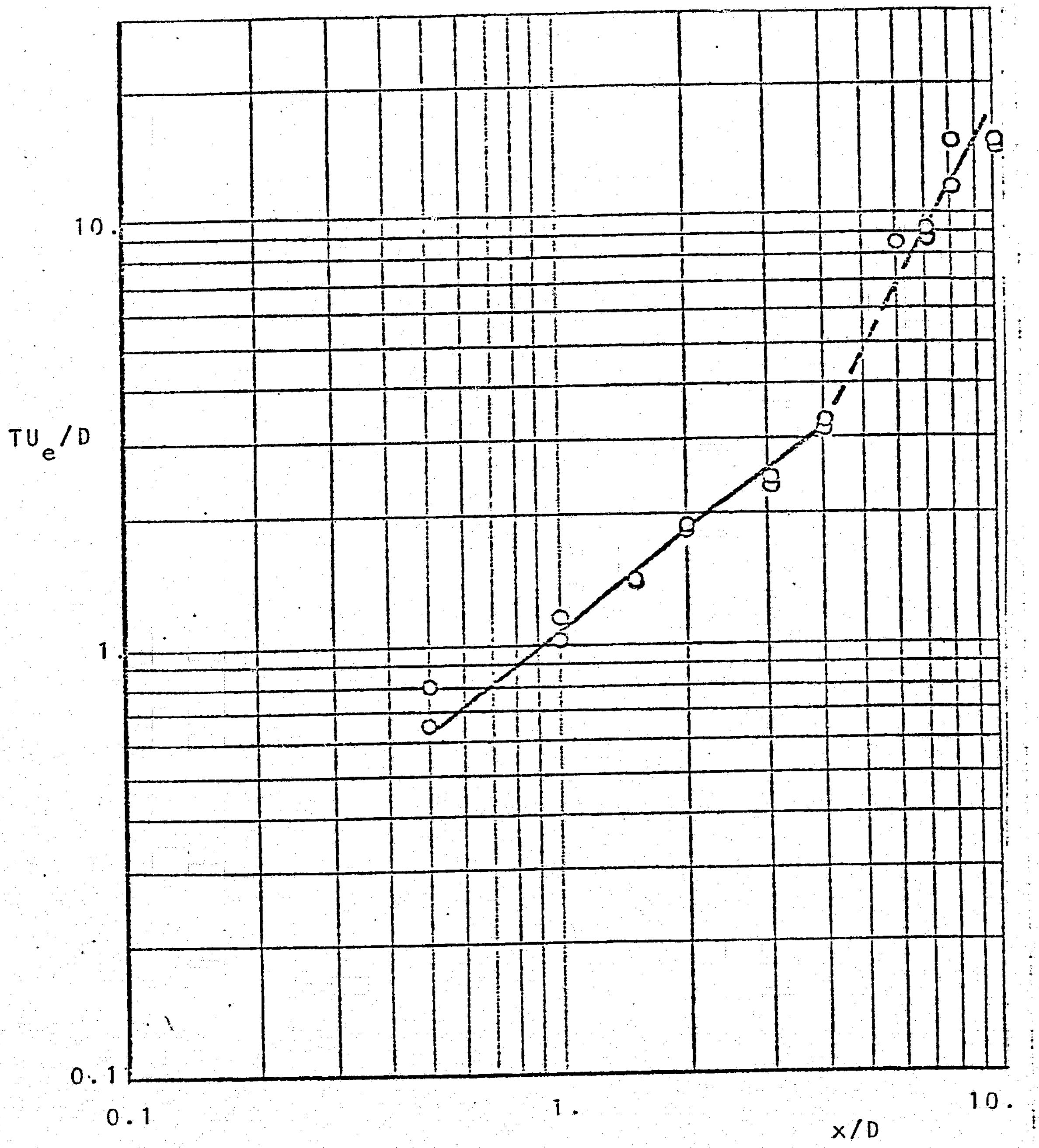

Figure 19. Autocorrelation time scales T(x)

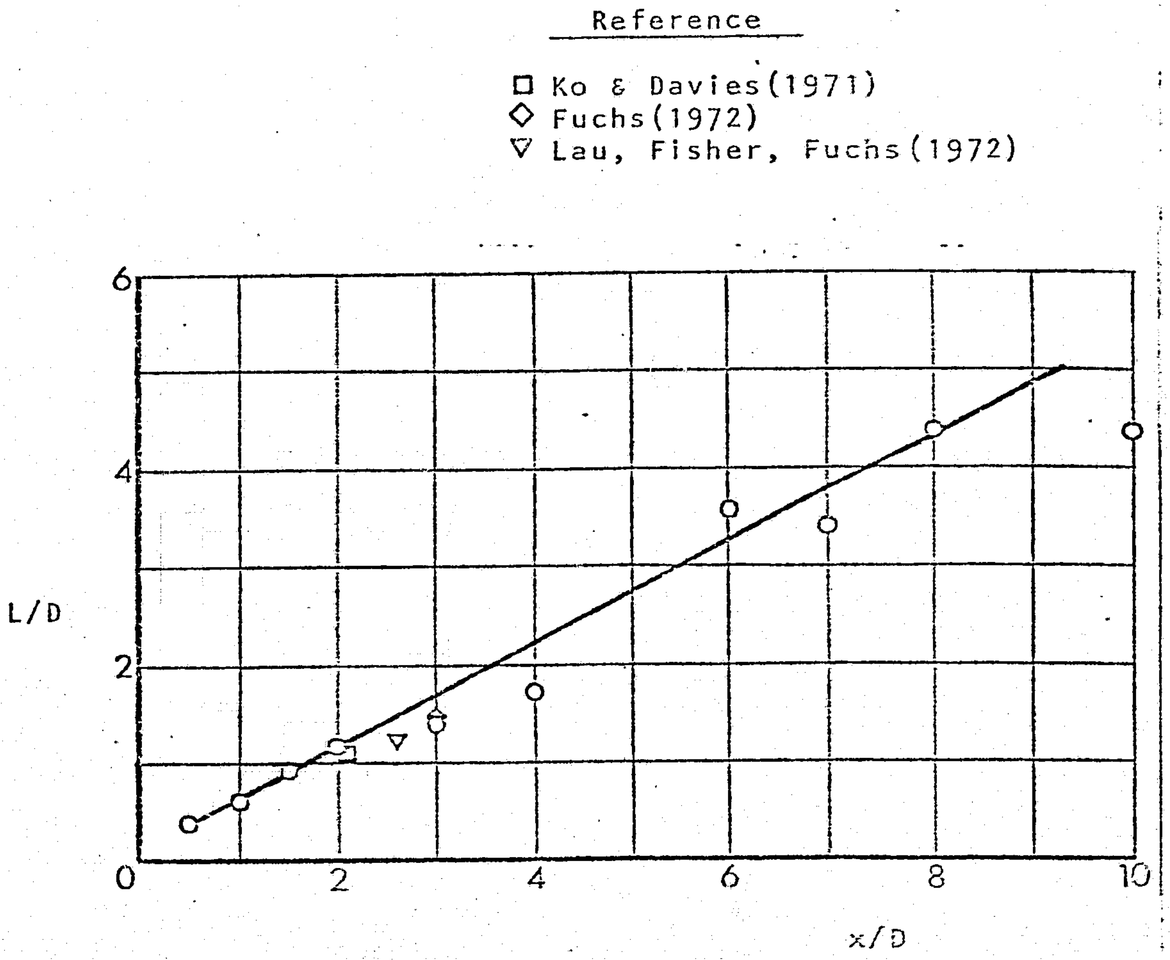

Figure 20. Convected length scale L(x).

signal passed through zero volts with a positive slope. The pulses were counted on a digital counter to derive an average passage frequency. In order to reduce the influence of the fine scale turbulence the microphone signal was low pass filtered an octave above the measured frequency and when the wave counting was repeated there was negligible change in the results. The measured passage frequencies, normalized as Strouhal numbers, are shown in figure 21. Figure 22 shows the local convection speed divided by the passage frequency to form the mean spacing λ. The spacing appears to increase linearly along the potential core but farther downstream ($x/D > 7$) the spacing asymptotically approaches a constant of about three diameters.

Comparison of figures 20 and 22 implies a contradiction: the size of the structures eventually becomes larger than the spacing between them. The statistical implication is that the pressure signal is increasingly skewed towards smaller time scales with increasing downstream distance. That is, the most probable time scale (reflected in the autocorrelations) is increasingly larger than the average time scale. It is possible that this reflects the pairing process in that interactions between adjacent concentrations of vorticity become increasingly intermittent downstream of the core. On the other hand the one-to-one correspondence between lumps of vorticity and

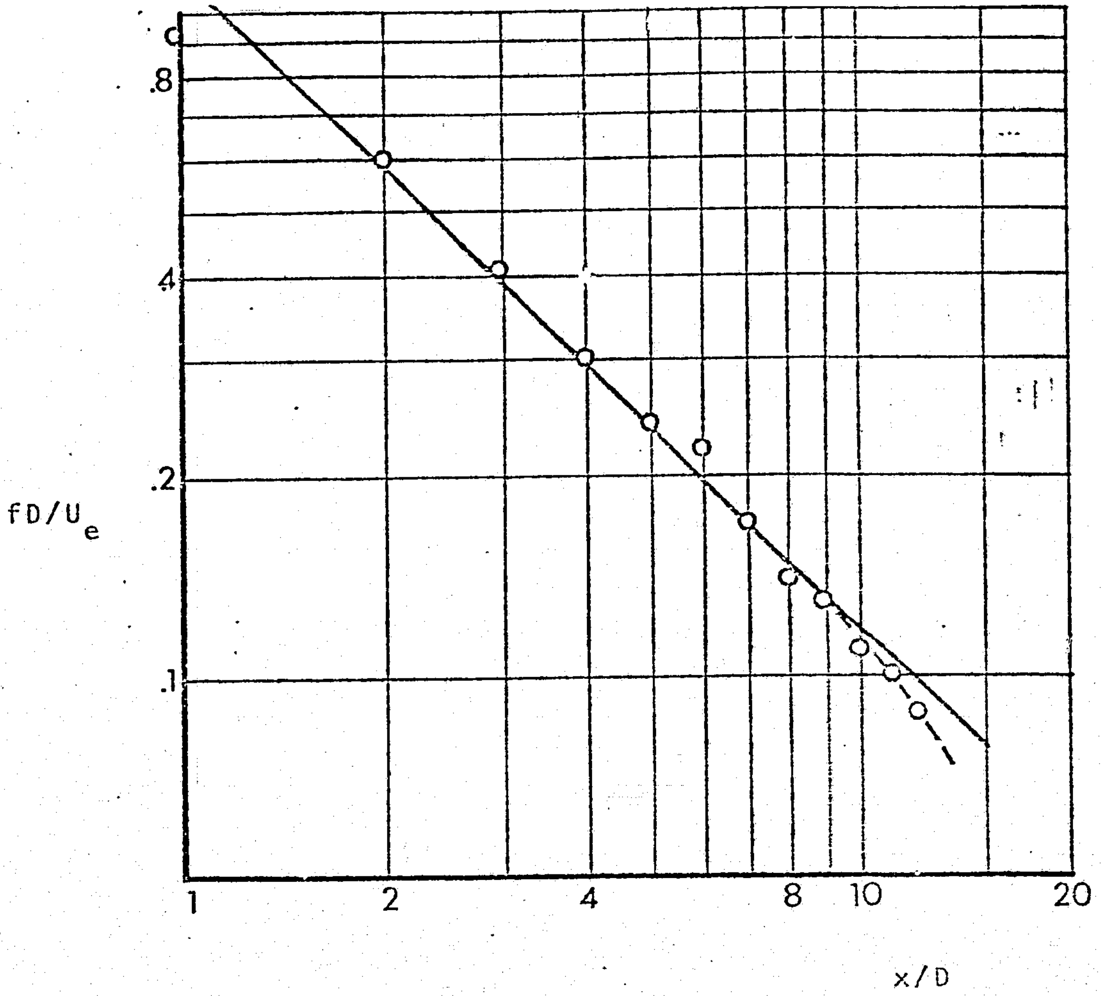

Figure 21. Passage frequency f(x).

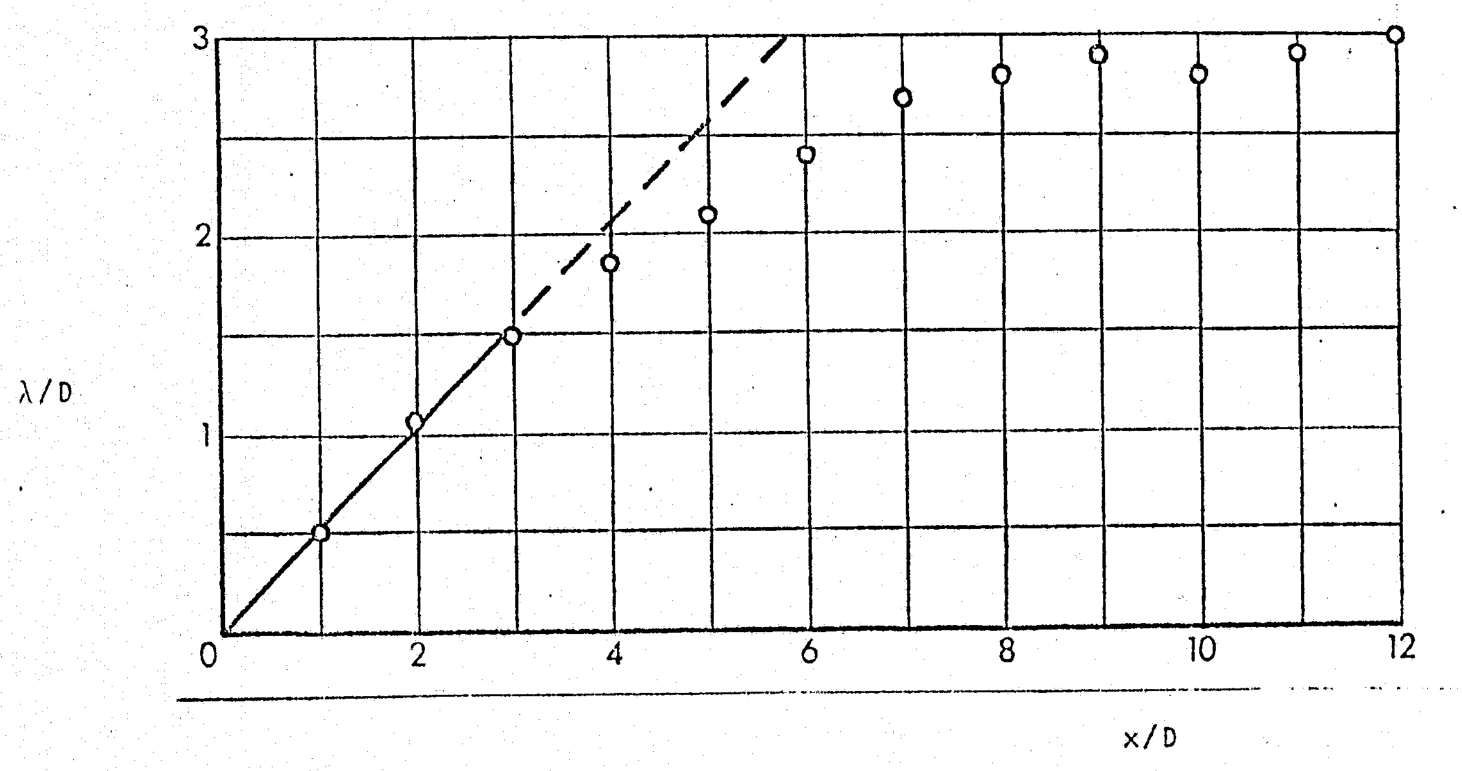

Figure 22. Vortex spacing λ(x)

near field pressure pulses may simply disappear with downstream distance. That interpretation would be consistent with the azimuthal correlation measurements shown in figure 23. The outputs of two microphones placed on either side of the jet at the same downstream distance were crosscorrelated, and the value of the maximum crosscorrelation coefficient is plotted against downstream distance. The correlation is negligible by the end of the core, in qualitative agreement with Mollo-Christensen's measurements (1967). Again this can be reconciled with the pairing model in that the vortex rings are observed to lose their axisymmetry through the production of azimuthal modes.

From the considerations above it is apparent that near field pressure measurements are open to a lot of misinterpretation. Consequently most of this investigation is directed towards mixing layer measurements.

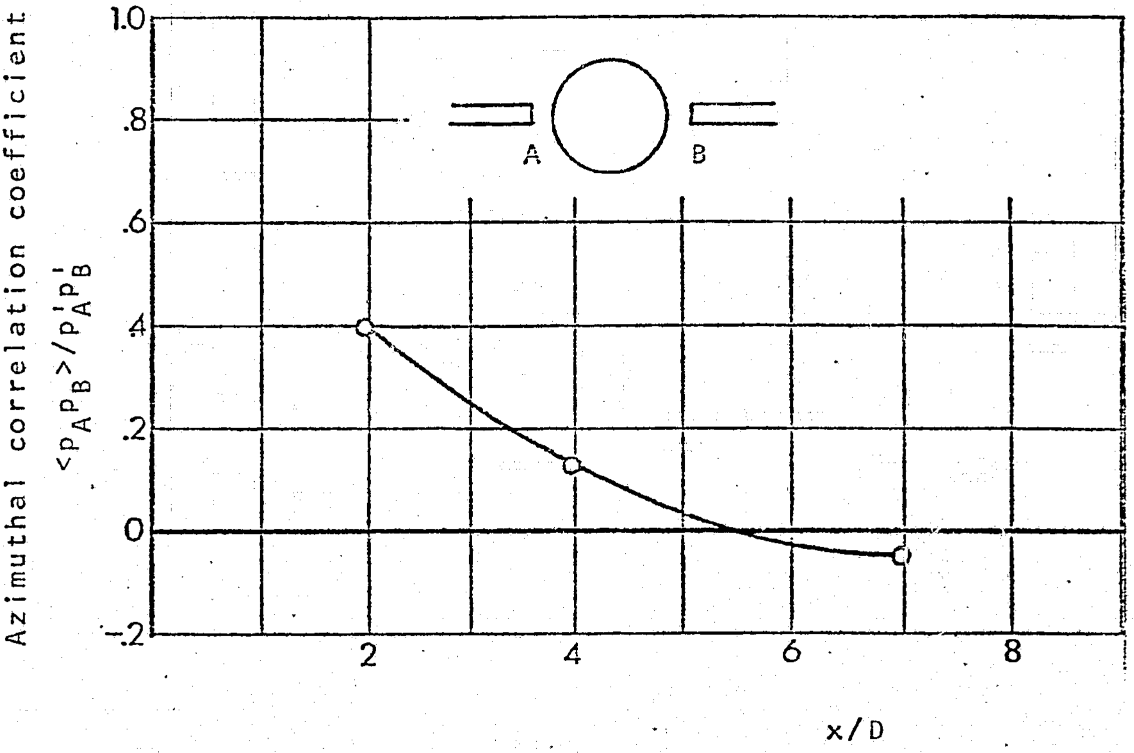

Figure 23. Azimuthal correlation vs. x/D

6. MIXING LAYER STATISTICS

6.1 Joint (u,v) statistics

For the purposes of this section the jet was considered to consist of three separate regions: the region close to the nozzle exit ($x/D < .5$) where the shear layer undergoes transition from laminar to turbulent spreading; the potential core region ($.5 < x/D < 5$) where the cylindrical, turbulent shear layer grows linearly until the jet is fully mixed; and the transitional mixing region ($5 < x/D < 20$), which has been observed to be the major source of acoustic radiation. Data was collected at representative locations in each region as summarized in table 1.

Data from each location was digitized and analyzed to produce joint probability densities, drift vectors, and diffusion tensors. The results will be presented in the following pages. Joint probability densities are displayed in terms of equally spaced contours of constant probability. For clarity the presentation of the drift vectors is modulated by the corresponding joint probability density. The vectors are normalized so that the maximum vector magnitude is one cell width. Diffusion tensors are shown diagonalized in the coordinate system of their principal axes. They are similarly modulated and normalized. In each case the origin of the coordinate system is the mean velocity $(\langle u\rangle, \langle v\rangle)$. Where possible zero velocity is indicated on the joint probability figures by a tick mark. Four straight lines radiating outwards from the mark depict the calibration limits. The inner pair of lines define the actual domain of the calibration, while the outer pair depict the angles of the hot wires.

Note that the time step is fixed at 40 microseconds for all the drift and diffusion measurements. This value of dt, which is just the digitization period, corresponds to a resolution bandwidth of 12.5 kHz. The power bandwidth of the turbulence is less than 5 kHz.

Region	x/D	r/D	η
Laminar/turbulent transition	.2	.5	0
	.3	.5	0
Potential core	2	.5	0
		.6	.05
	4	.4	−.025
		.6	.025
Transitional mixing	8	0	−.062
		.5	0
		1.0	.062
	12	.5	0

Table 1. Joint statistics:
schedule of measurement locations.

The following parameters were generated to describe the joint statistics at each point:

a) Rms axial velocity fluctuation u'/U_e

b) Ratio of axial to radial turbulence u'/v'

c) Mean shear stress $uv - u \;\; v \;\; /u'v'$

d) DRIFT $\iint \sqrt{<dq>_k <dq>_k}\; P(u,v)\; dudv$

e) DIFFUSION $\iint \sqrt{T_{kk}}\; P(u,v)\; dudv$

The variations of u'/U_e, u'/v', and $\{<uv> - <u><v>\}/u'v'$ with axial position is summarized in figure 24 along the ray $\eta = 0$, while figure 25 shows the variations across the shear layer. The measurements of other investigators are included for comparison. Although there is considerable variation between investigators, our measurements seem to fall within

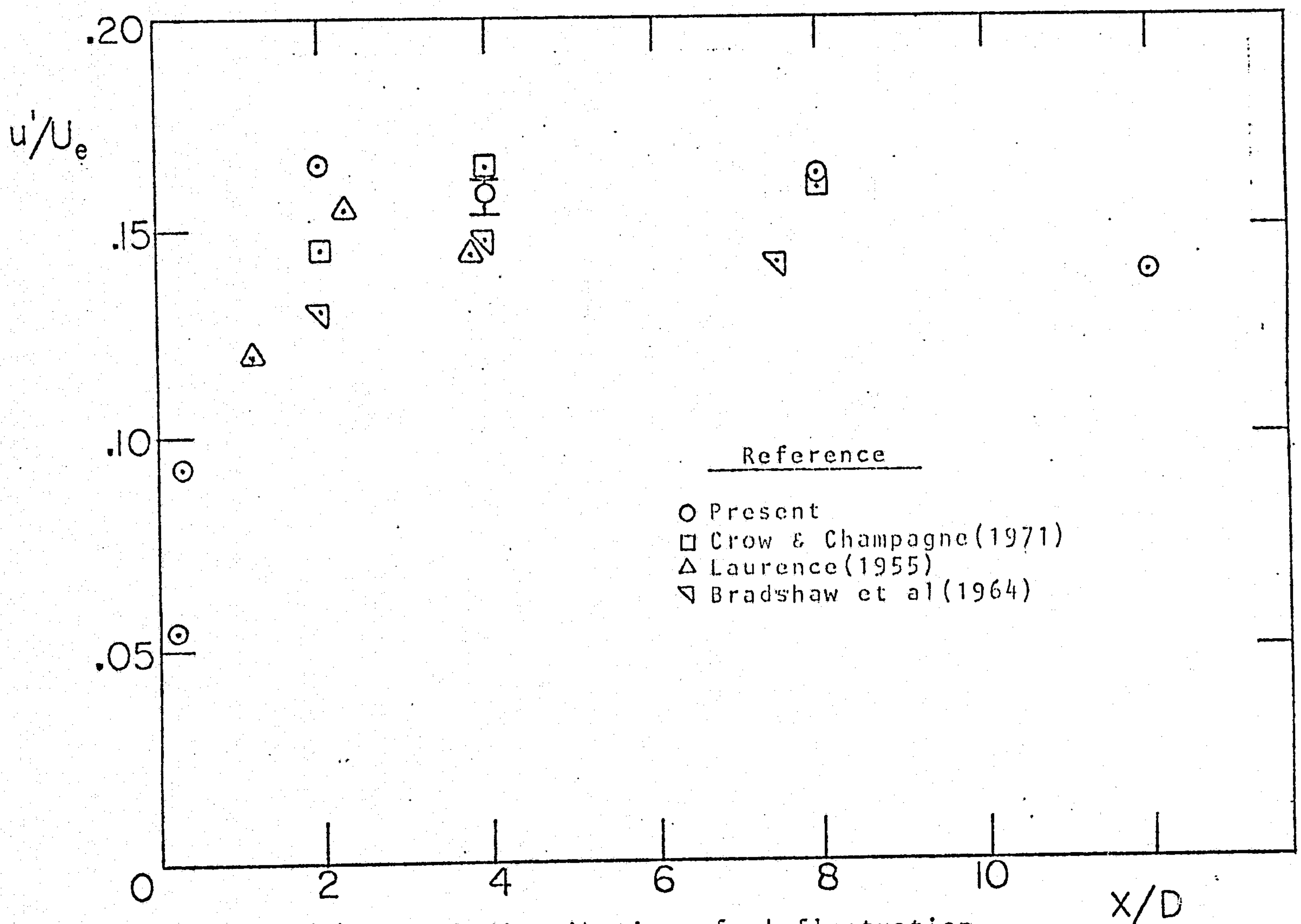

(a) Axial distribution of u' fluctuation

Figure 24. Axial distribution of mixing layer statistics. ($\eta = 0$)

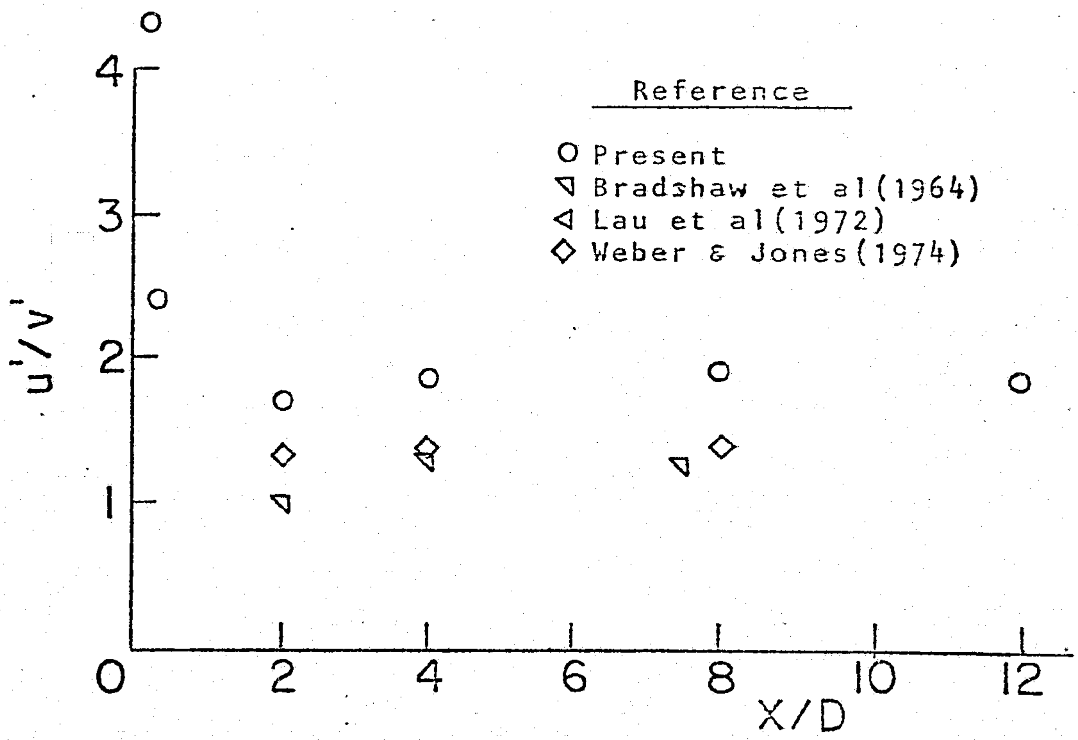

(b) Axial distribution of u'/v' ratio.

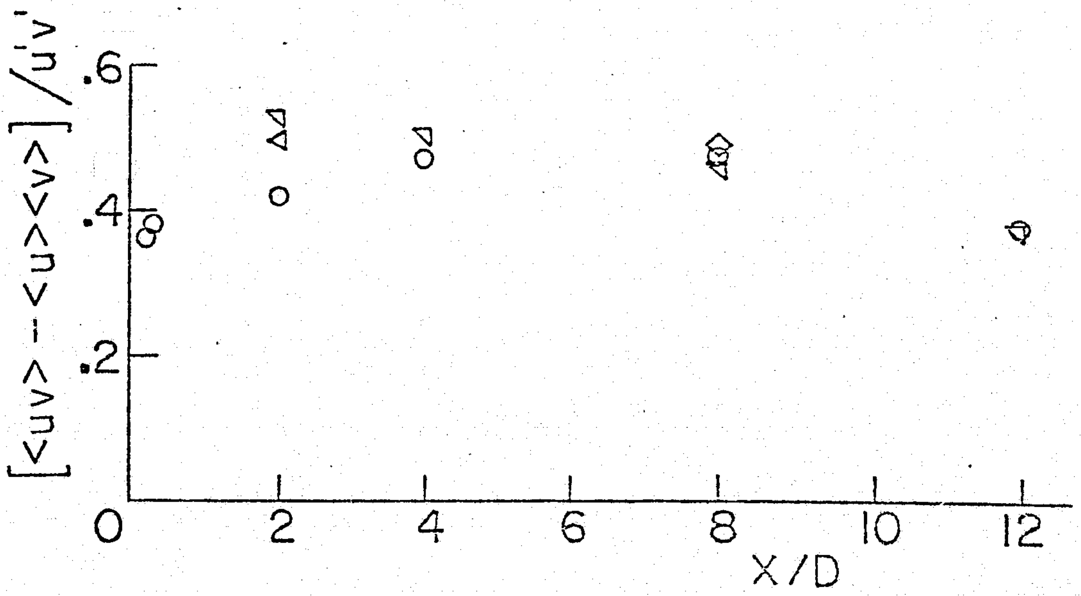

(c) Axial distribution of Reynolds stress.

Figure 24. Concluded.

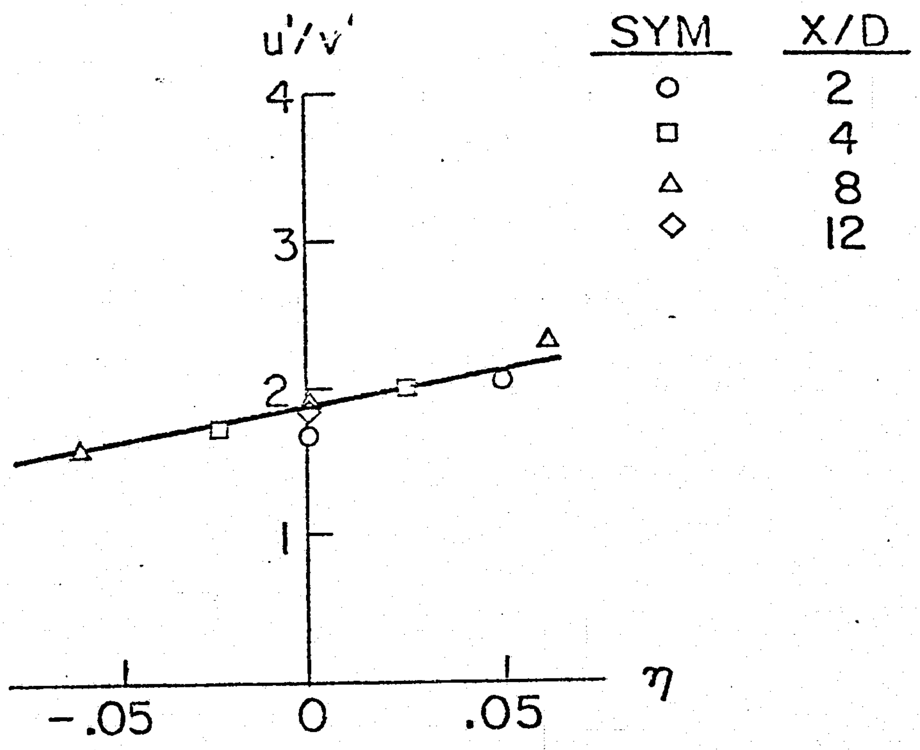

(a) Profile of u'/v' ratio

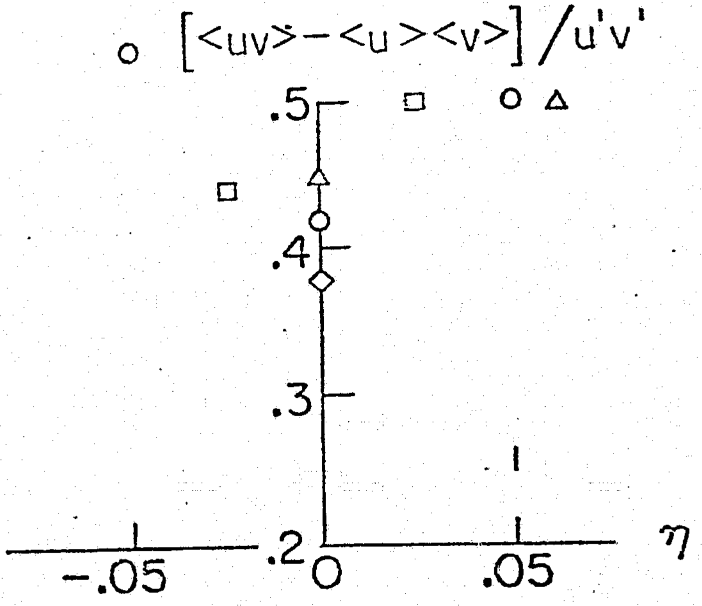

(b) Profile of Reynolds stress

Figure 25. Radial profiles of mixing layer statistics

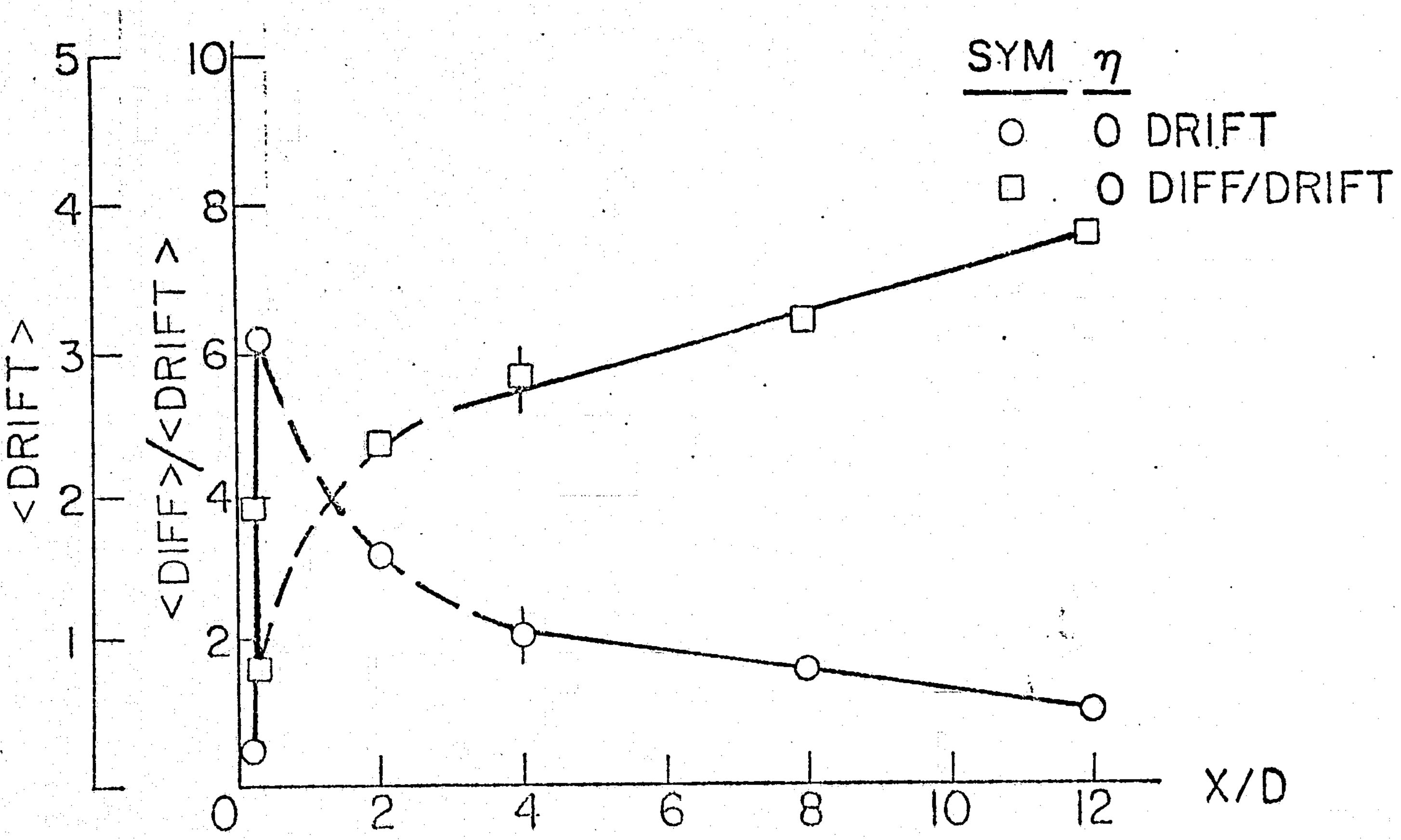

Figure 26. Axial distribution of DRIFT and DIFFUSION

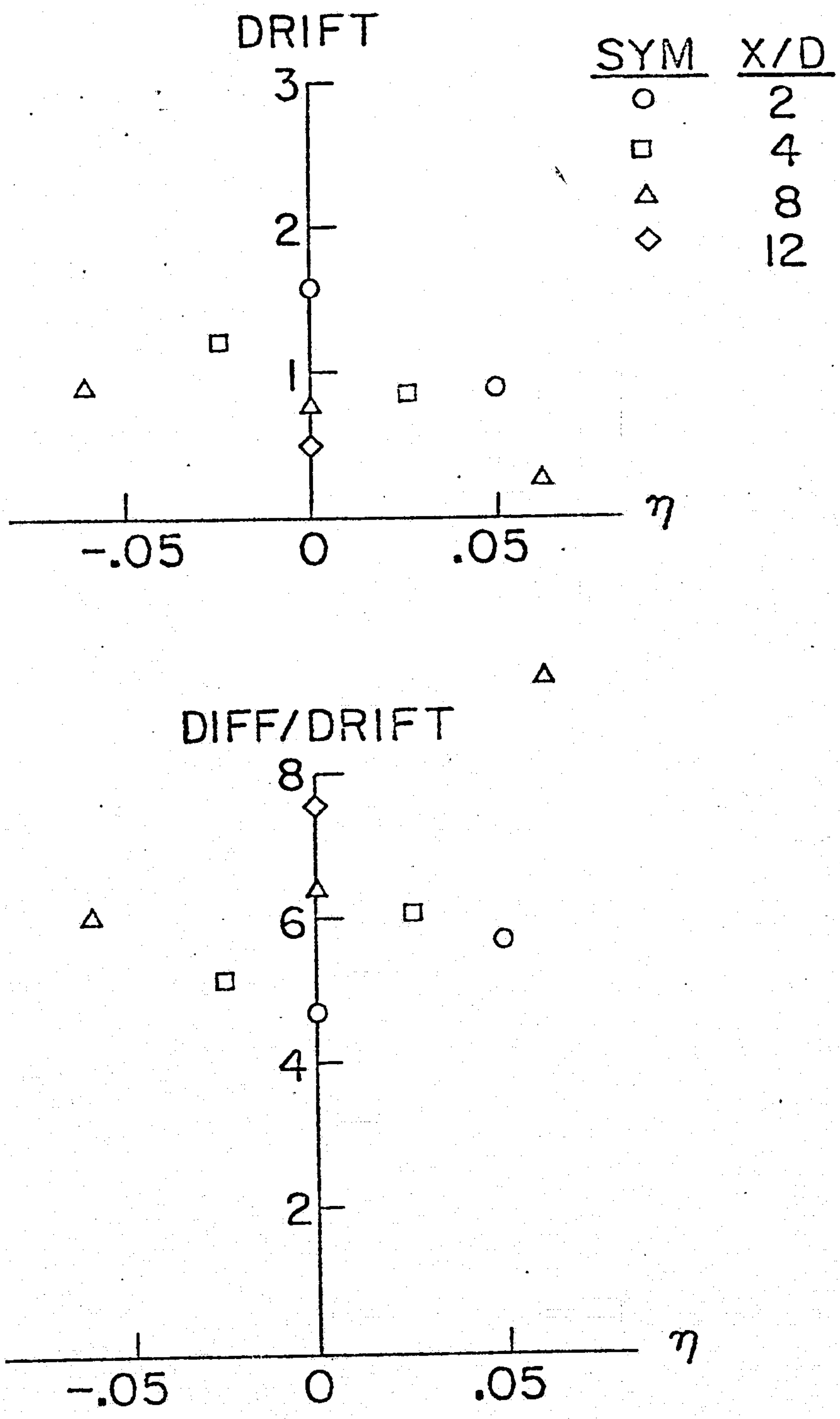

Figure 27. Radial profiles of DRIFT and DIFFUSION

the scatter. The axial variations of DRIFT and DIFFUSION/DRIFT are shown in figure 26, while the corresponding variations across the layer appear in figure 27.

Recall that the ratio of DIFFUSION to DRIFT is a measure of how "noisy" the signal is; the smaller the ratio the more deterministic the flow. The implication is that statistically the turbulence is increasingly noise driven at increasingly large downstream positions, and at increasingly large radial positions.

6.2 Laminar/turbulent transition region

The flow leaving the nozzle exit is initially laminar. The shear layer that develops at the edge of the jet is spatially unstable and the resultant waves grow with a Strouhal number of .2 (based on shear layer thickness at the nozzle exit) which is in agreement with the "eigenfrequency" of the most amplified spatial instability (e.g. Lessen, 1949). At some downstream position the waves coalesce and roll up into cylindrical rings of concentrated vorticity which interact with each other. From corroborative data the first pairing is known to occur at an x/D between .2 and .3. The corresponding joint probability densities, P(u,v), are shown in figure 28. From figures 24 and 28, it is apparent

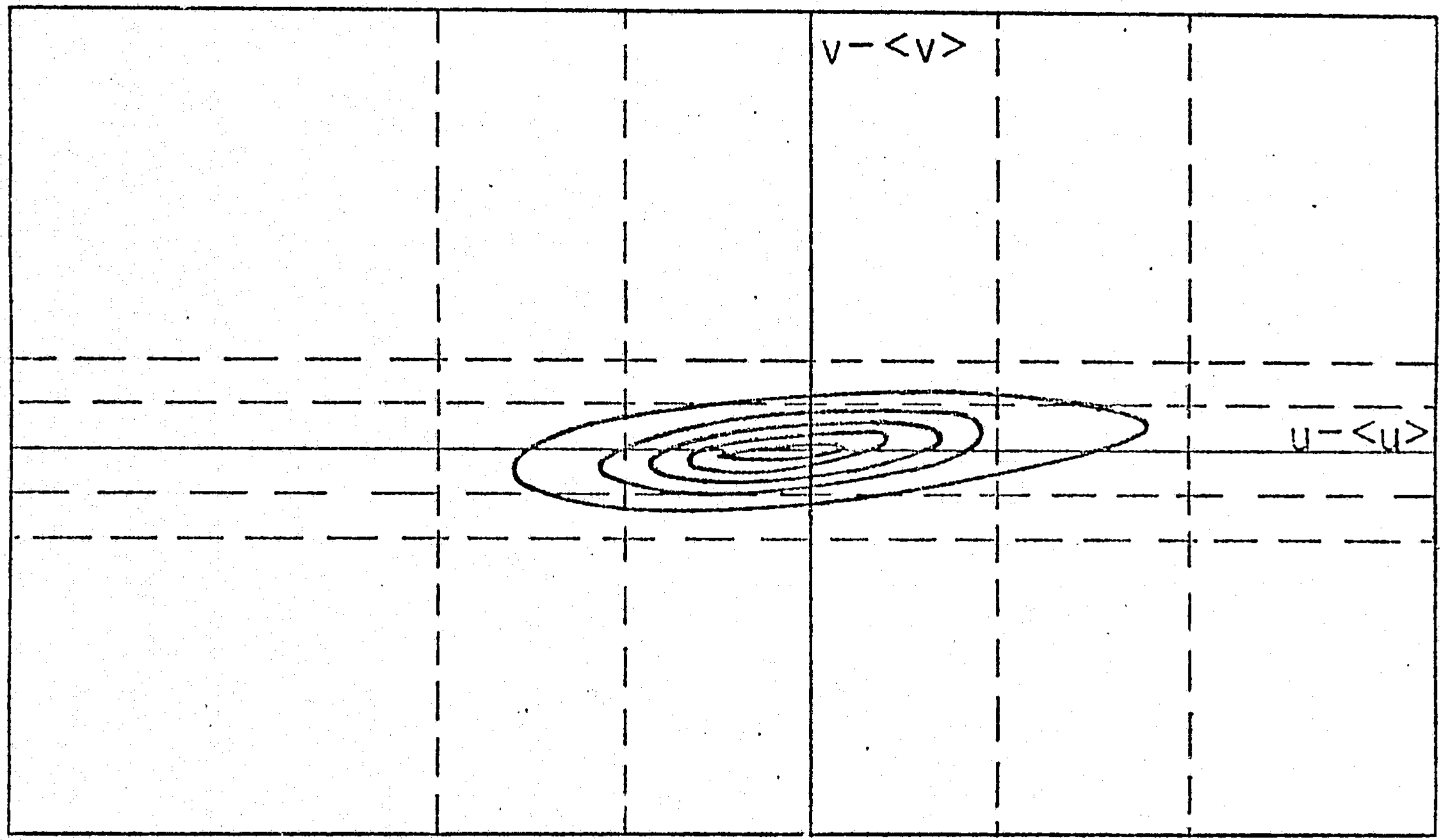

(a) x/D = 0.2, r/D = 0.5

Figure 28. Joint probability densities: x/D = .2,.3

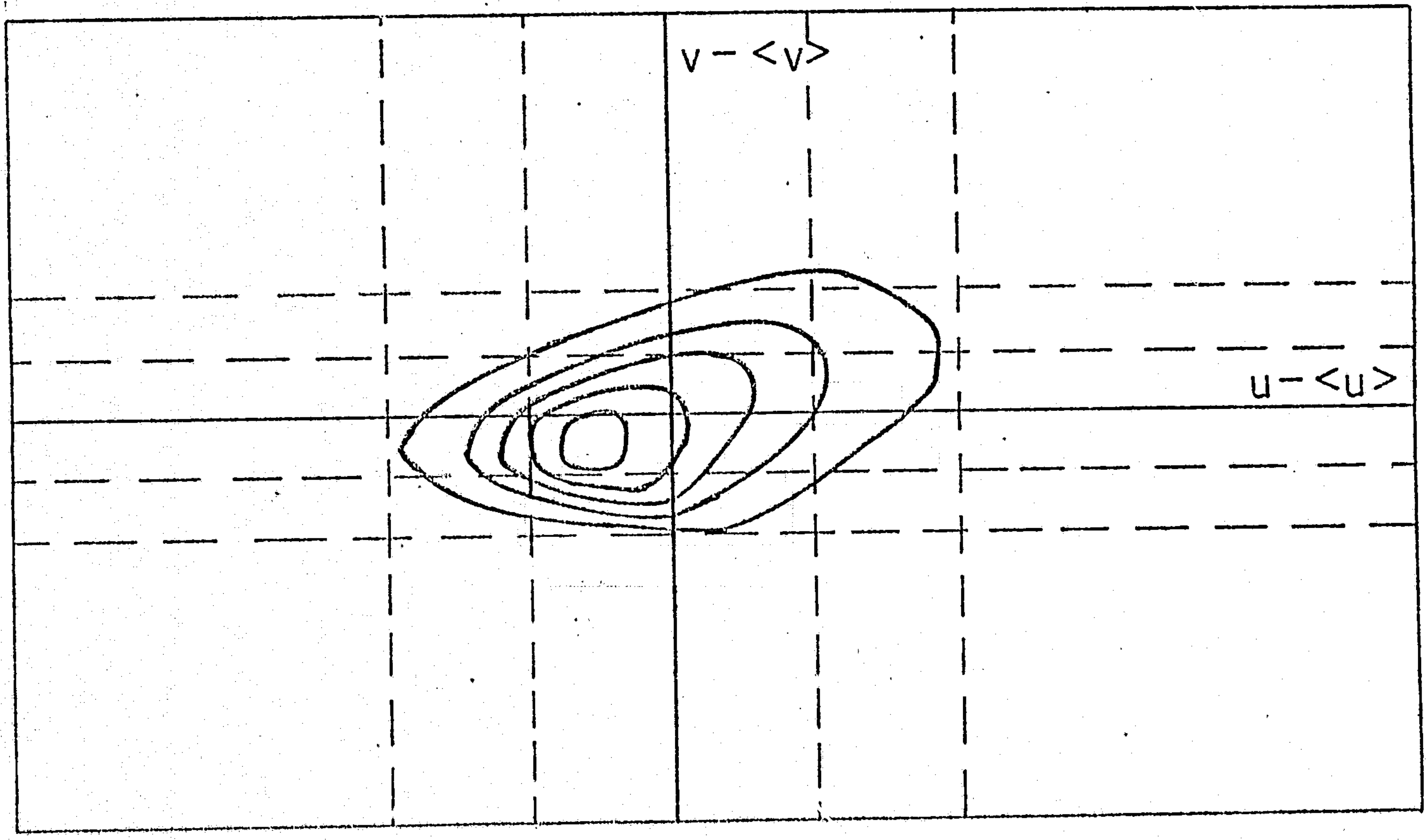

(b) x/D = 0.3, r/D = 0.5

Figure 28. Concluded.

that the aspect ratio u'/v' of the joint probability distribution decreases dramatically after transition. This can be understood after examining a short sample of the u,v velocity record figure 29. At x/D = .2, the signal is dominated by low frequency "whipping" of the whole jet so that the statistics reflect the rather large mean shear at that point. At x/D = .3, the signal is dominated by the strong vortex structures associated with roll up and pairing. Consequently, the flow process appears more deterministic.

Measured drift vectors $<d\underline{q}>(u,v)$ are shown in figure 30, while figure 31 shows the measured diffusion tensors. The lengths of the double vectors are the eigenvalues of the tensors while their orientation represents the axes of the corresponding eigenvectors.

The small DIFFUSION/DRIFT ratios and large anisotropy evident among the diffusion tensors reflect the determinateness of the flow at these small downstream positions. There is considerable "swirl" associated with the drift vectors in the sense that they seem to align with the probability contours to form closed trajectories in the hodograph plane. This behavior seems to be associated with the periodic nature of the flow field at this point, as discussed in section 3.4.

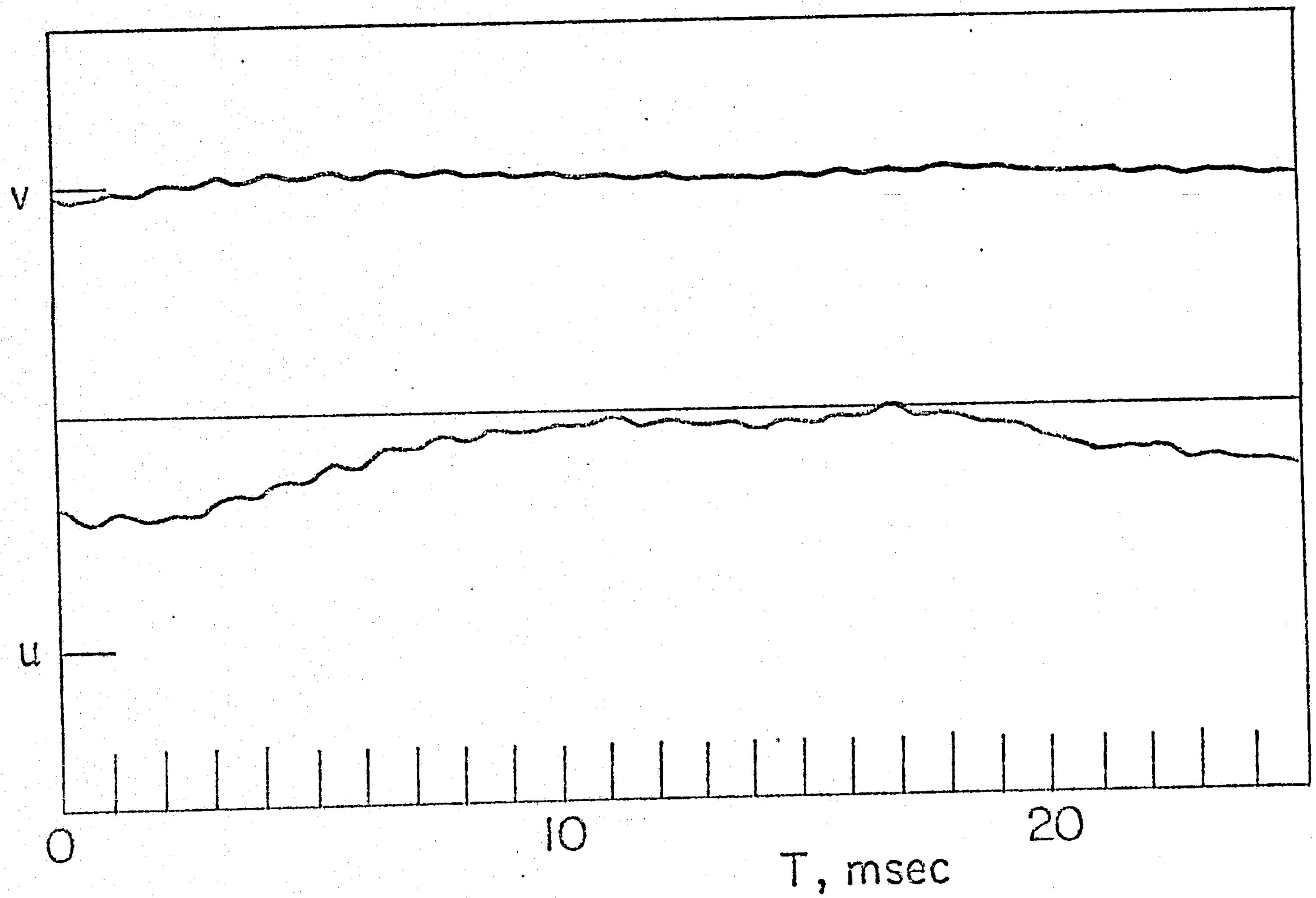

(a) x/D = 0.2, r/D = 0.5

Figure 29. Sample u,v velocity records: x/D = .2,.3

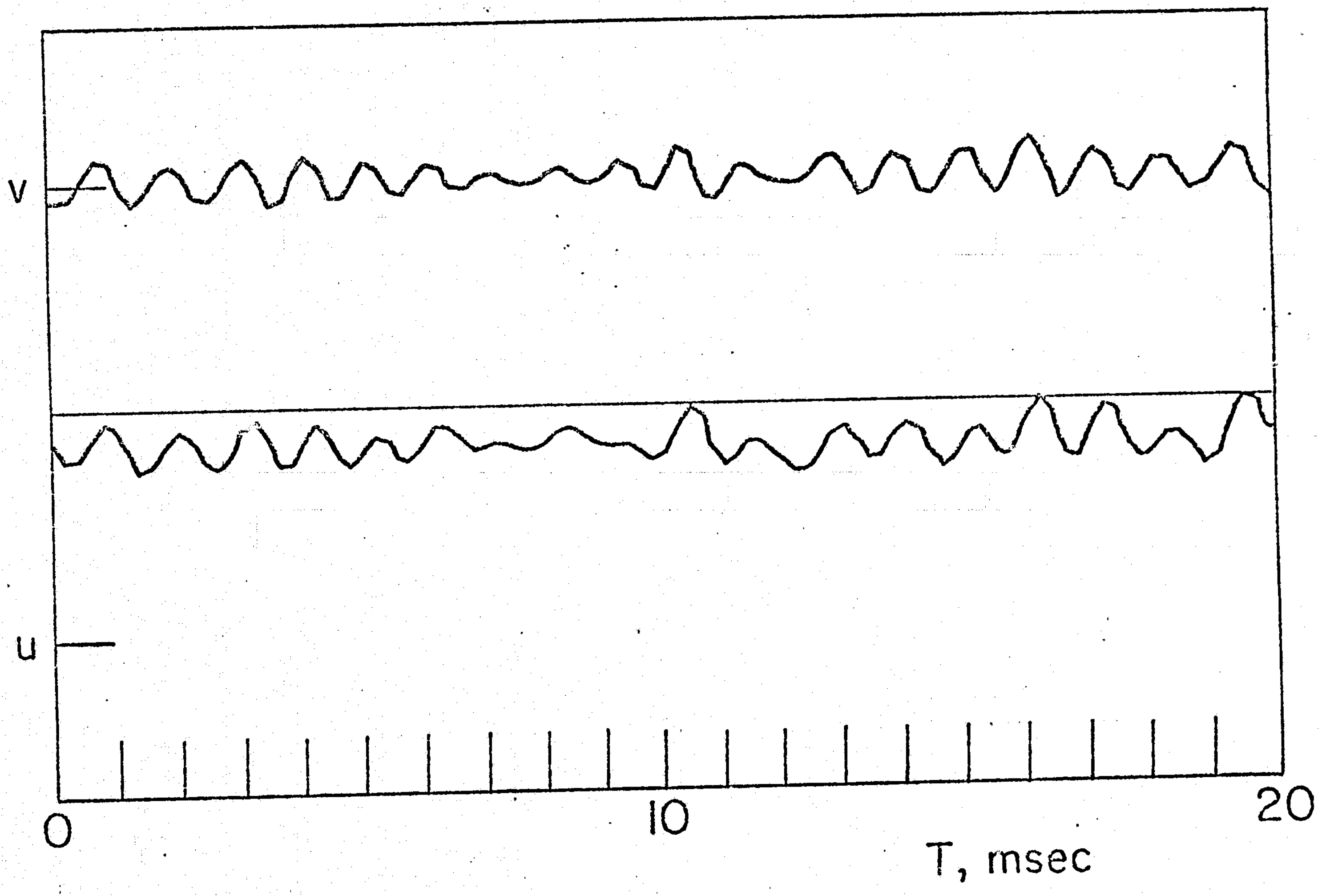

(b) x/D = 0.3, r/D = 0.5

Figure 29. Concluded.

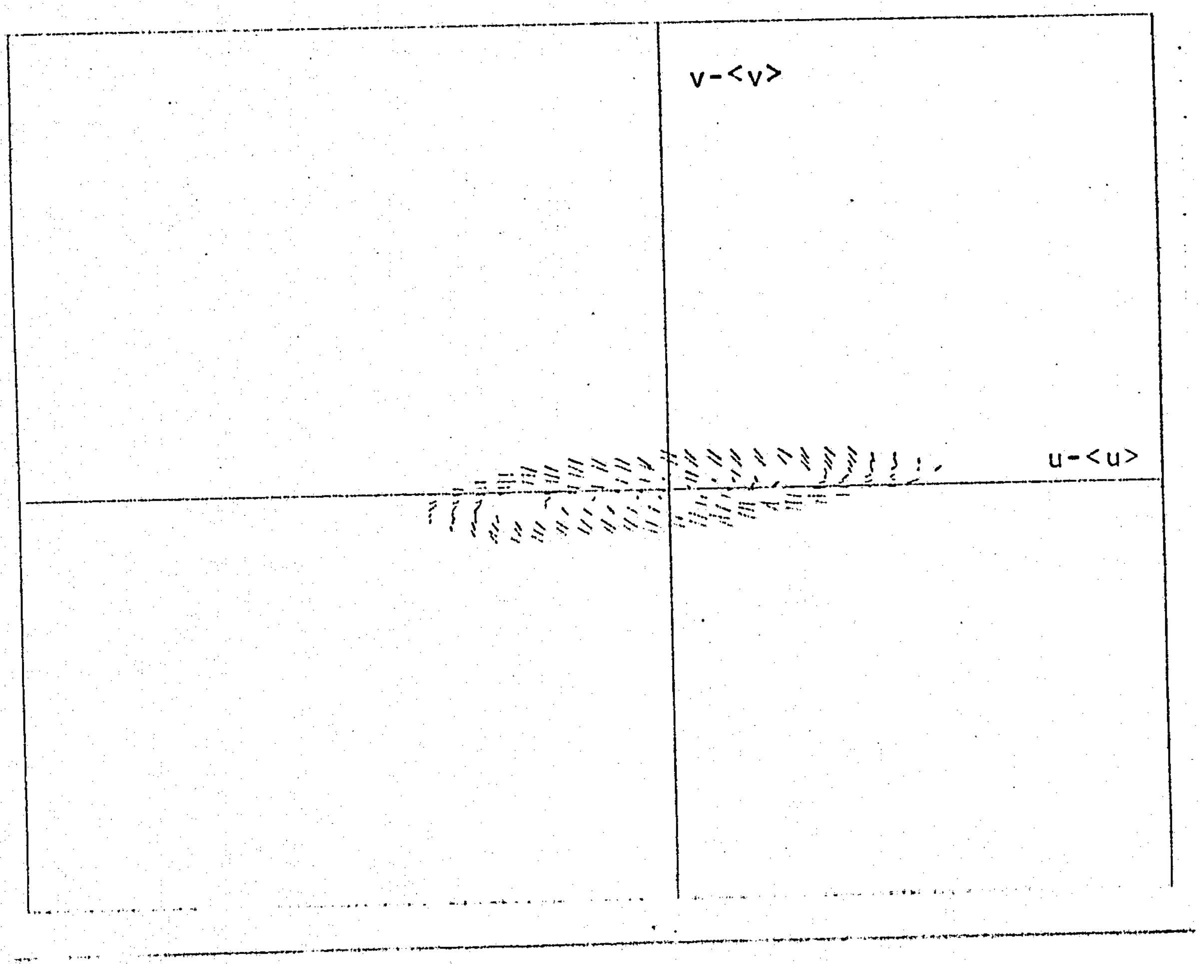

(a) x/D = 0.2, r/D = 0.5

Figure 30. Drift vectors: x/D = .2,.3

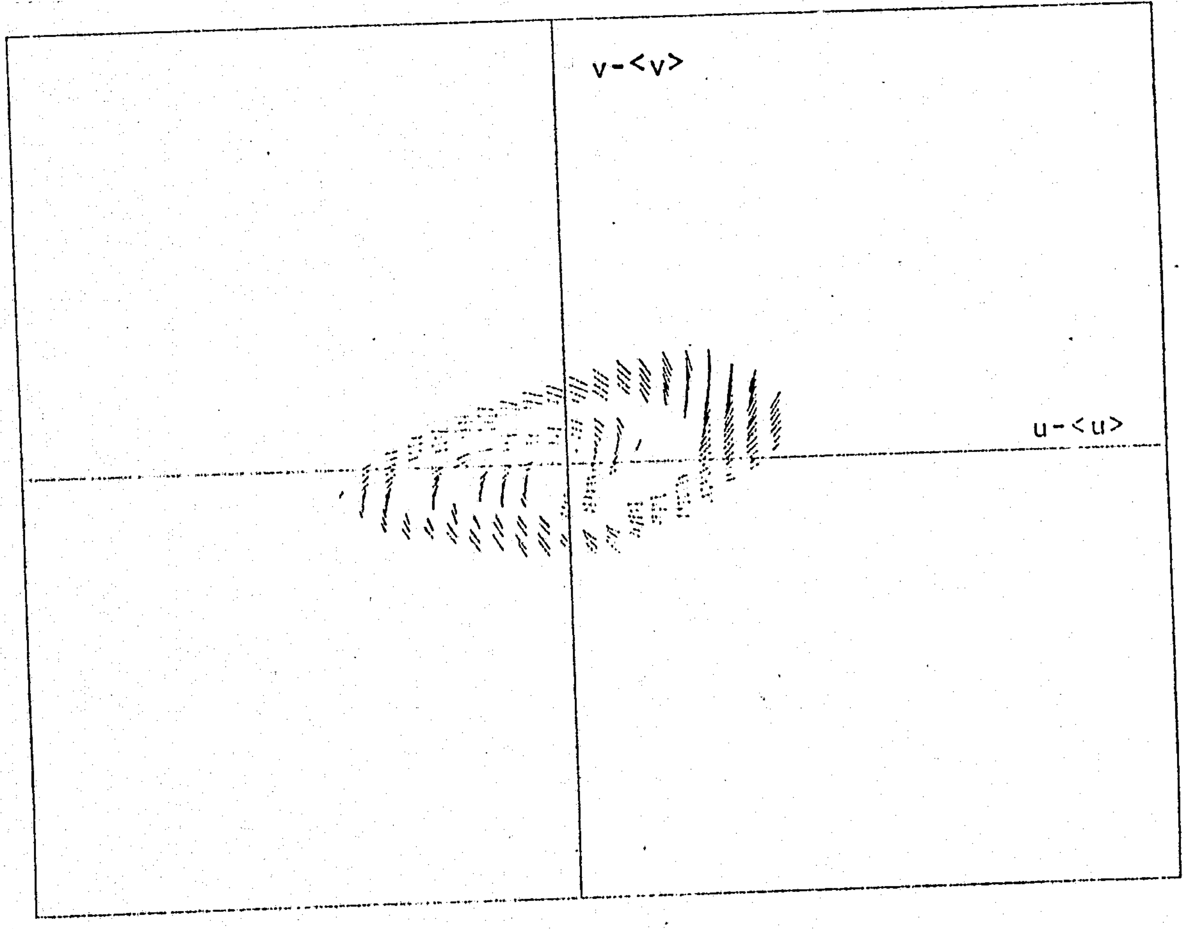

(b) x/D = 0.3, r/D = 0.5

Figure 30. Concluded.

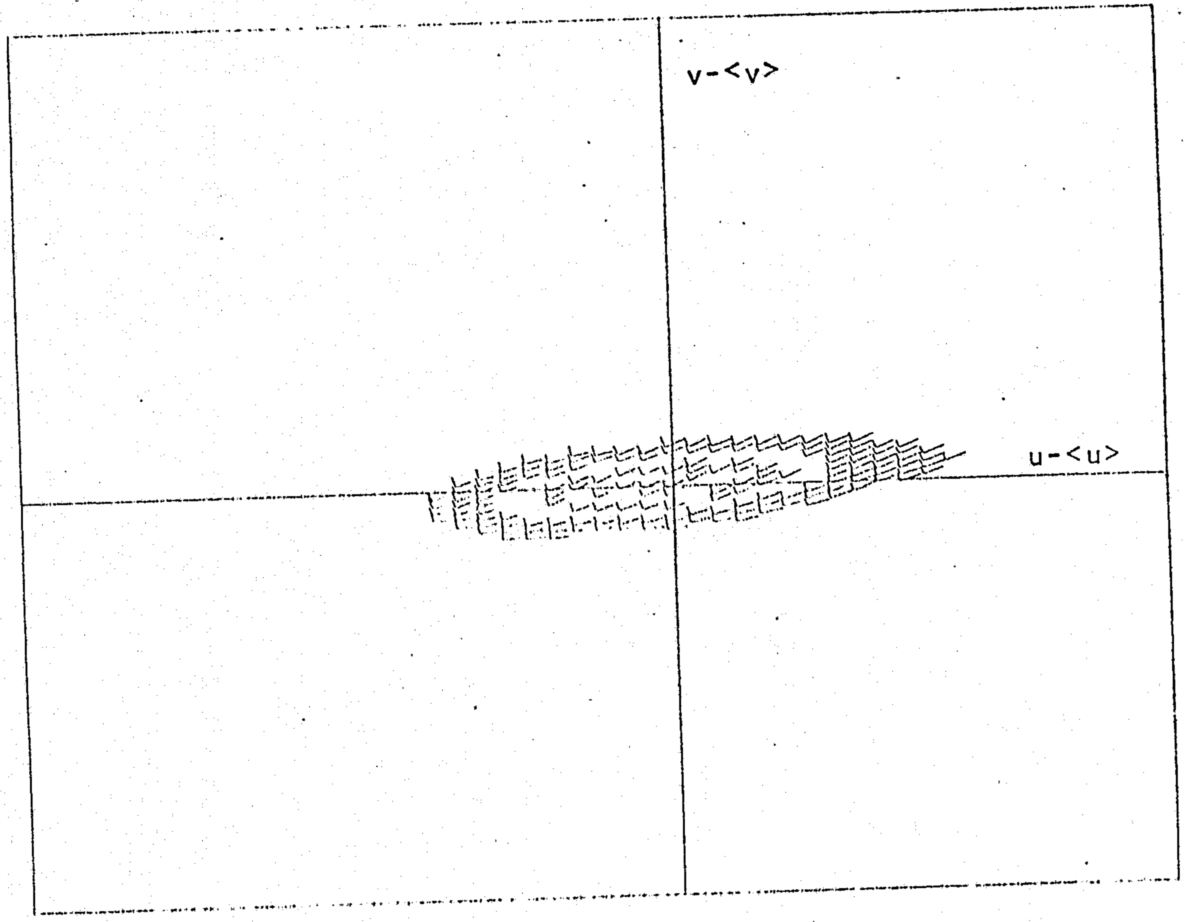

(a) x/D = 0.2, r/D = 0.5

Figure 31. Diffusion tensors: x/D = .2,.3

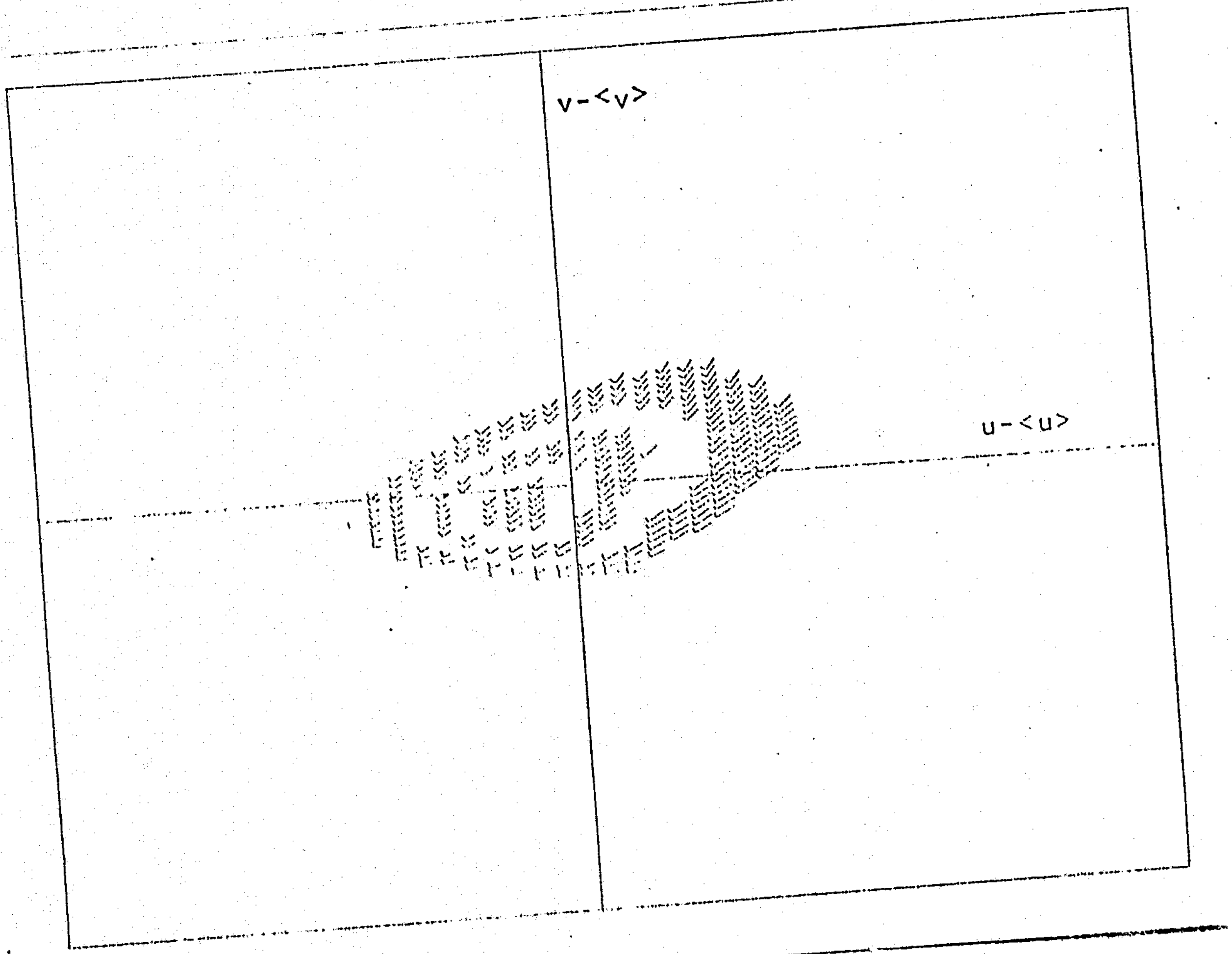

(b) x/D = 0.3, r/D = 0.5

Figure 31. Concluded.

6.3 Potential core region

Measurements were made midway along the potential core ($x/D = 2$), and towards the end of the core ($x/D = 4$). Two radial positions were selected for each axial station. Measured joint probability densities, sample velocity records, drift vectors, and diffusion tensors are presented as figures 32 - 35.

The figures above, in conjunction with figures 24 - 27, indicate the statistical parameters u'/U and u'/v' are nearly constant with downstream position while the shear stress slowly increases to a maximum near $x/D = 4$. DRIFT decreases with downstream distance while the ratio DIFFUSION/DRIFT increases roughly linearly with distance. All parameters except DRIFT increase across the shear layer away from the jet axis. However DRIFT is a measure of flow acceleration and will necessarily decrease as length scales increase.

For positive values of the similarity parameter, η, the joint probability densities (e.g. figure 32b) exhibit an "edge" in the third quadrant characterized by parallel, closely spaced contours. This effect becomes more pronounced with increasingly positive η. The drifts are relatively small near these "edges" while the diffusion

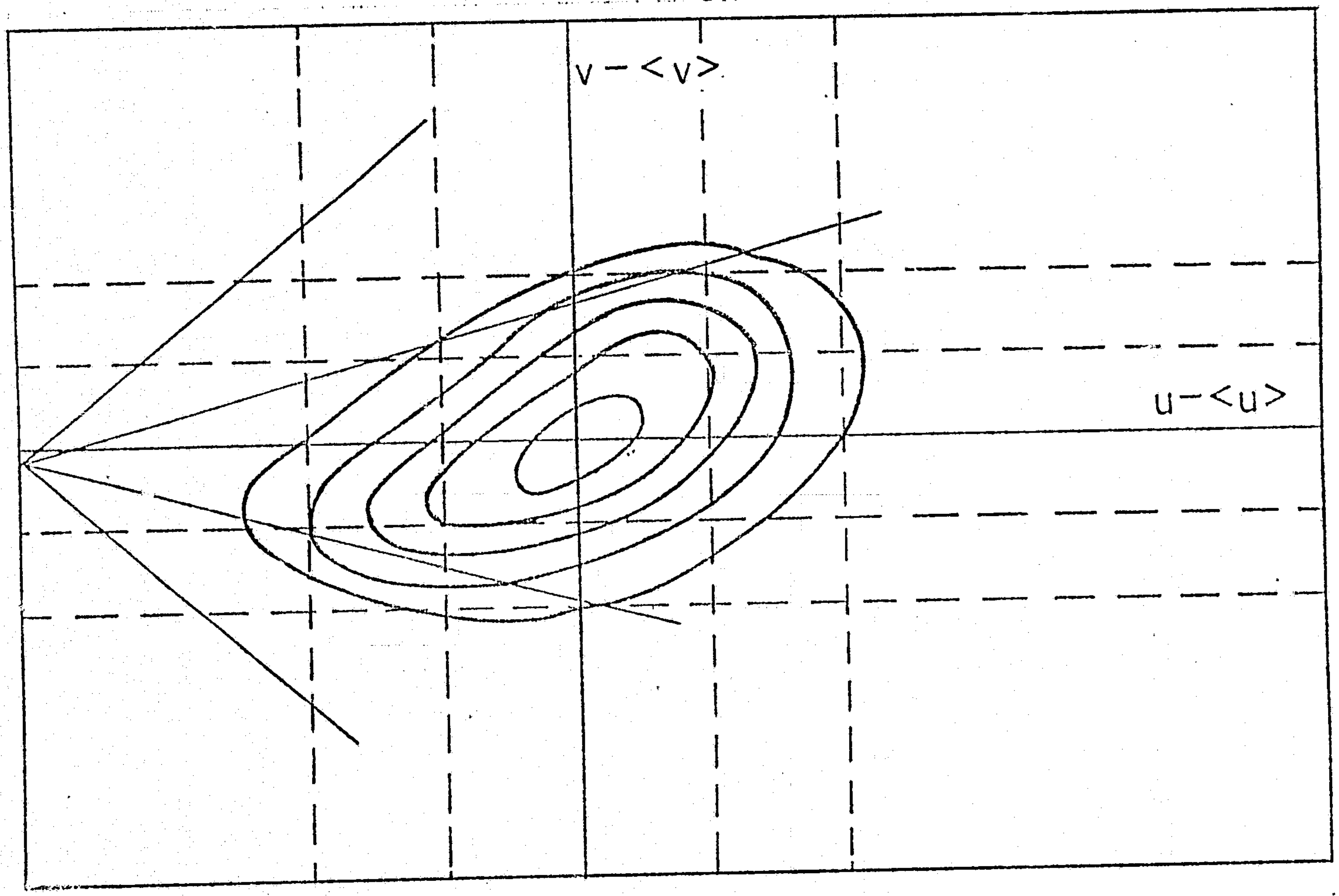

(a) x/D = 2, r/D = .5

Figure 32. Joint probability densities: x/D = 2, 4.

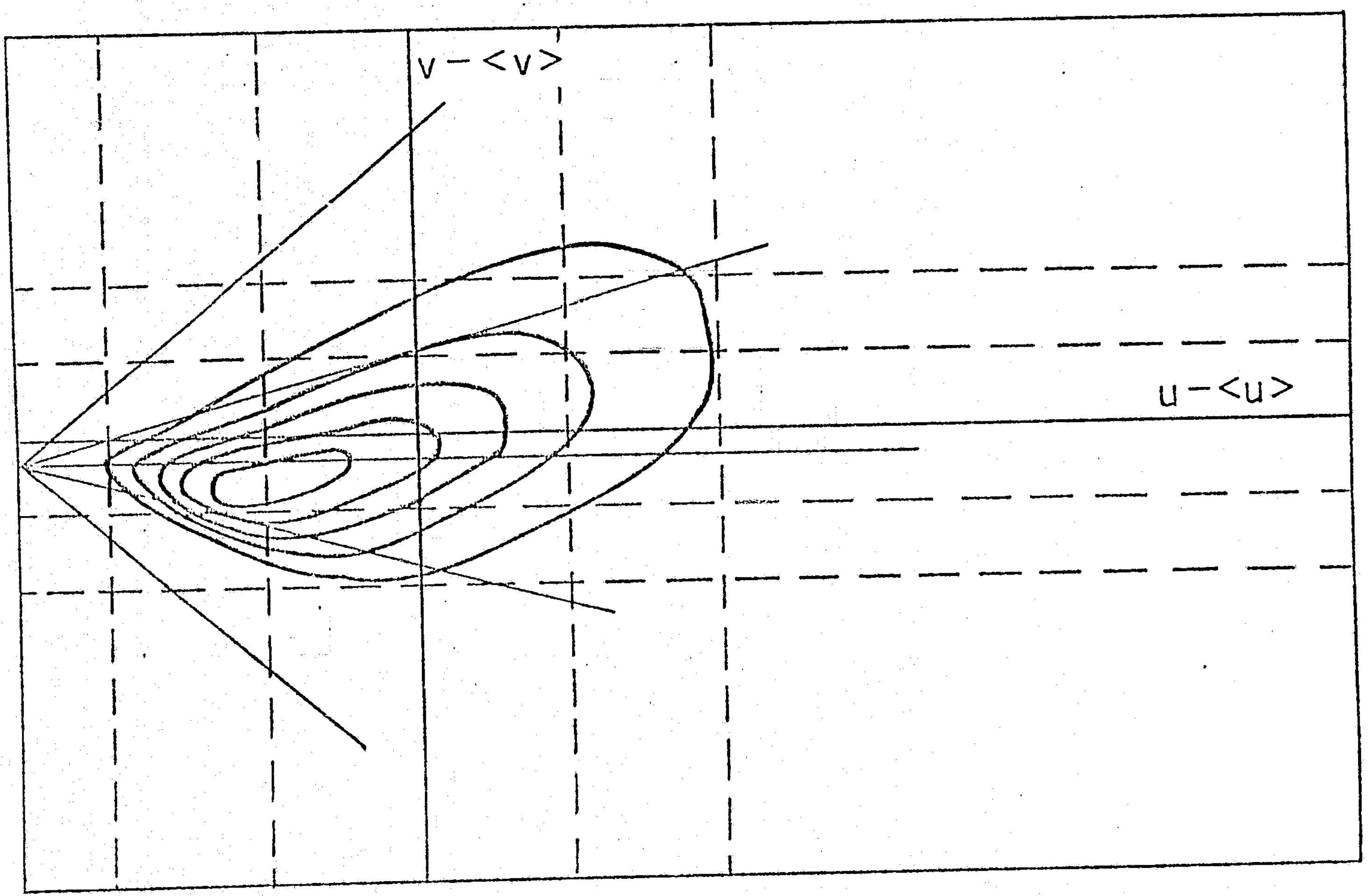

(b) x/D = 2.0, r/D = 0.6

Figure 32. Continued.

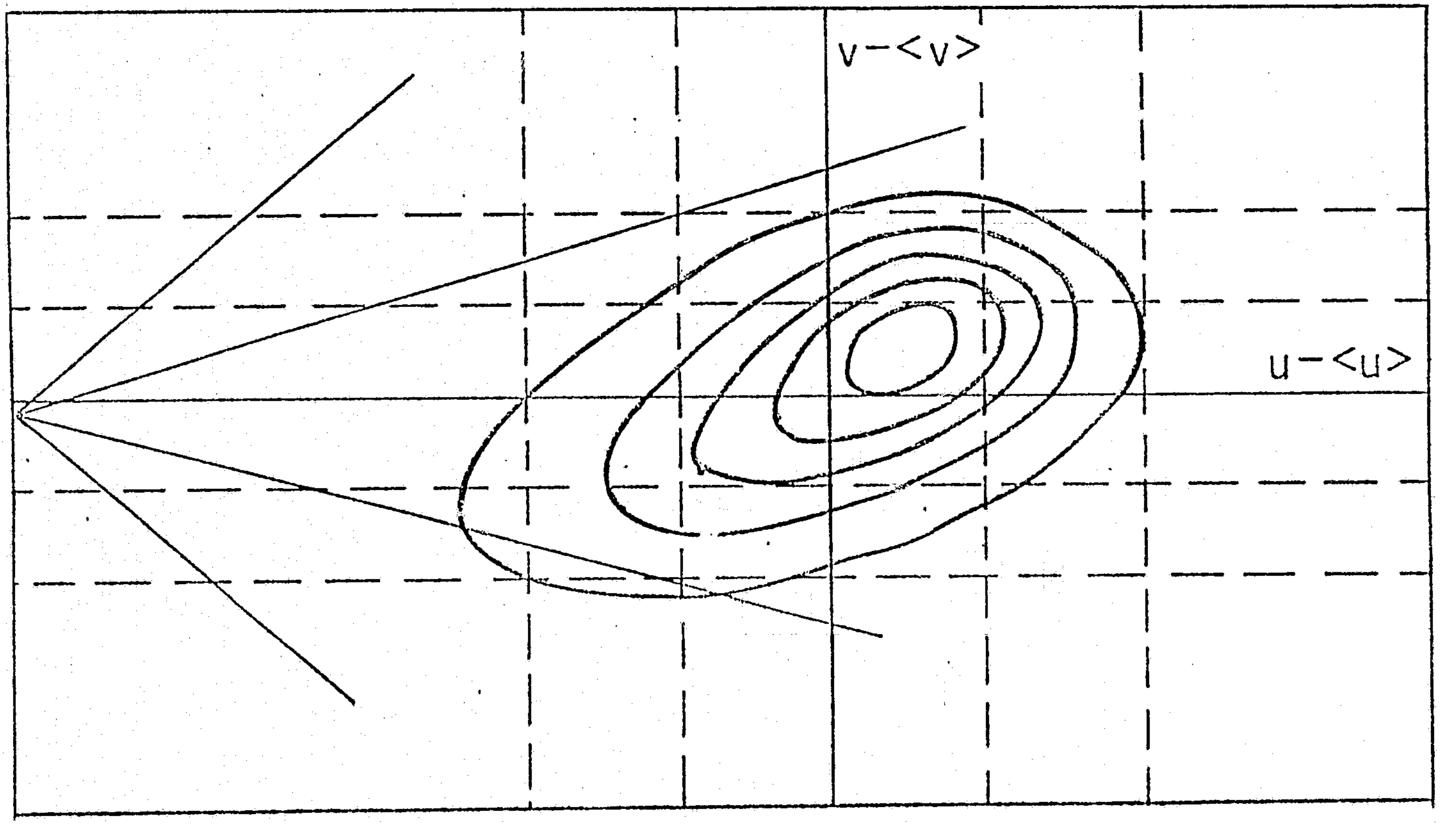

(c) x/D = 4.0, r/D = 0.4

Figure 32. Continued.

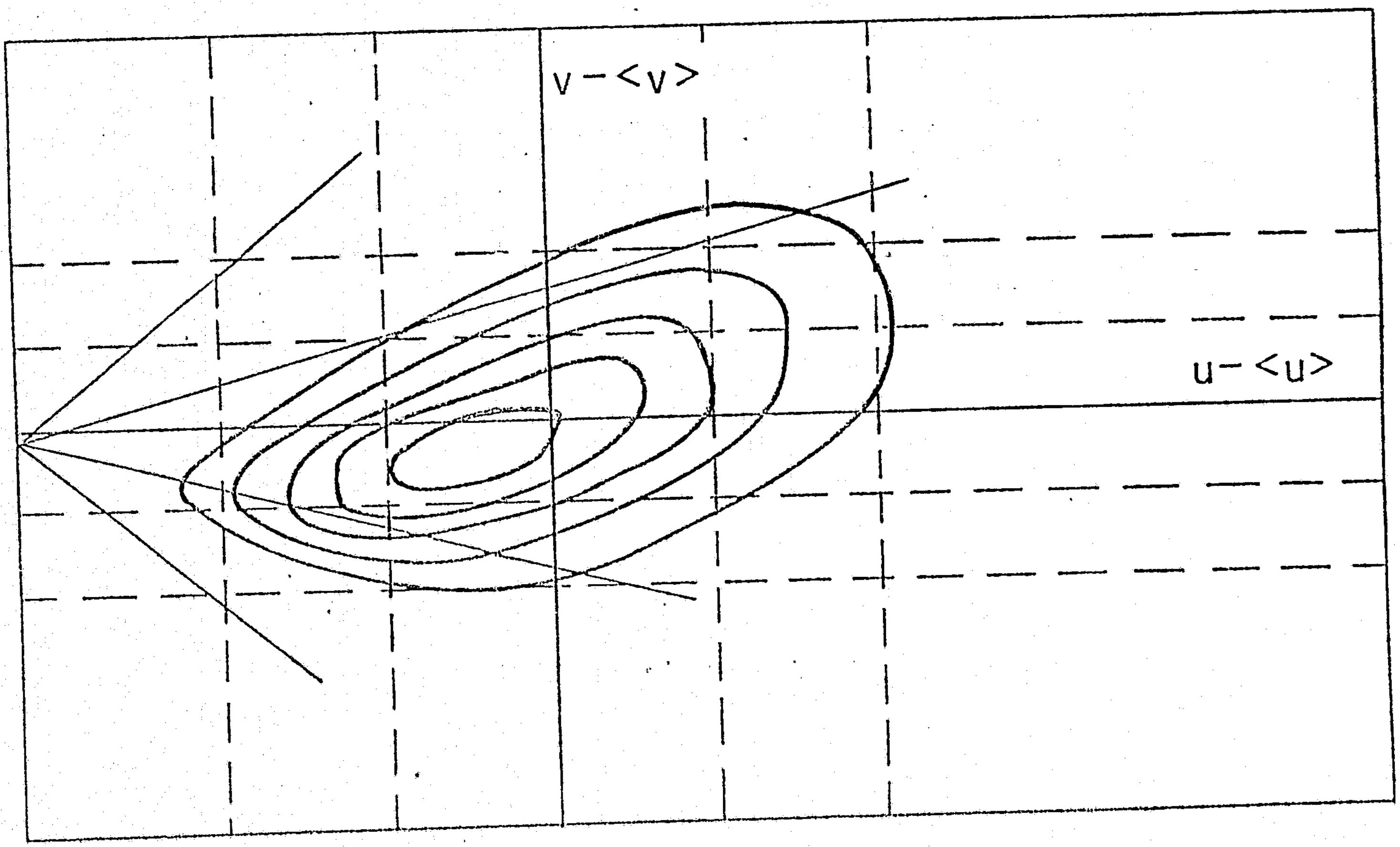

(d) x/D = 4.0, r/D = 0.6

Figure 32. Concluded.

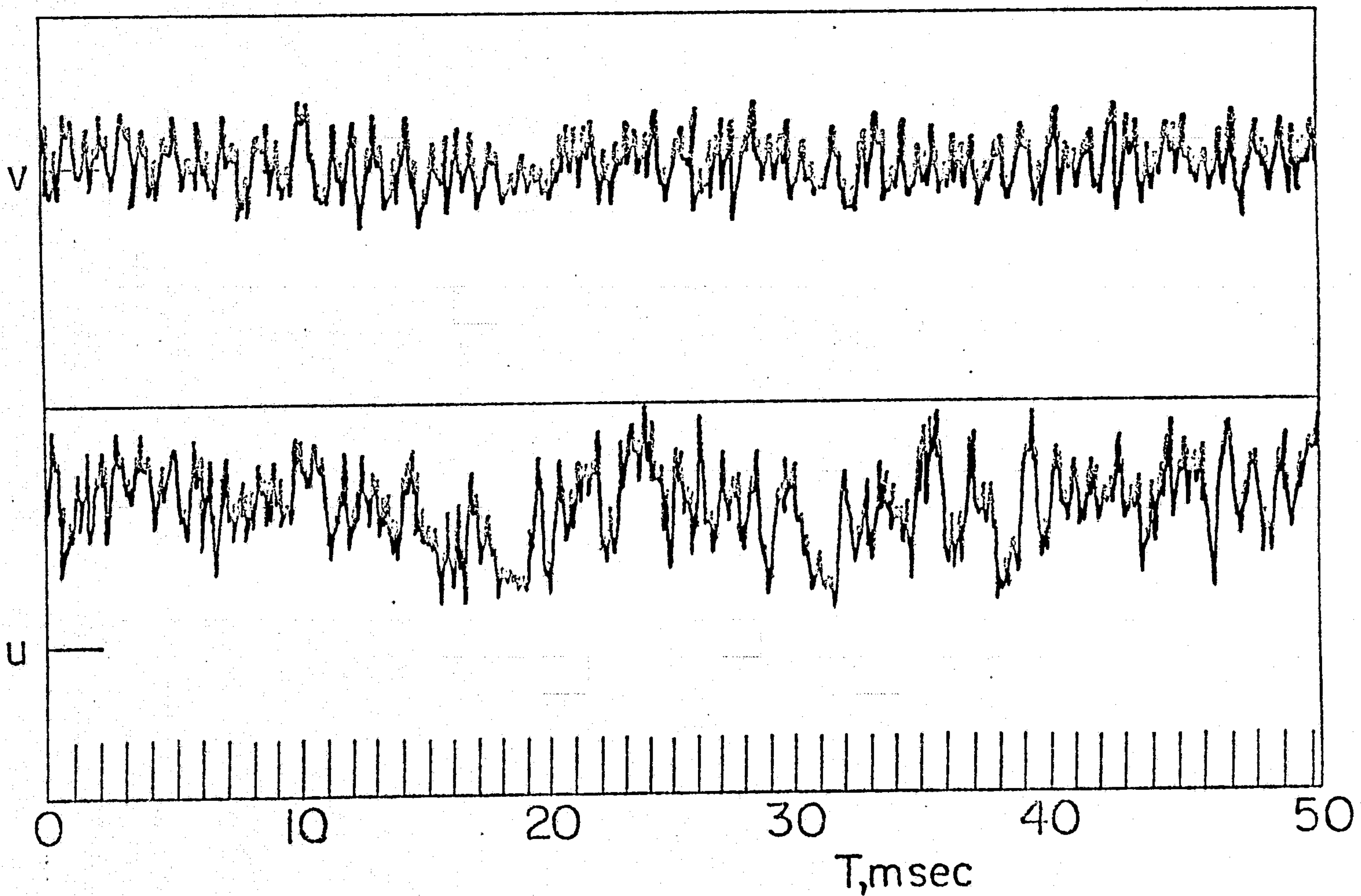

(a) x/D = 2.0; r/D = 0.5

Figure 33. Sample u,v velocity records: x/D = 2, 4.

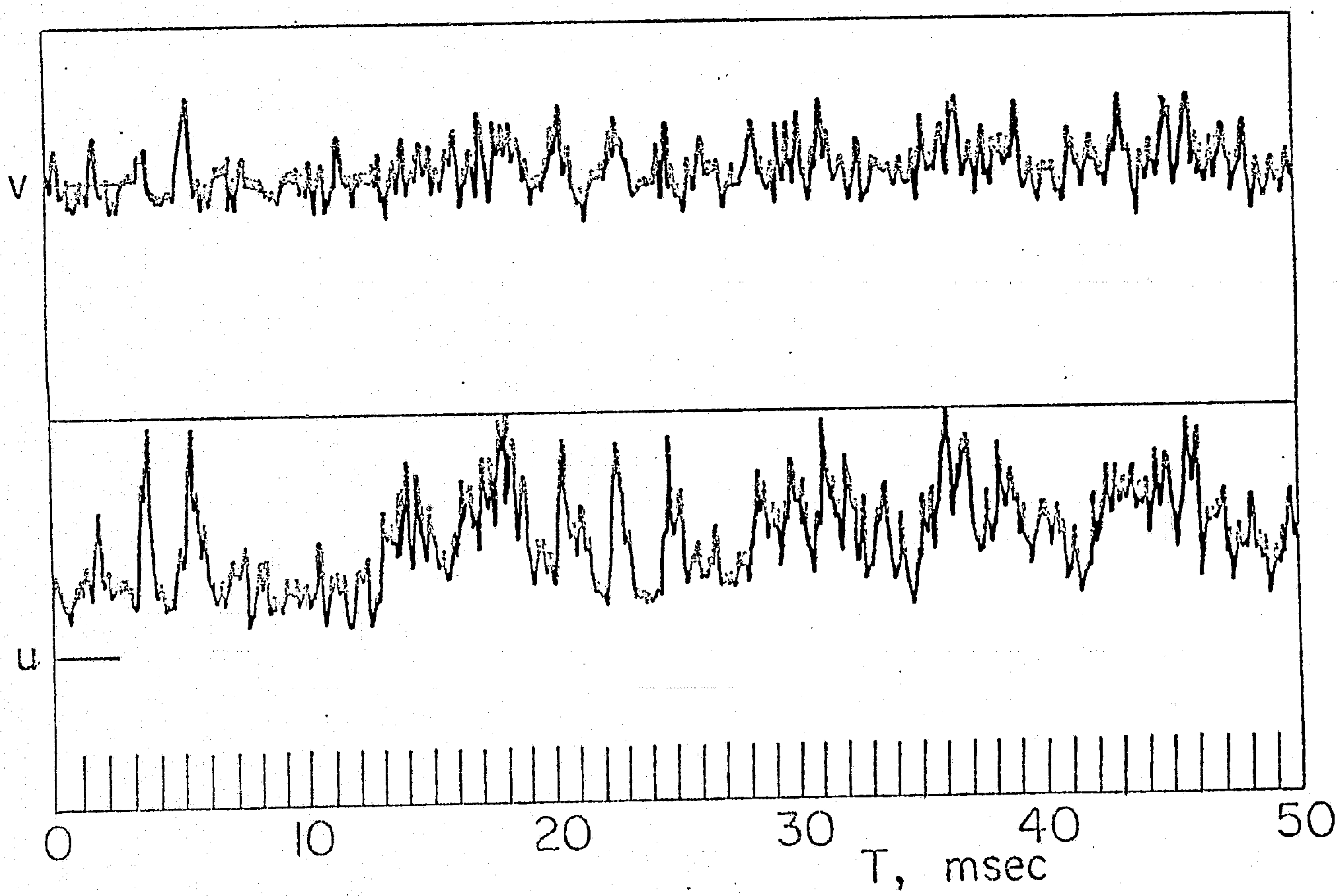

(b) x/D = 2.0, r/D = 0.6

Figure 33. Continued.

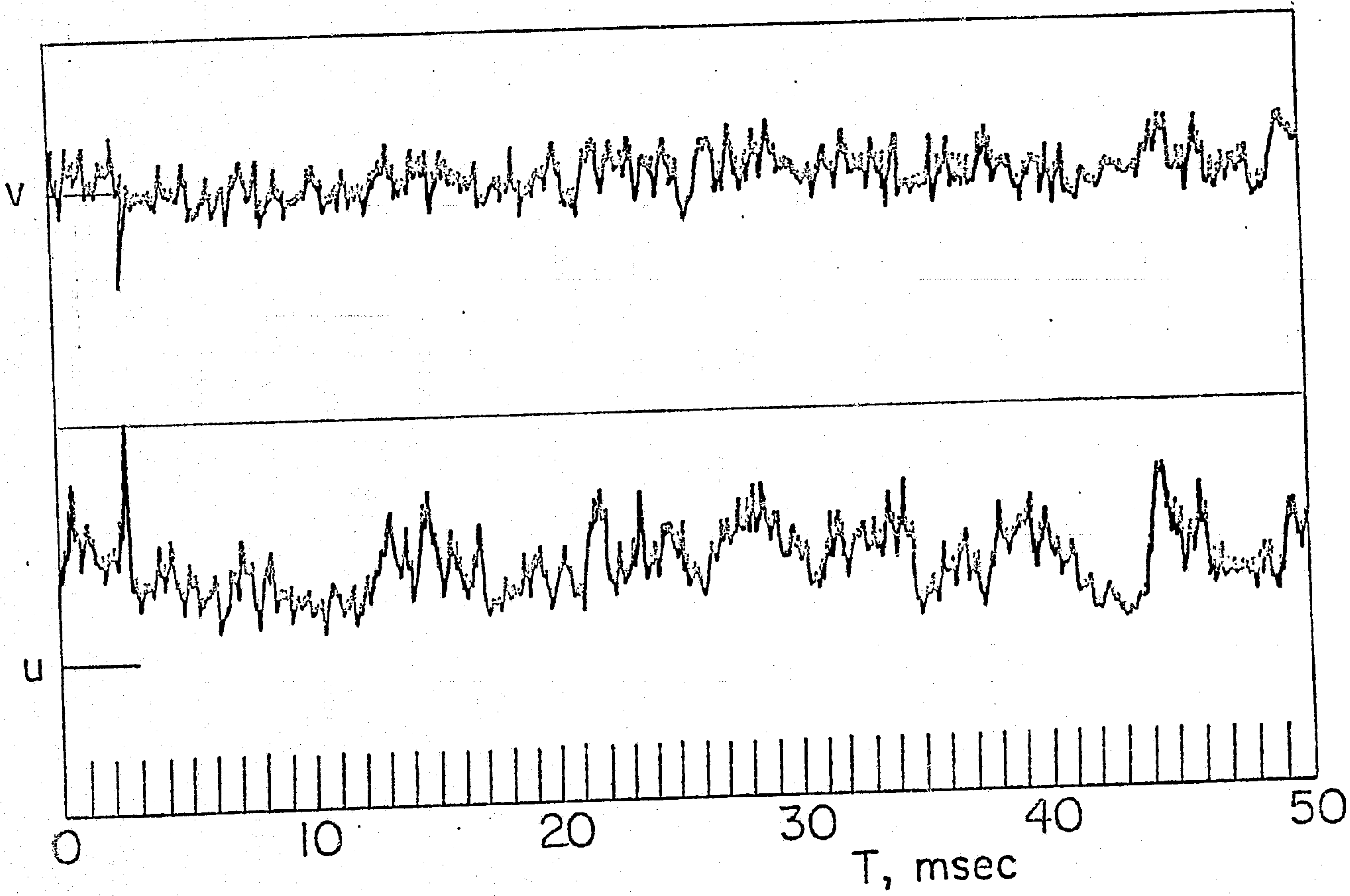

(c) x/D = 4.0, r/D = 0.6

Figure 33. Concluded.

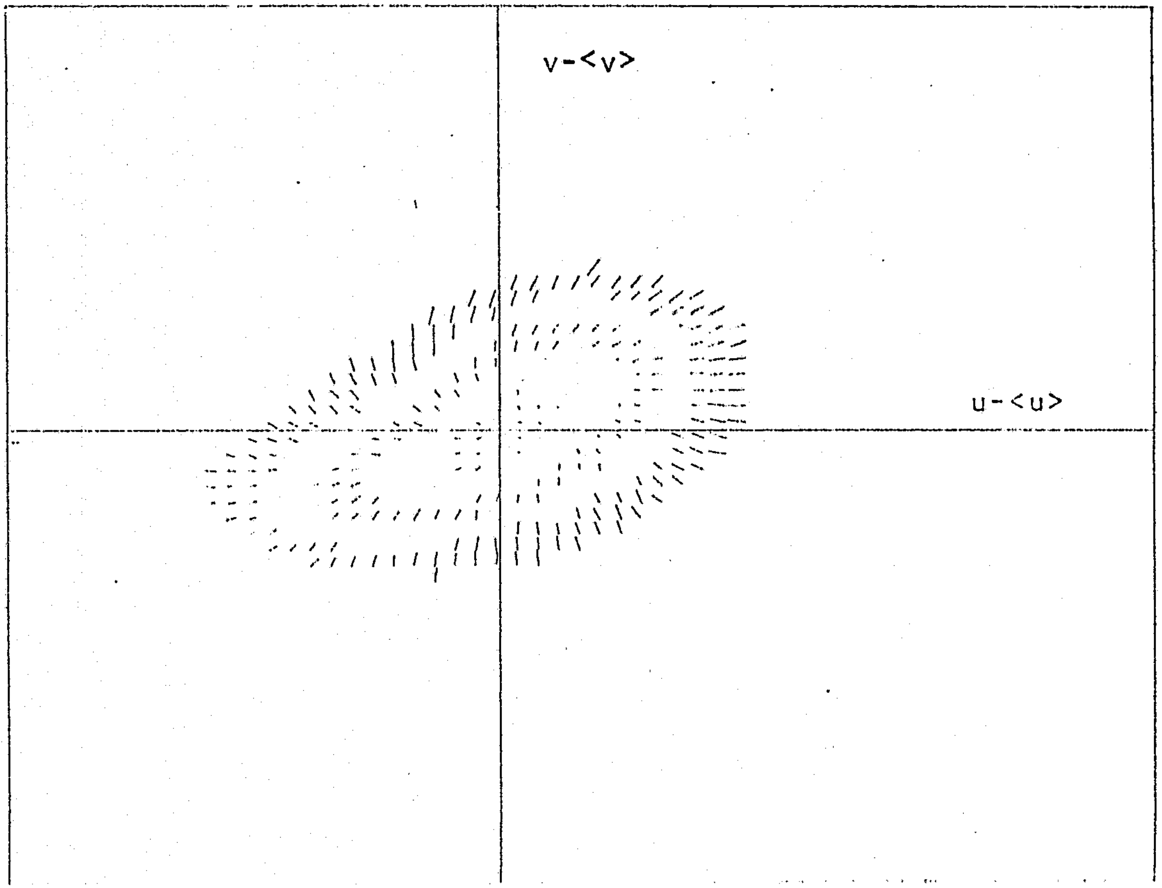

(a) x/D = 2.0, r/D = 0.5

Figure 34. Drift Vectors: x/D = 2, 4

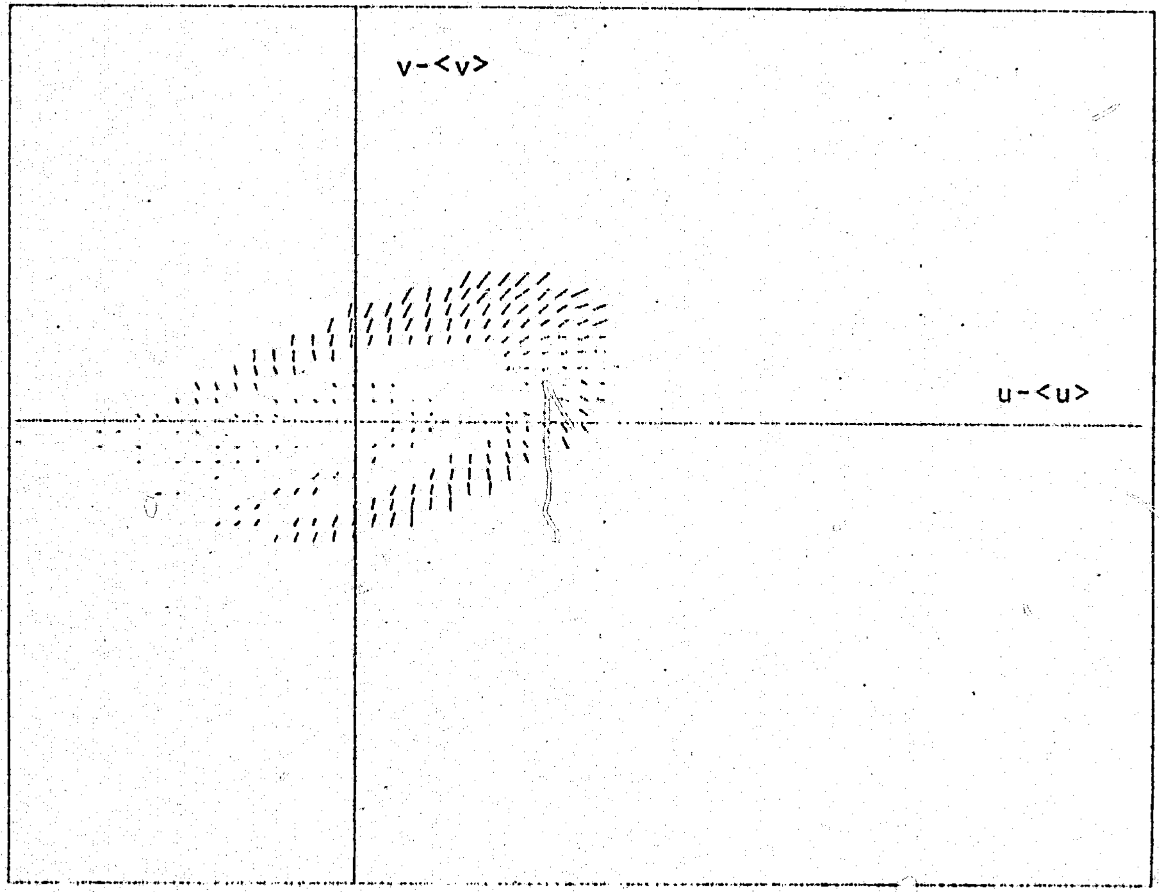

(b) x/D = 2.0, r/D = .6

Figure 34. Continued.

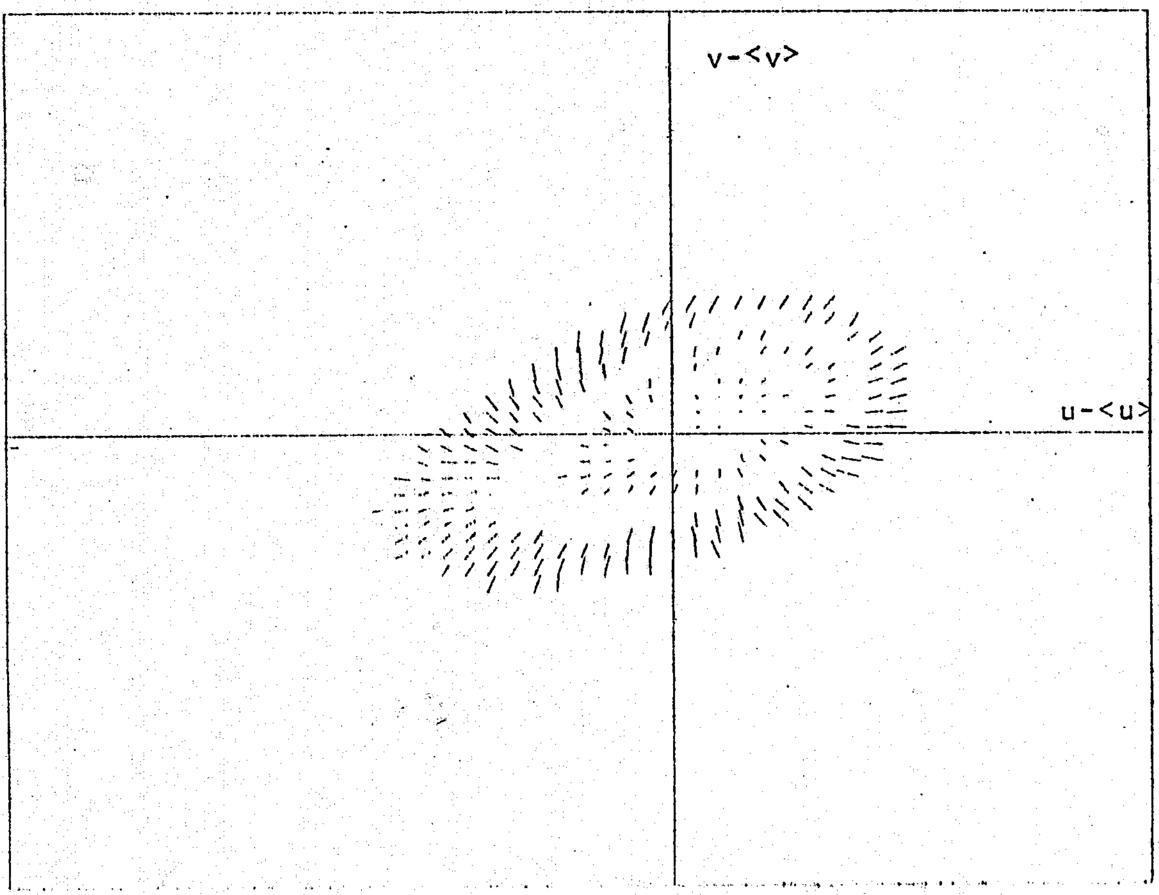

(c) x/D = 4.0, r/D = 0.4

Figure 34. Continued.

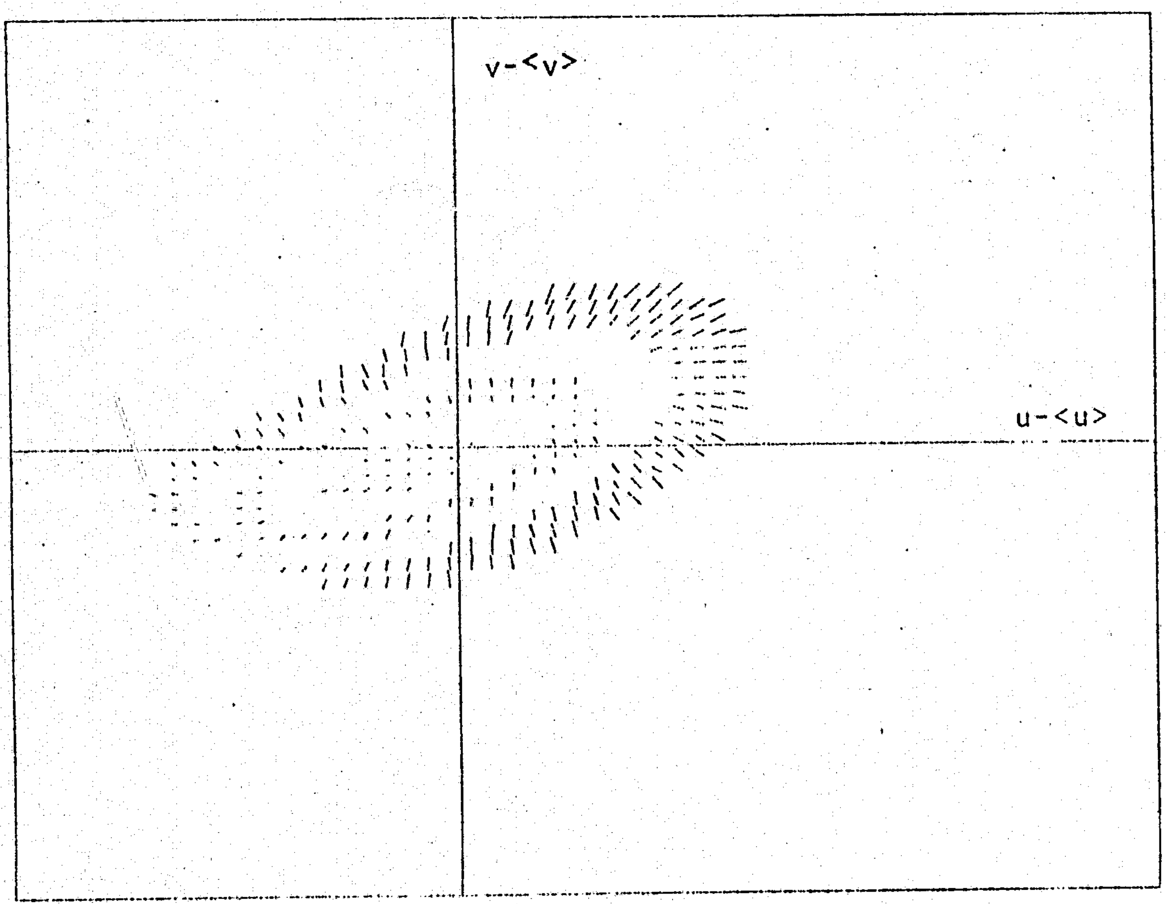

(d) x/D = 4.0, r/D = 0.6

Figure 34. Concluded.

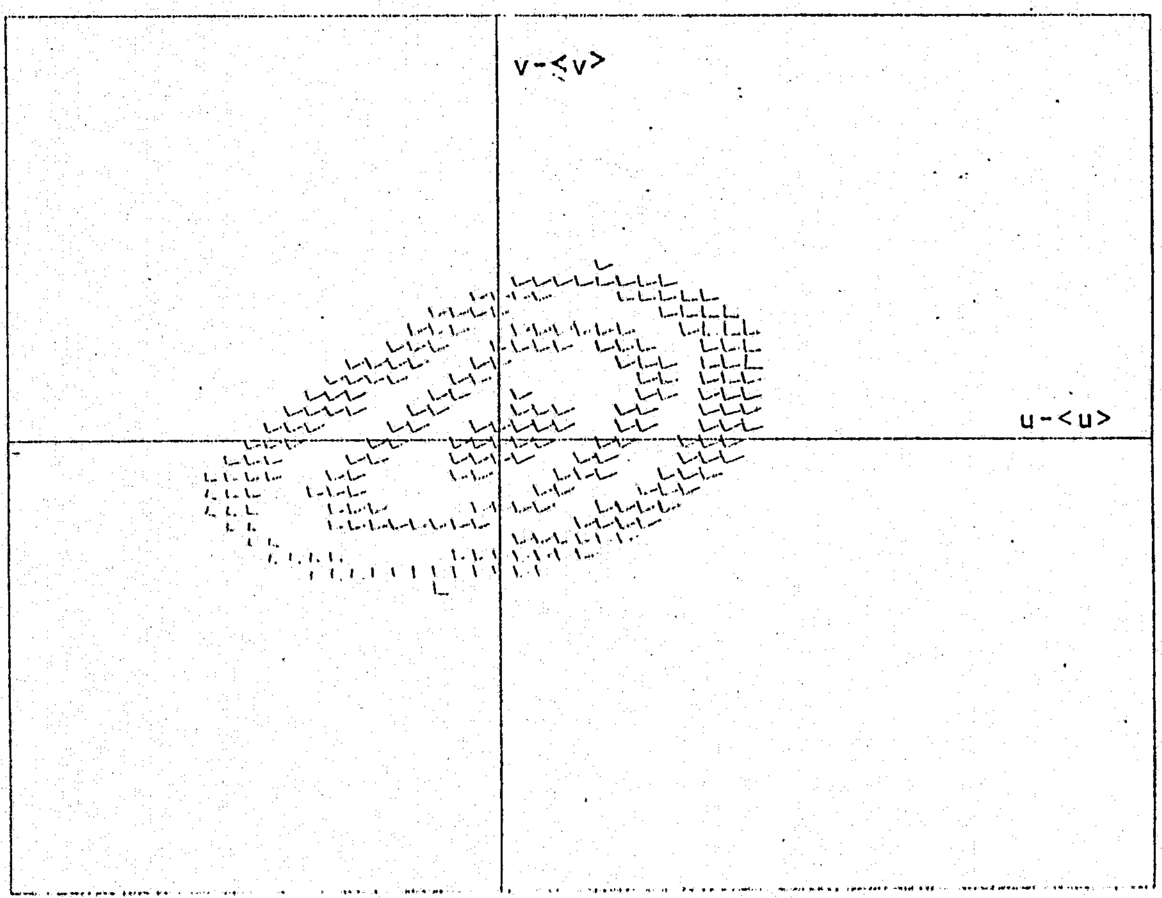

(a) x/D = 2.0, r/D = 0.5

Figure 35. Diffusion tensors: x/D = 2, 4.

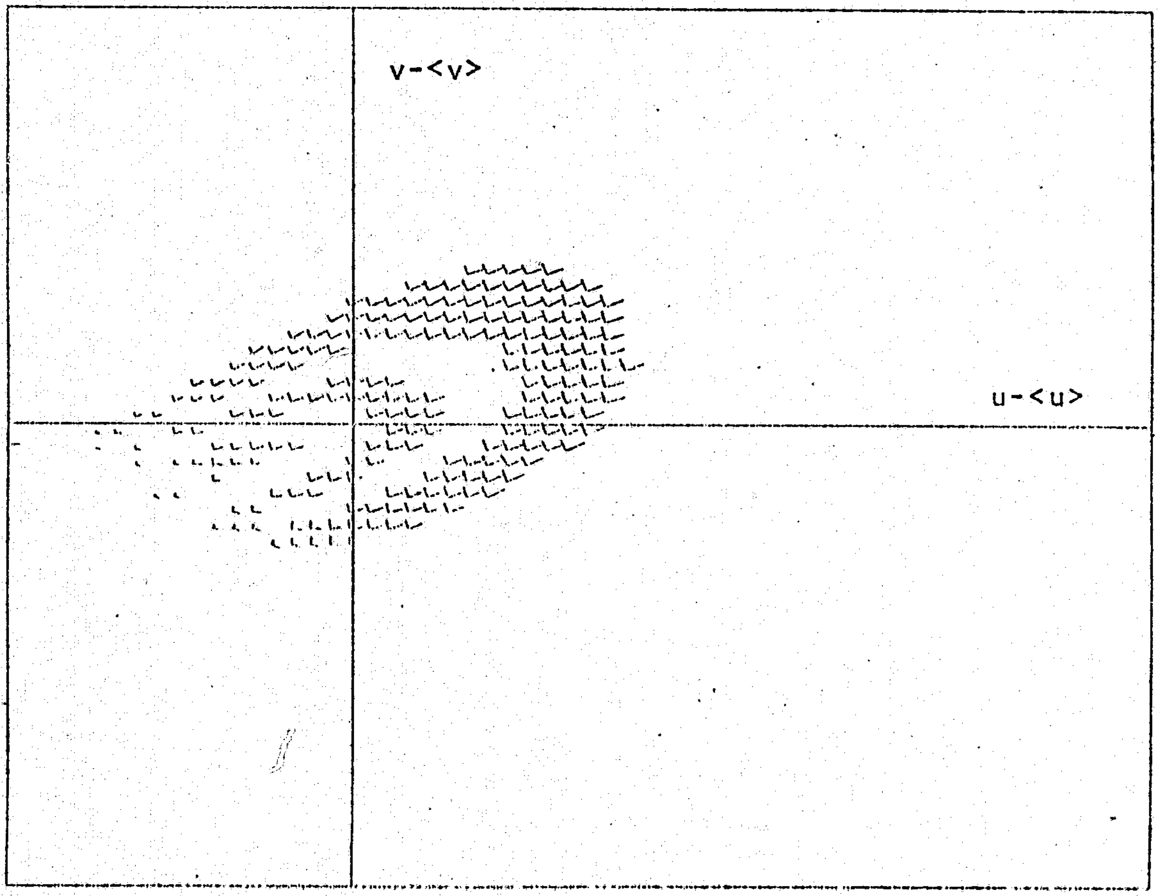

(b) x/D = 2.0, r/D = 0.6

Figure 35. Continued.

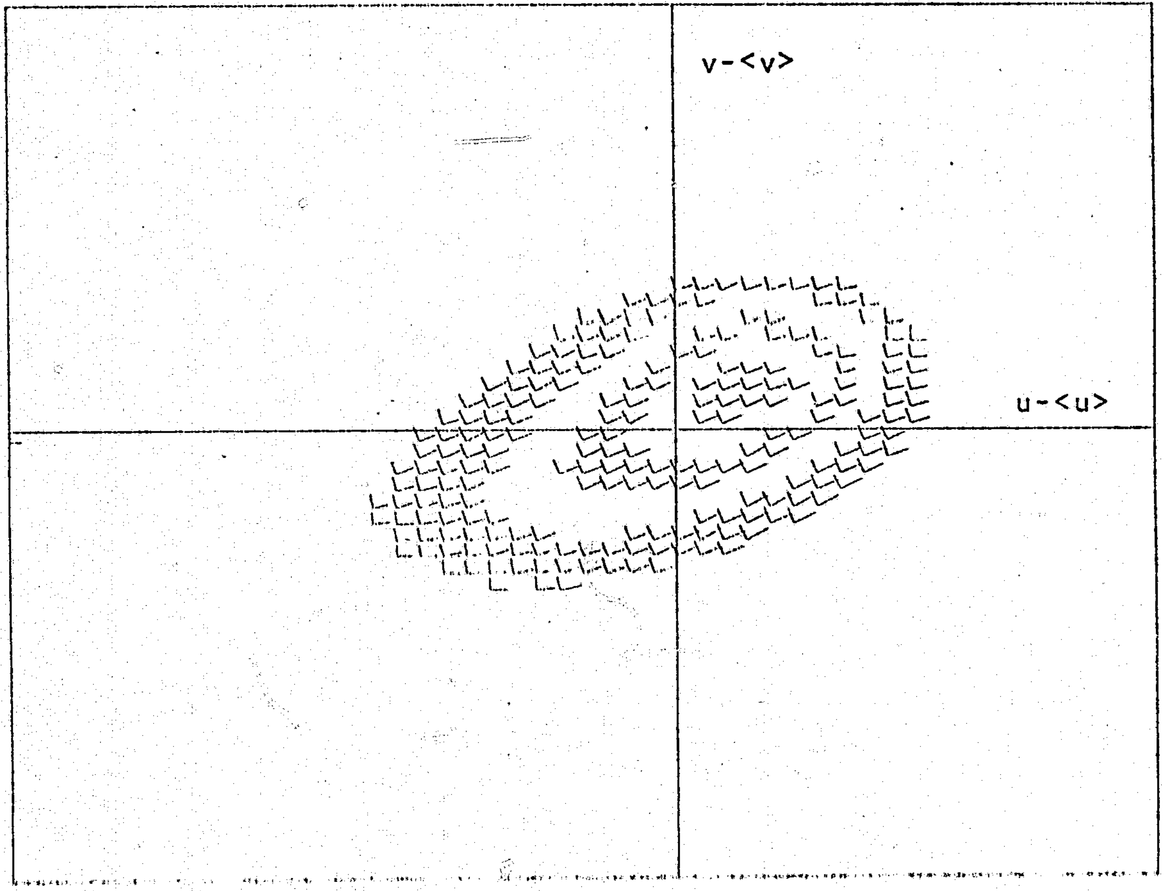

(c) x/D = 4.0, r/D = 0.4

Figure 35. Continued.

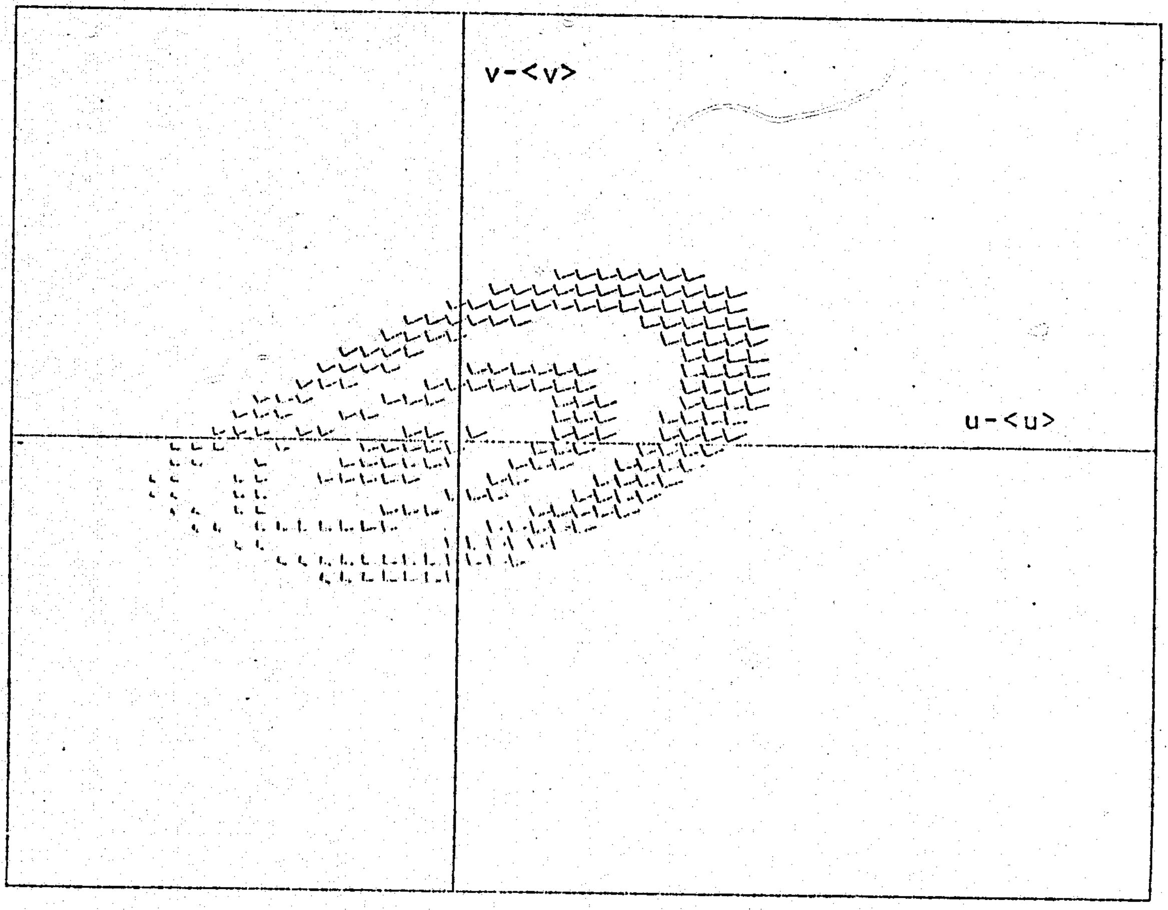

(d) x/D = 4.0, r/D = 0.6

Figure 35. Concluded.

tensors become small and anisotropic, with major axes aligned parallel to the edge (e.g. figures 34b and 35b). The significance of the edges is unclear, and may simply be an effect of the calibration. The edges lie along angles in the hodograph plane that are generally outside of the calibration domain.

6.4 Transitional mixing region

Since the most intense noise producing region of a subsonic jet has been measured to be around eight diameters downstream from the nozzle, this region was examined in detail. Data was taken on the jet axis ($r/D = 0$), at the radial position of maximum turbulence ($r/D = .5$), and at the outer edge of the jet ($r/D = 1.0$), where the turbulence is intermittent. For completeness additional data was recorded at ($x/D = 12$, $r/D = .5$). The joint statistics as well as velocity records are shown in figures 36 - 39.

Statistically there is nothing strikingly unique about this region except that the mixing occupies a greater volume. For the most part the statistical parameters are similar in magnitude to those in the potential core region, and decay slowly with downstream distance (figures 24 and 26). The exception is the DIFFUSION/DRIFT ratio which continues to increase linearly with x/D. Consequently at

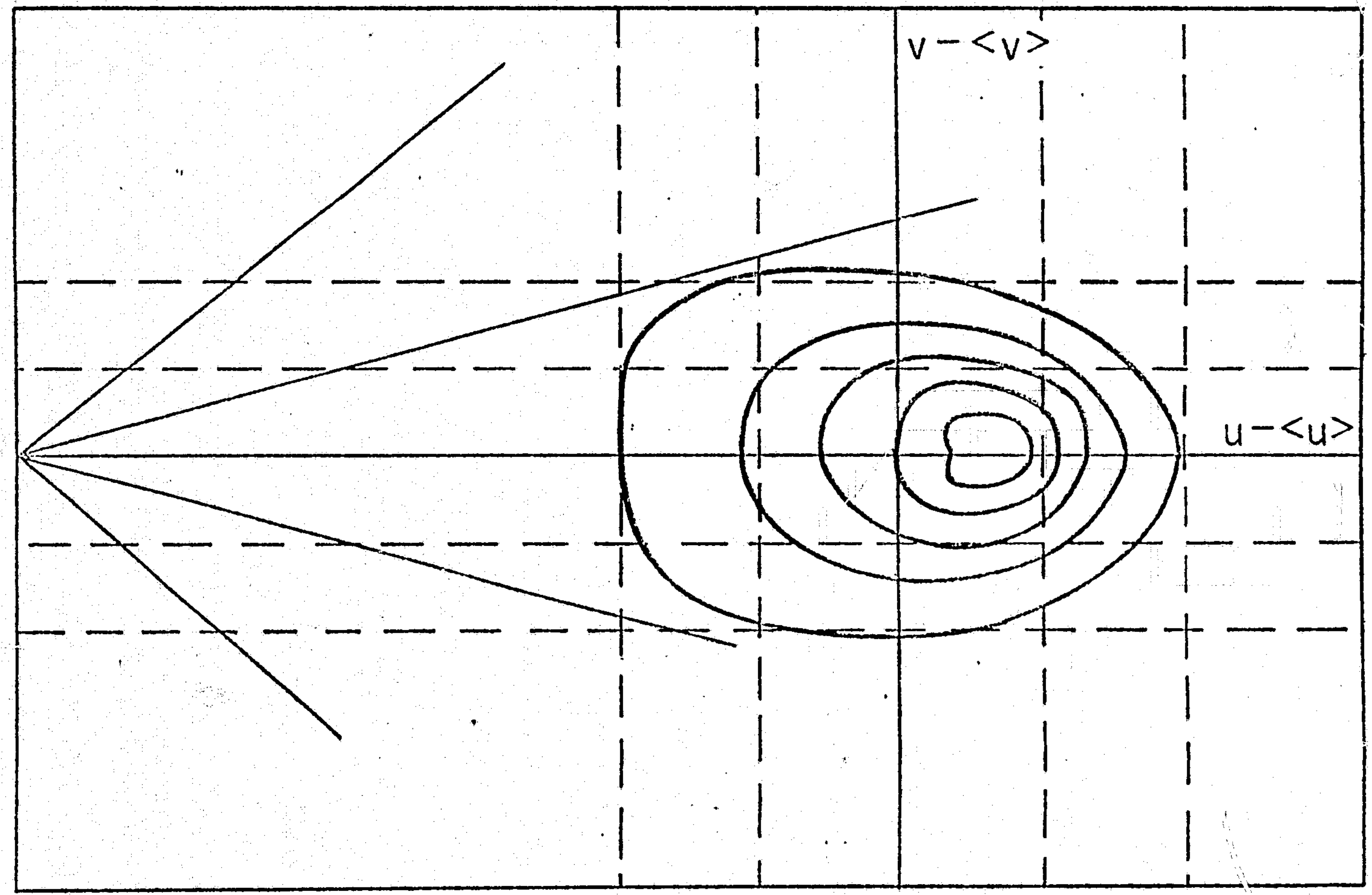

(a) x/D = 8.0, r/D = 0

Figure 36. Joint probability densities: x/D = 8, 12

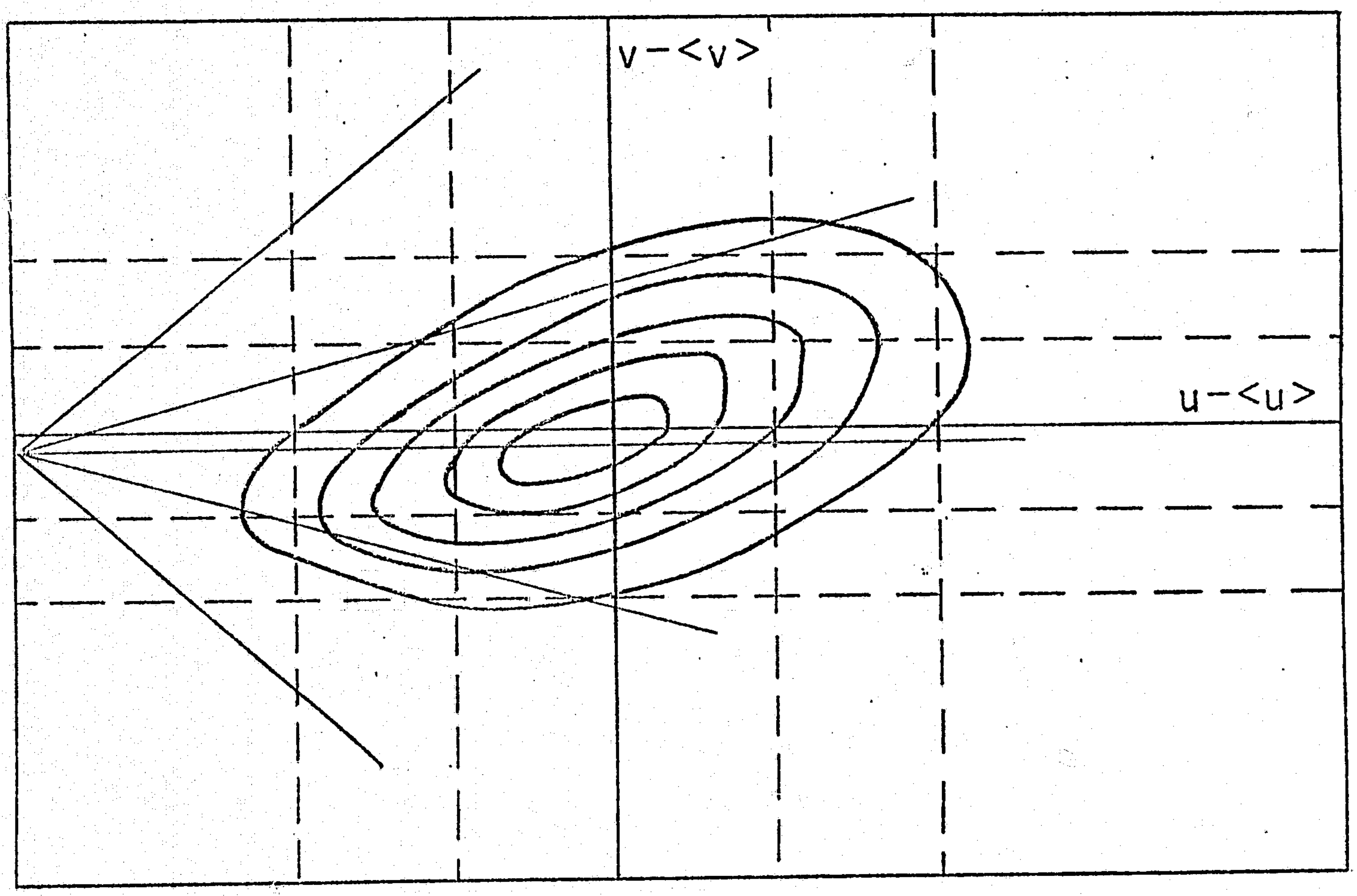

(b) x/D = 8.0, r/D = 0.5

Figure 36. Continued.

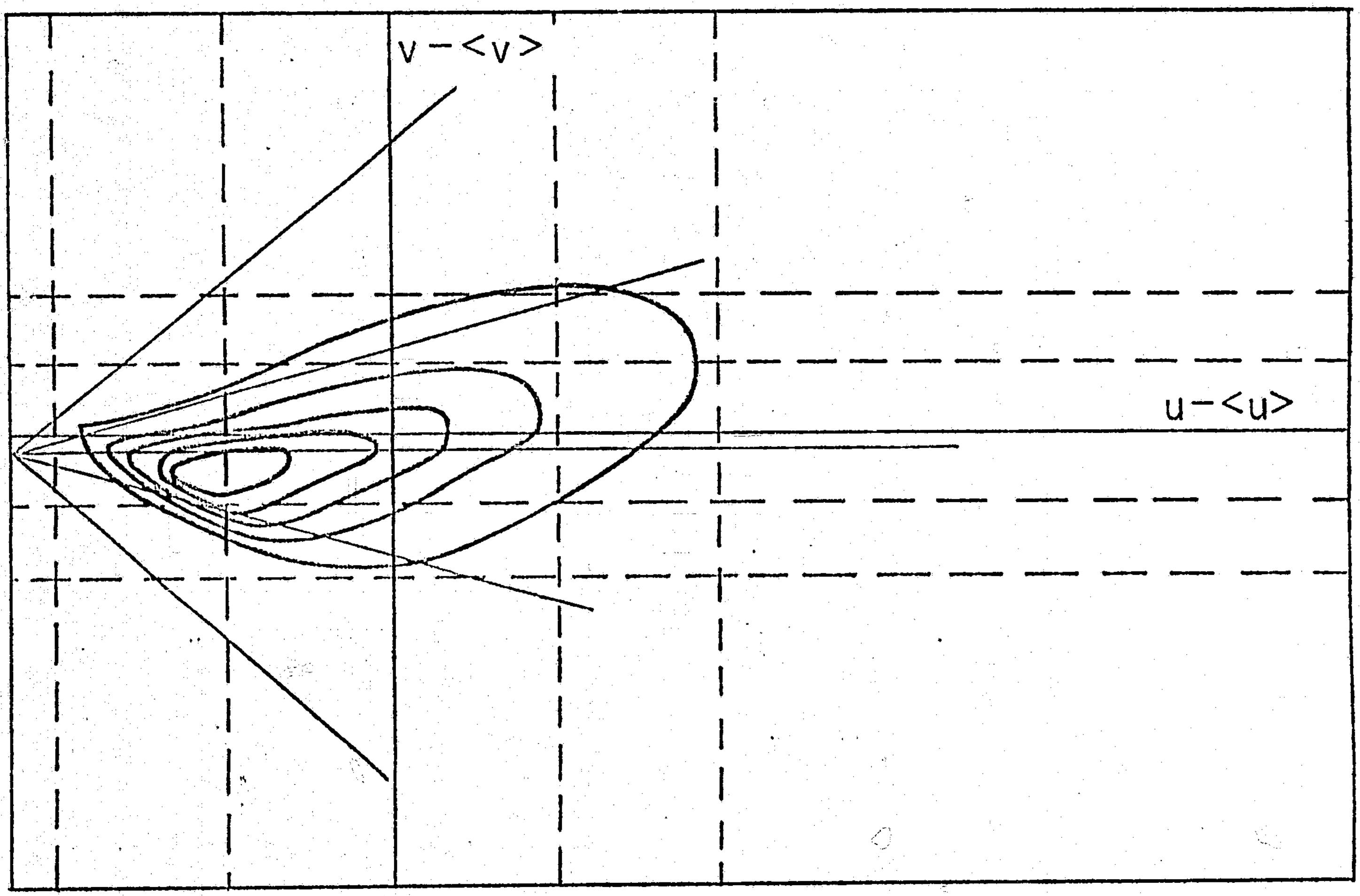

(c) x/D = 8.0, r/D = 1.0

Figure 36. Continued.

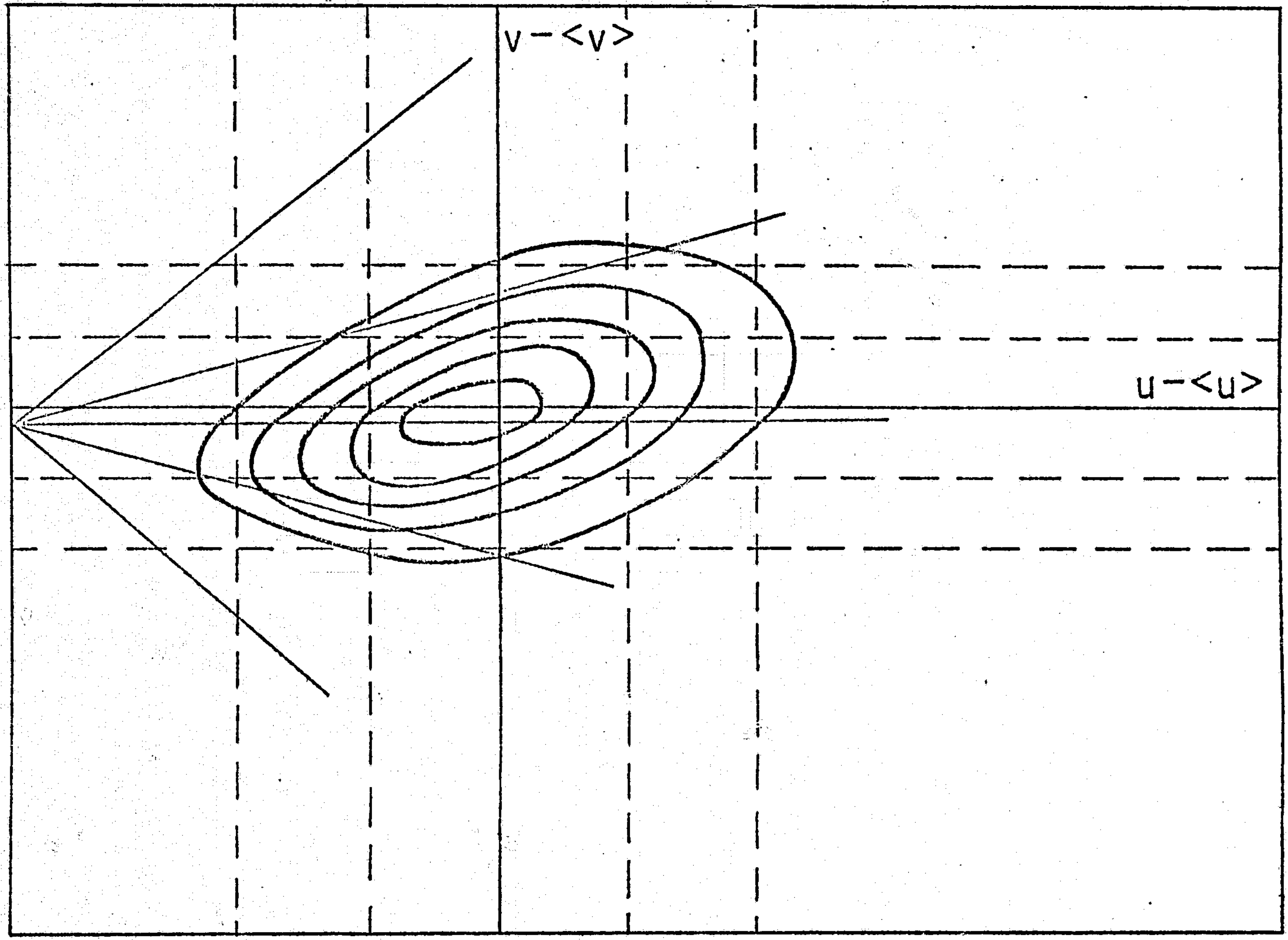

(d) x/D = 12.0, r/D = 0.5

Figure 36. Concluded.

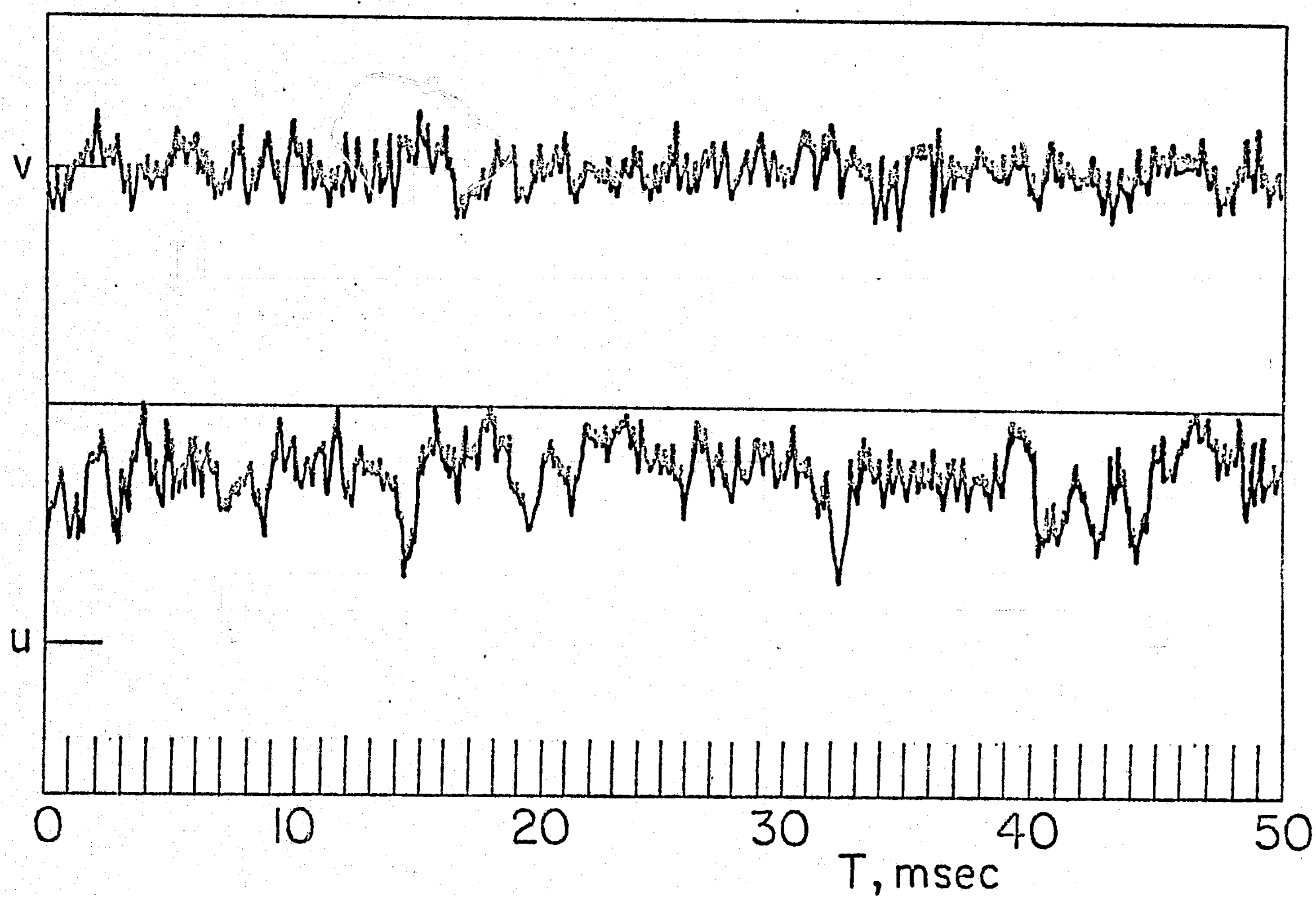

(a) x/D = 8.0, r/D = 0

Figure 37. Sample u,v velocity records: x/D = 8, 12

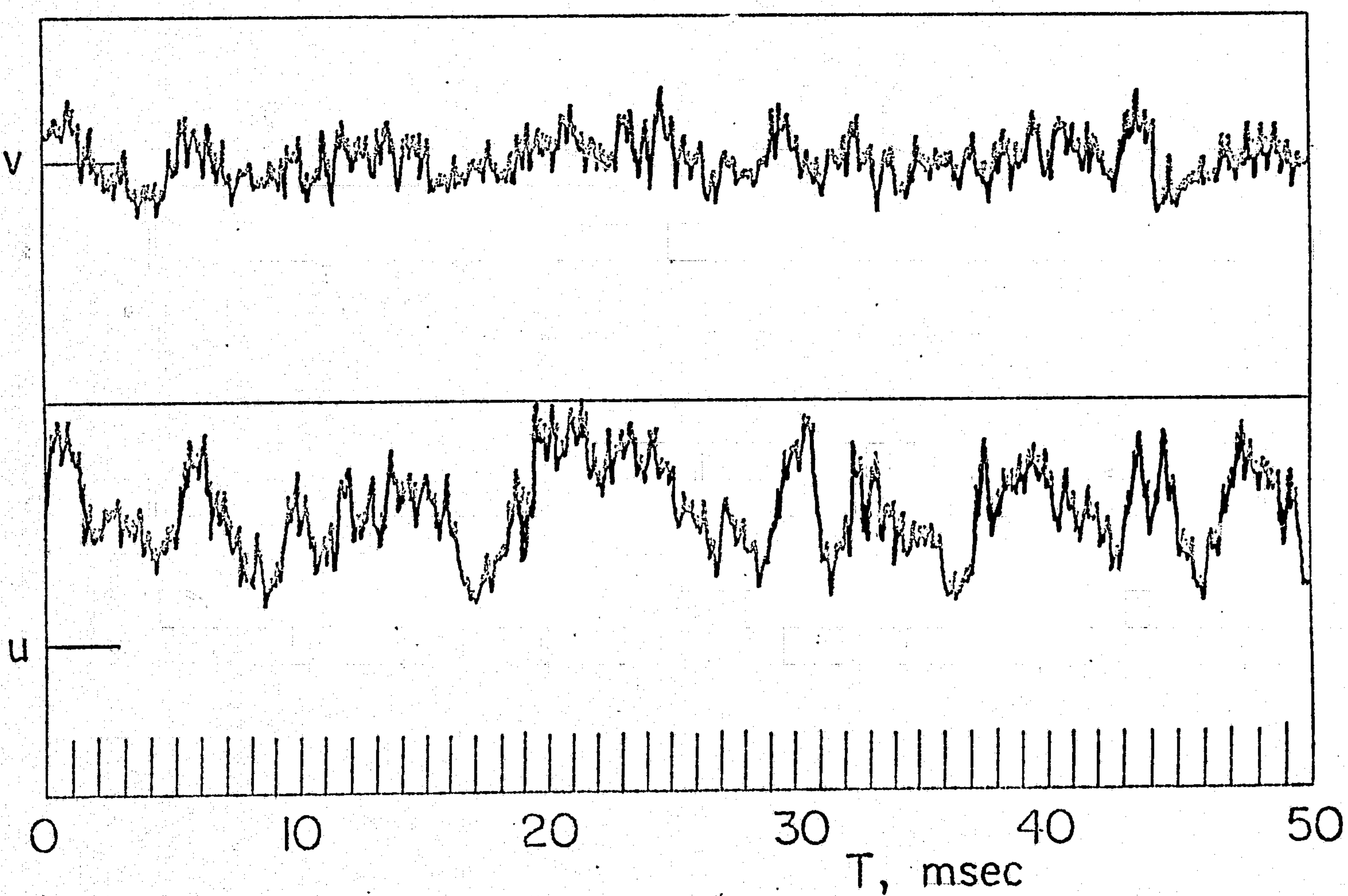

(b) x/D = 8.0, r/D = 0.5

Figure 37. Continued.

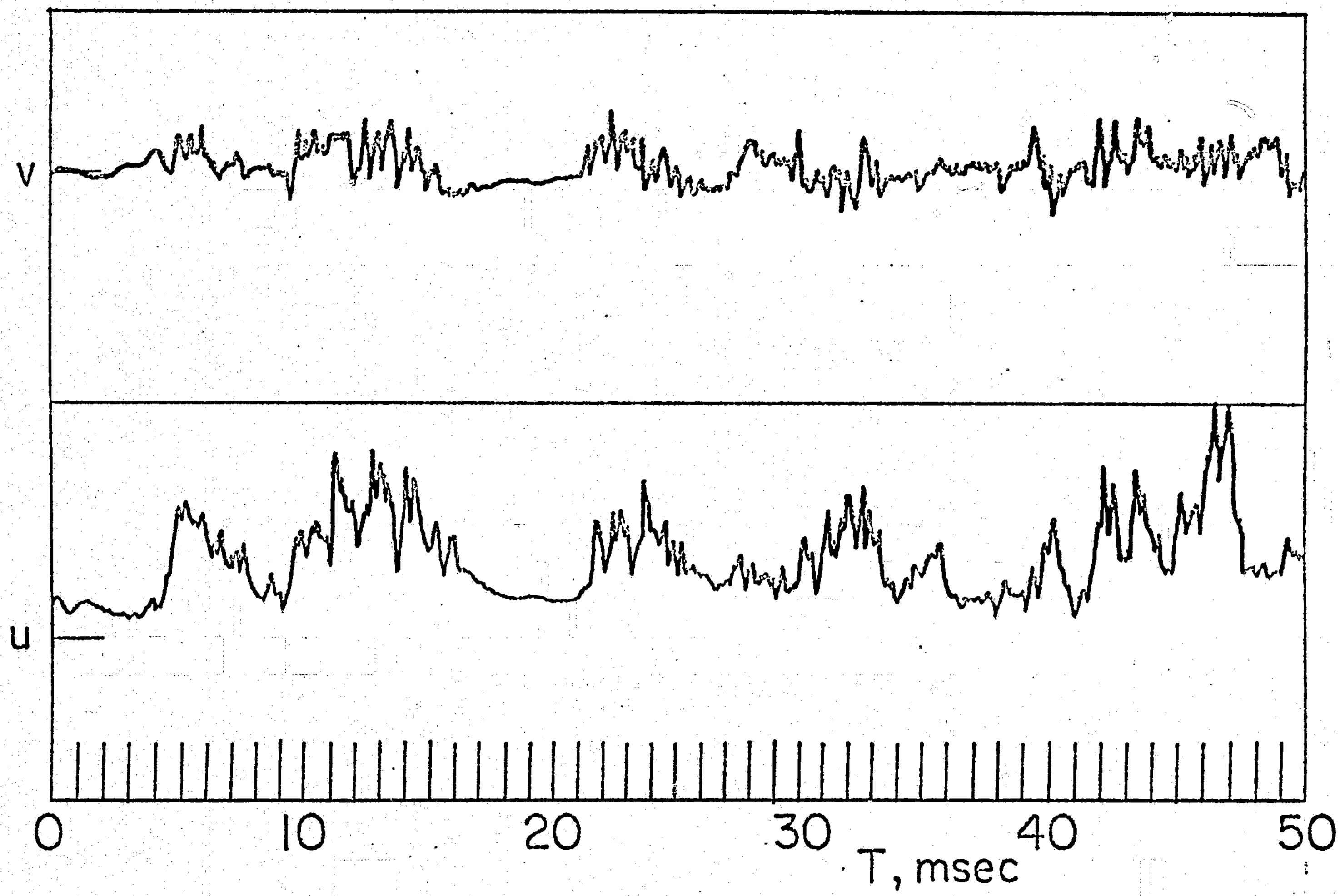

(c) x/D = 8.0, r/D = 1.0

Figure 37. Continued.

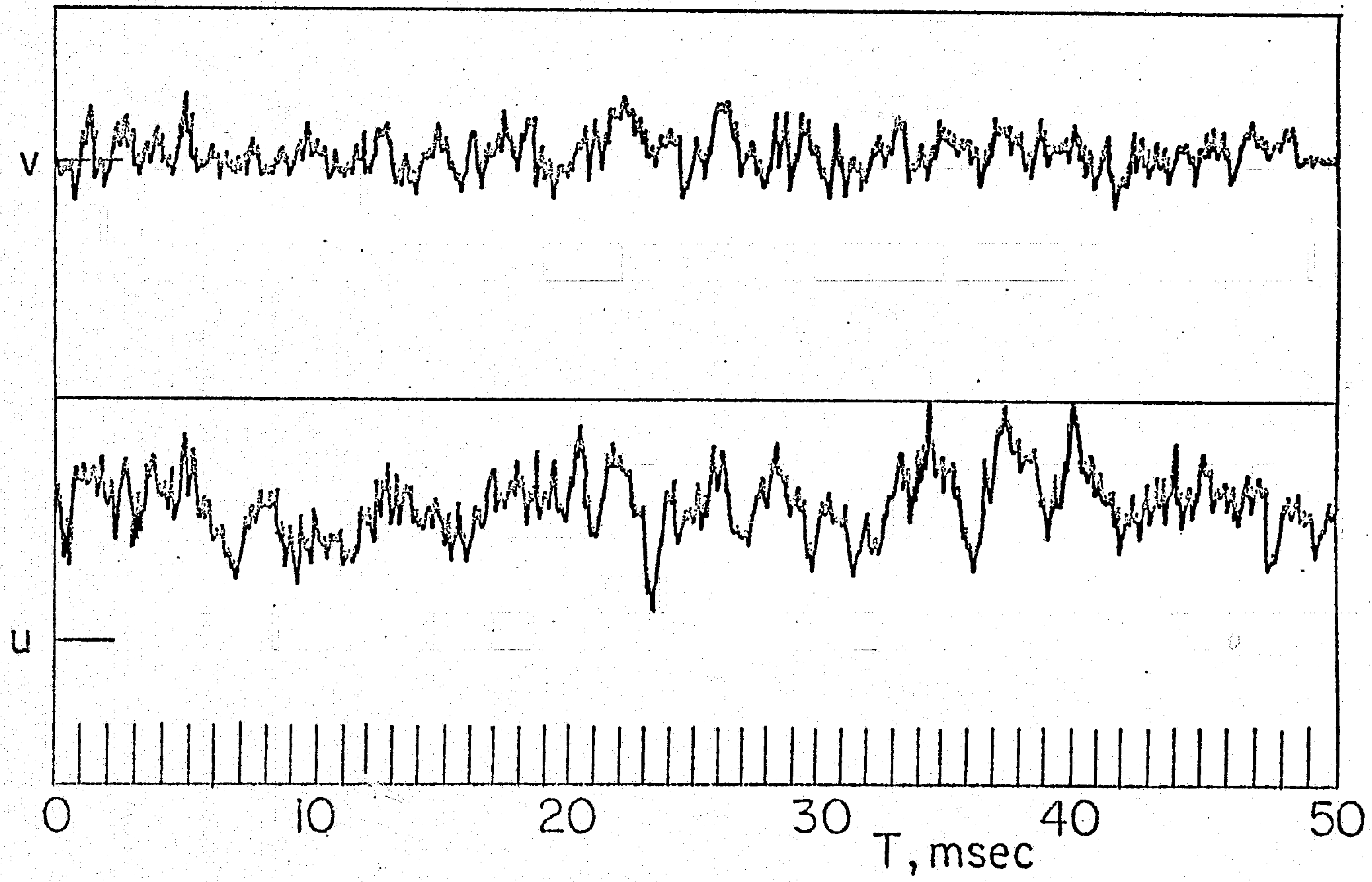

(d) x/D = 12.0, r/D = 0.5

Figure 37. Concluded.

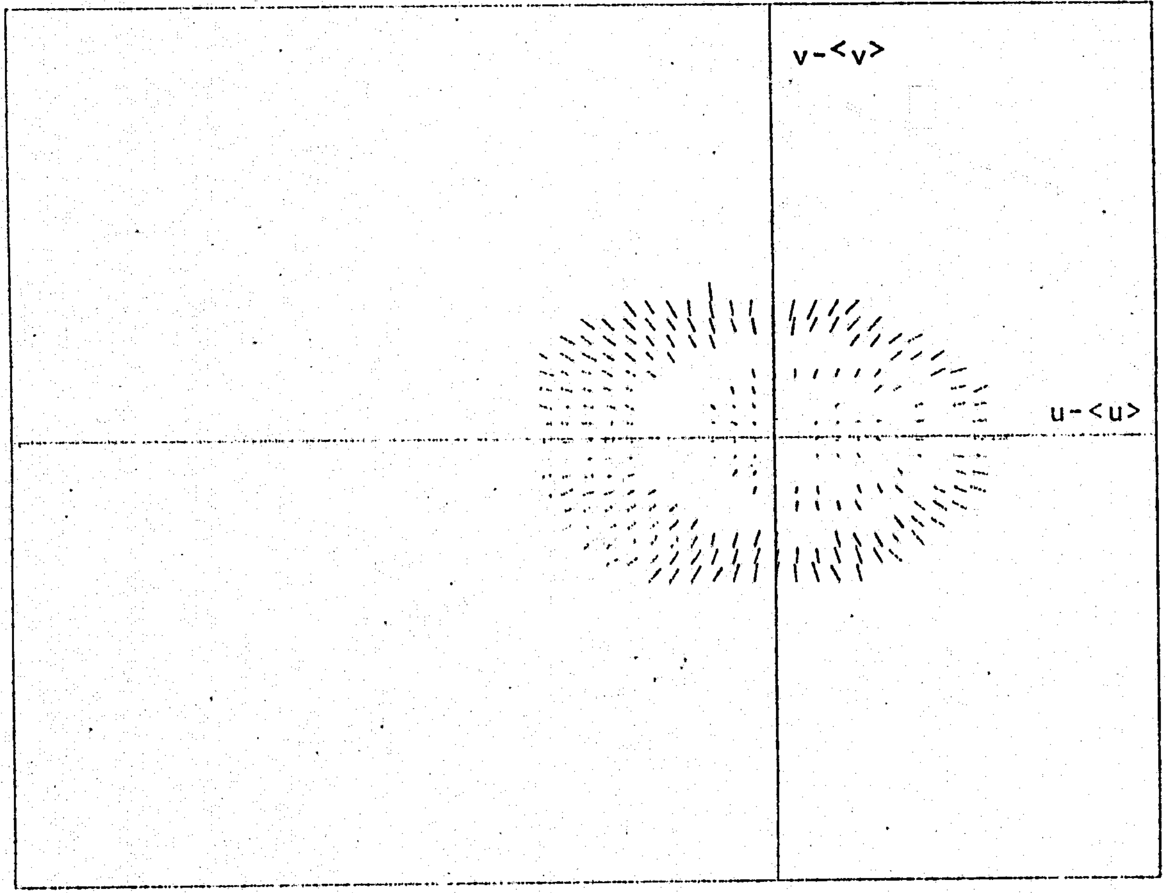

(a) x/D = 8.0, r/D = 0

Figure 38. Drift vectors: x/D = 8, 12

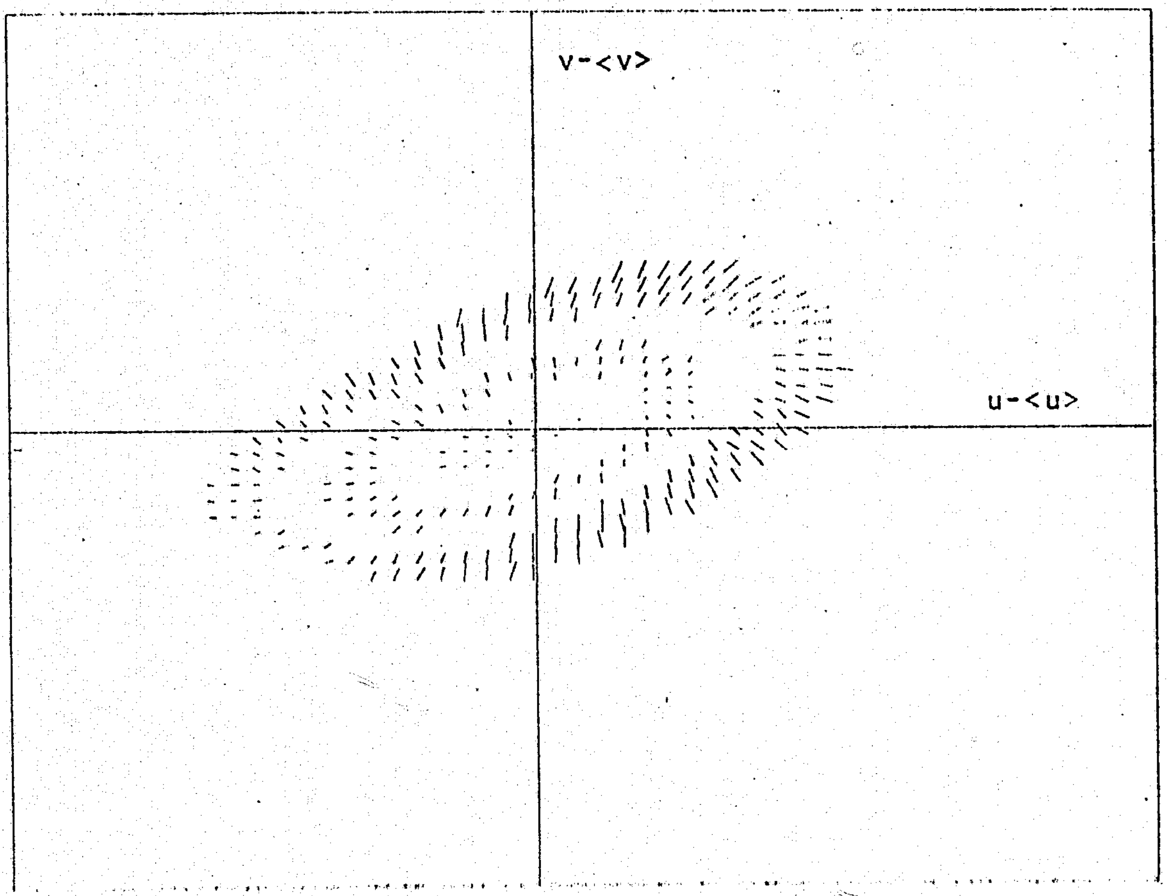

(b) x/D = 8.0, r/D = 0.5

Figure 38. Continued.

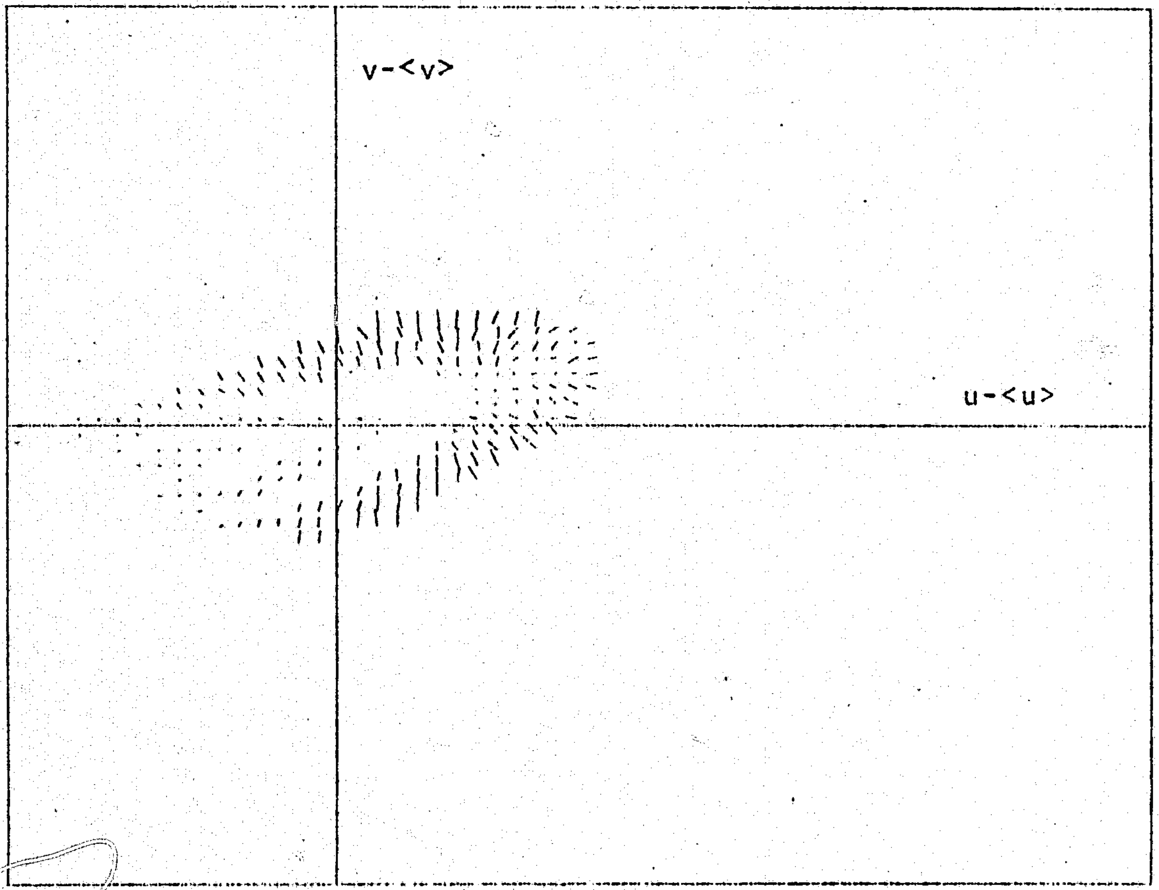

(c) x/D = 8.0, r/D = 1.0

Figure 38. Continued.

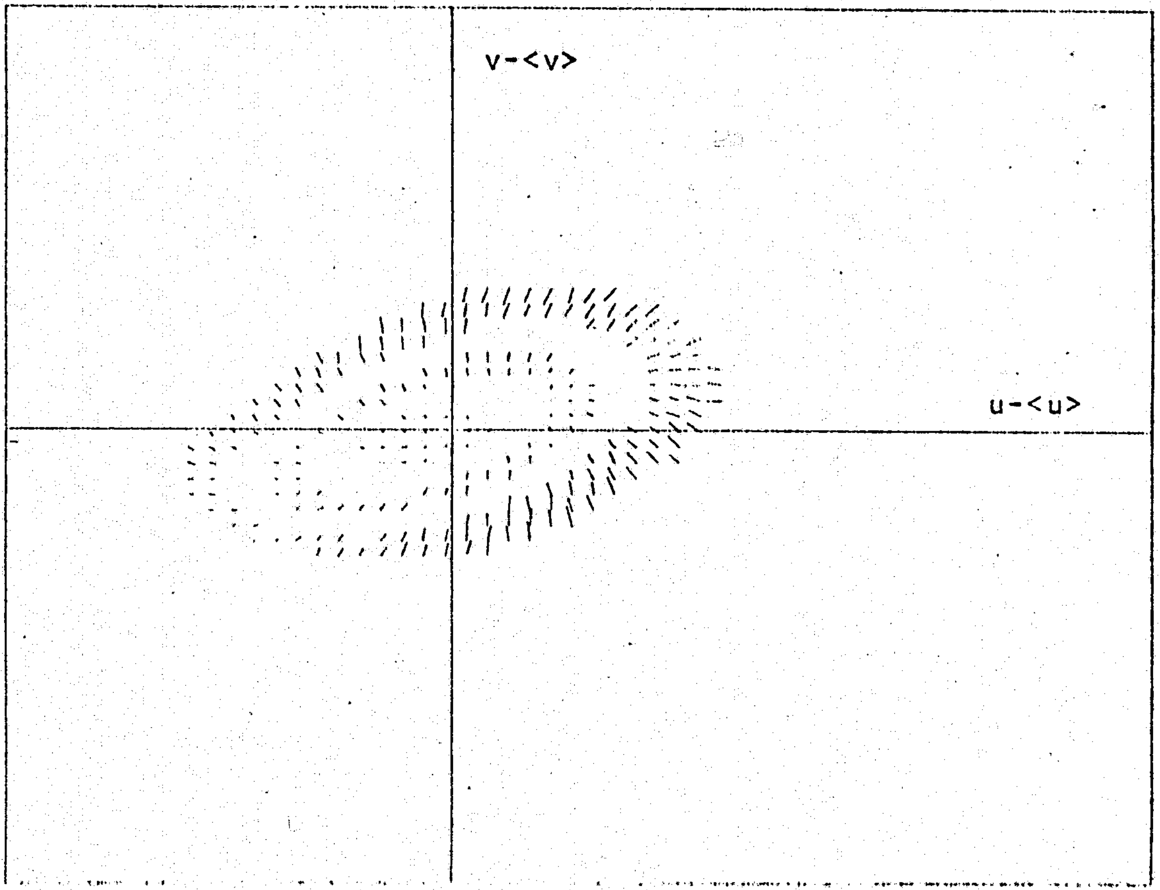

(d) x/D = 12.0, r/D = 0.5

Figure 38. Concluded.

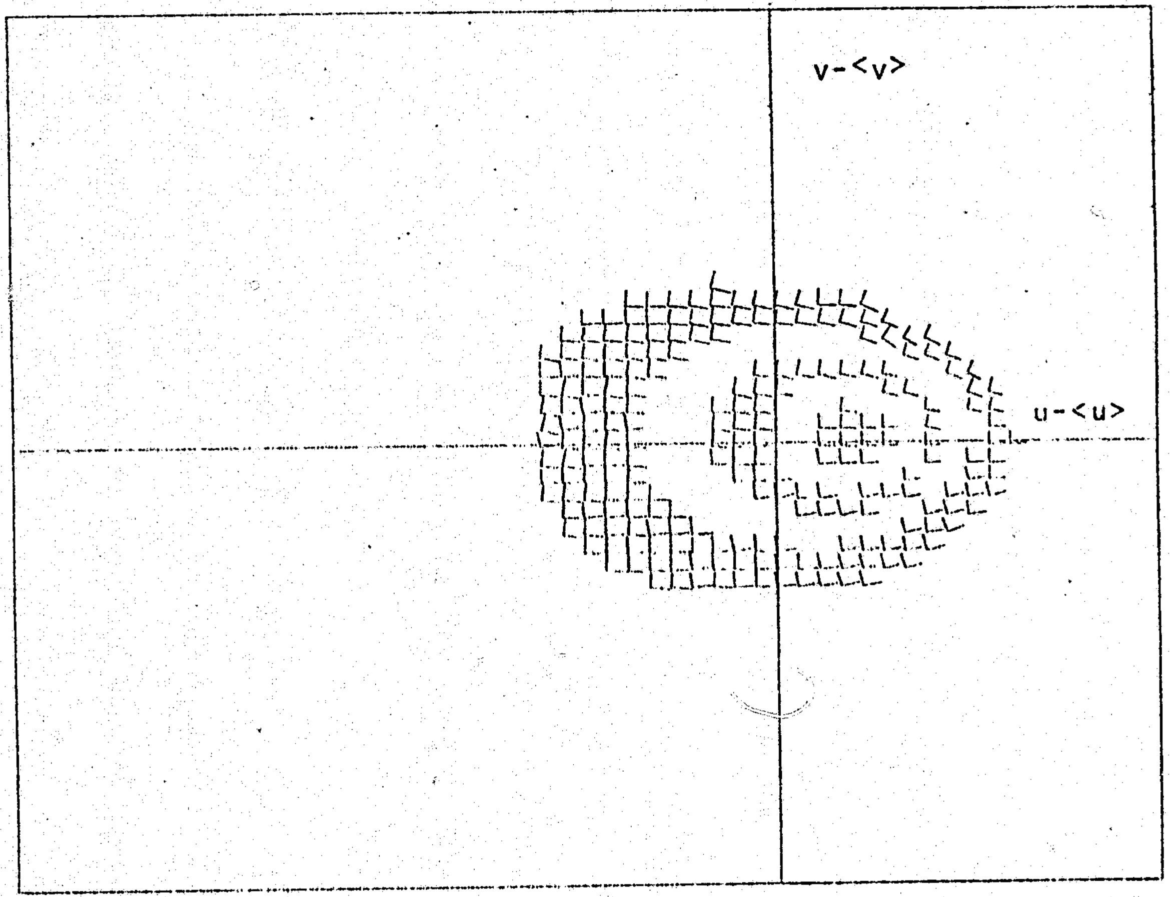

(a) x/D = 8.0, r/D = 0

Figure 39. Diffusion tensors: x/D = 8, 12.

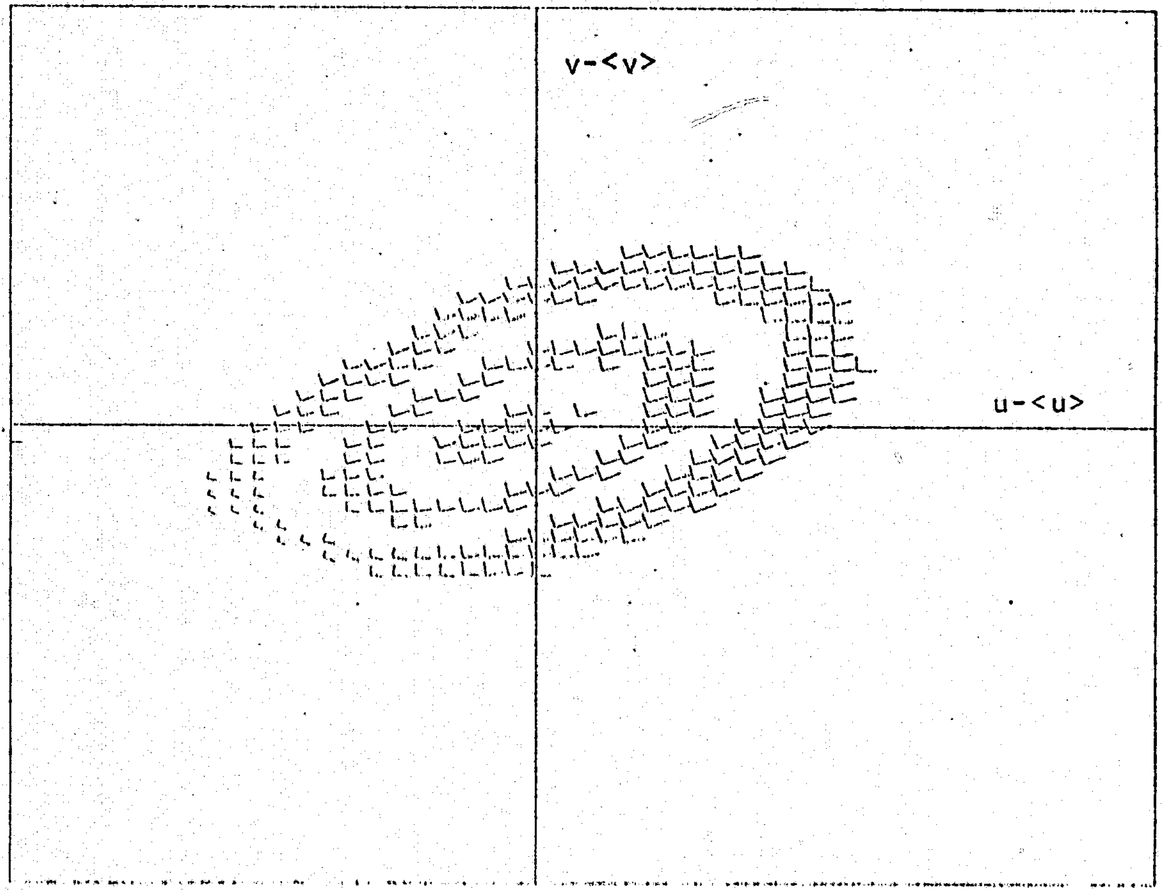

(b) x/D = 8.0, r/D = 0.5

Figure 39. Continued.

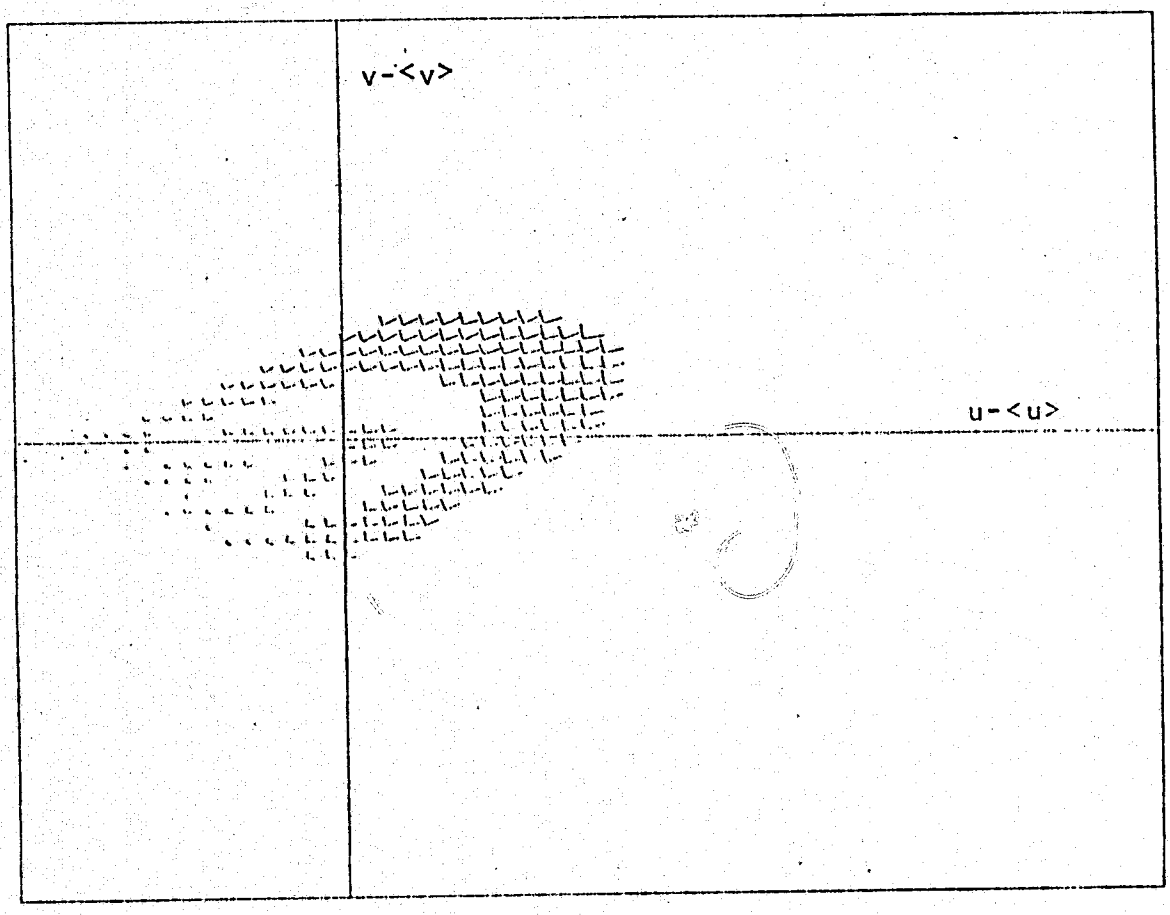

(c) x/D = 8.0, r/D = 1.0

Figure 39. Continued.

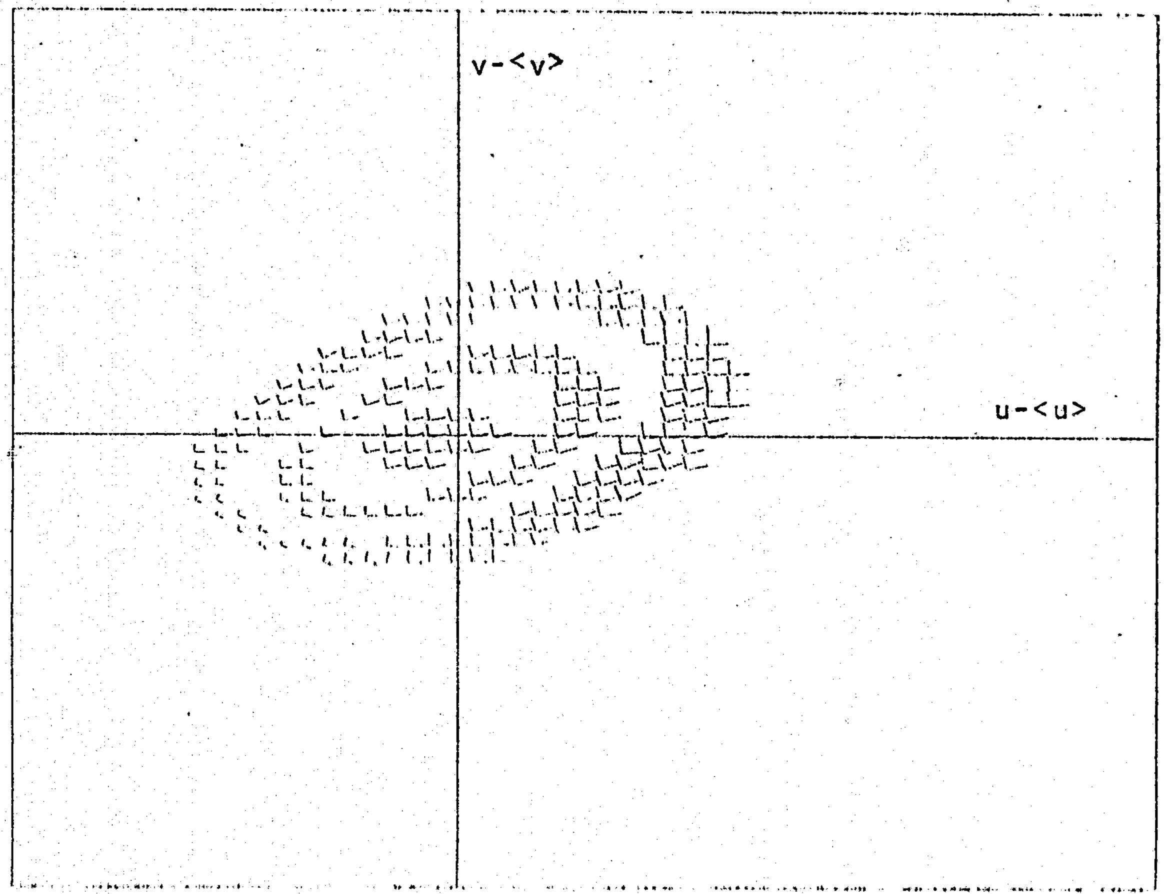

(d) x/D = 12.0, r/D = 0.5

Figure 39. Concluded.

some point in the transitional mixing region the velocity signal can be modelled statistically as a noise driven process.

6.5 Generation of complex correlation

The complex scalar correlation $<WW^*>(\tau)$ was defined and discussed in section 3.4. The correlation was then measured at position (x/D=.3, r/D=.5) according to the scheme described. The periodicity of the flow at that location is reflected in the measured correlation, figure 9. It is of interest to measure the correlation for locations farther downstream where the periodicity has disappeared. Accordingly, figure 40 shows the complex correlations for positions (x/D = 2,8; r/D = .5). These correlations behave quite differently from the earlier one. The imaginary part of the correlation is small, and the change in phase angle is no longer monotonic. This behavior in phase angle is difficult to interpret.

The drift vectors are forward differences and their orientations are measures of which direction the fluid was traveling in space during the time increment. Accordingly, counterclockwise solid body rotation in a spatial coordinate system being swept past the probe would appear as clockwise trajectories in the hodograph plane. Consequently the

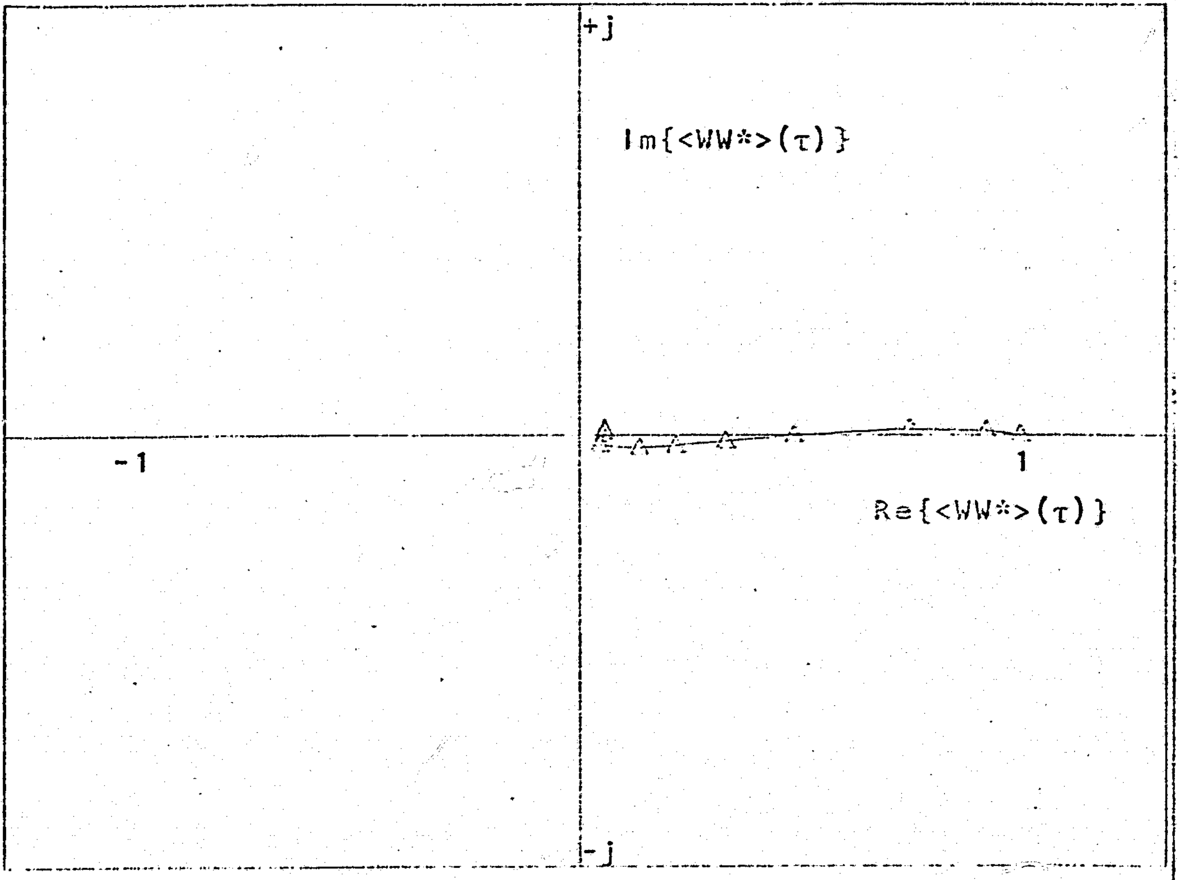

(a) x/D = 2.0, r/D = 0.5

Figure 40. Complex correlations: x/D = 2, 8

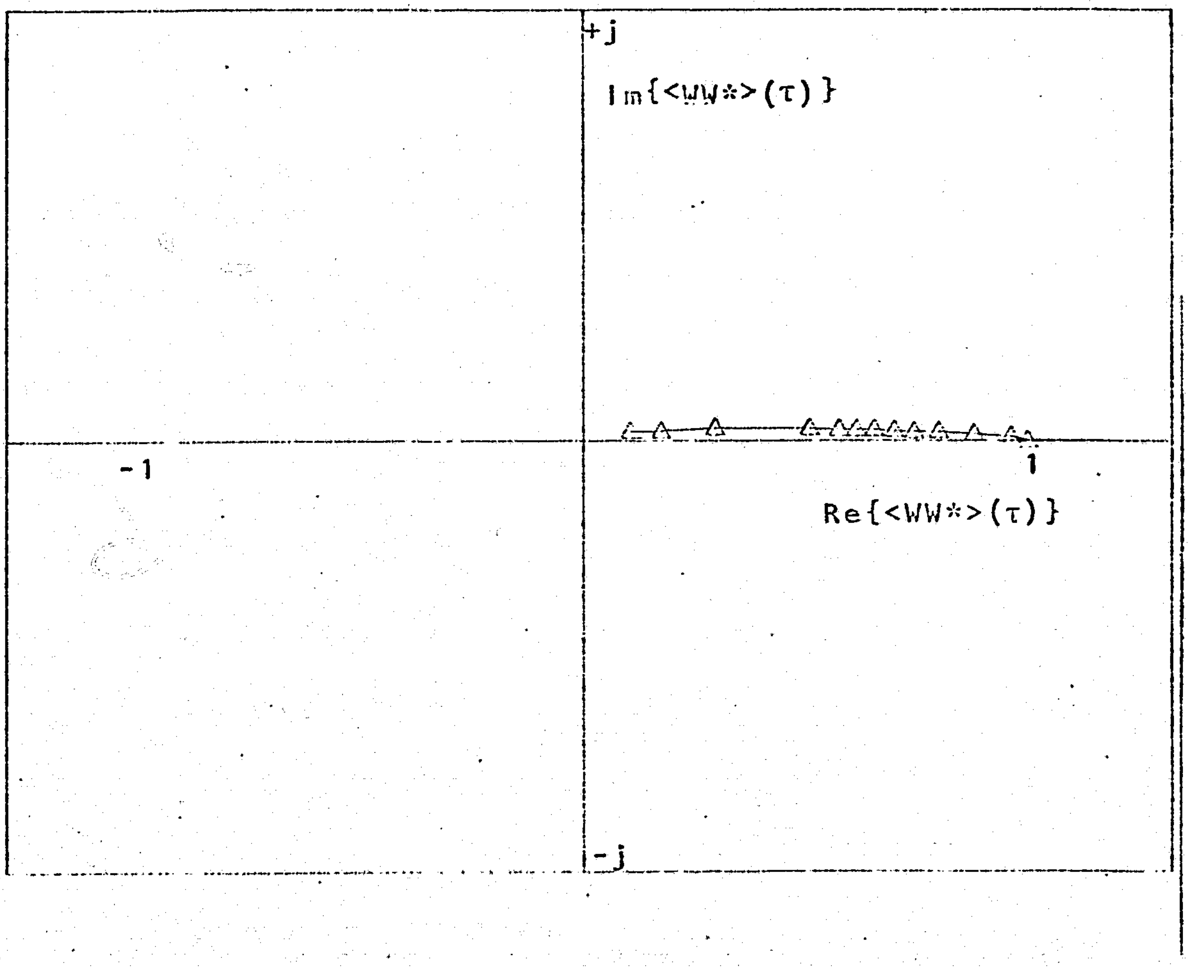

(b) x/D = 8.0, r/D = 0.5

Figure 40. Concluded.

direction of change of phase angle observed in figure 9 is consistent with the local shear. In figure 40, however, the phase angle changes in the opposite direction. Possibly the local fluid distortion is dominated by strong intermittent influences such as entrainment rather than by mean shear.

The decay of the correlation magnitude $S(\tau)$ at two and eight diameters is now clearly monotonic in time delay. The decay of $S(\tau)$ is presented in figure 41 as a function of τ normalized like an inverse Strouhal number. All three locations (x/D=.3,2,8; r/D=.5) are included and the display is essentially log log $S(\tau)$ vs $\log(\tau)$. Any exponential behavior of the decay will appear linear under that scaling. At the location (x/D=.3, r/D=.5) there are oscillations superimposed on the decay. However the data seems generally to fall off like $\exp(-\sqrt{\tau})$. At the other positions, however, the decay was very closely Gaussian for small , and generally approached something like a simple exponential at larger delays.

From the observed decay of $S(\tau)$ it is possible to define a correlation length scale. If τ_c is chosen as a characteristic time scale such that $S(\tau_c)/S(0) = 0.1$, then $\tau_c U_c/h$ is the convected correlation length scale normalized by the local shear layer thickness. This length scale appears in figure 42 for various downstream locations. For

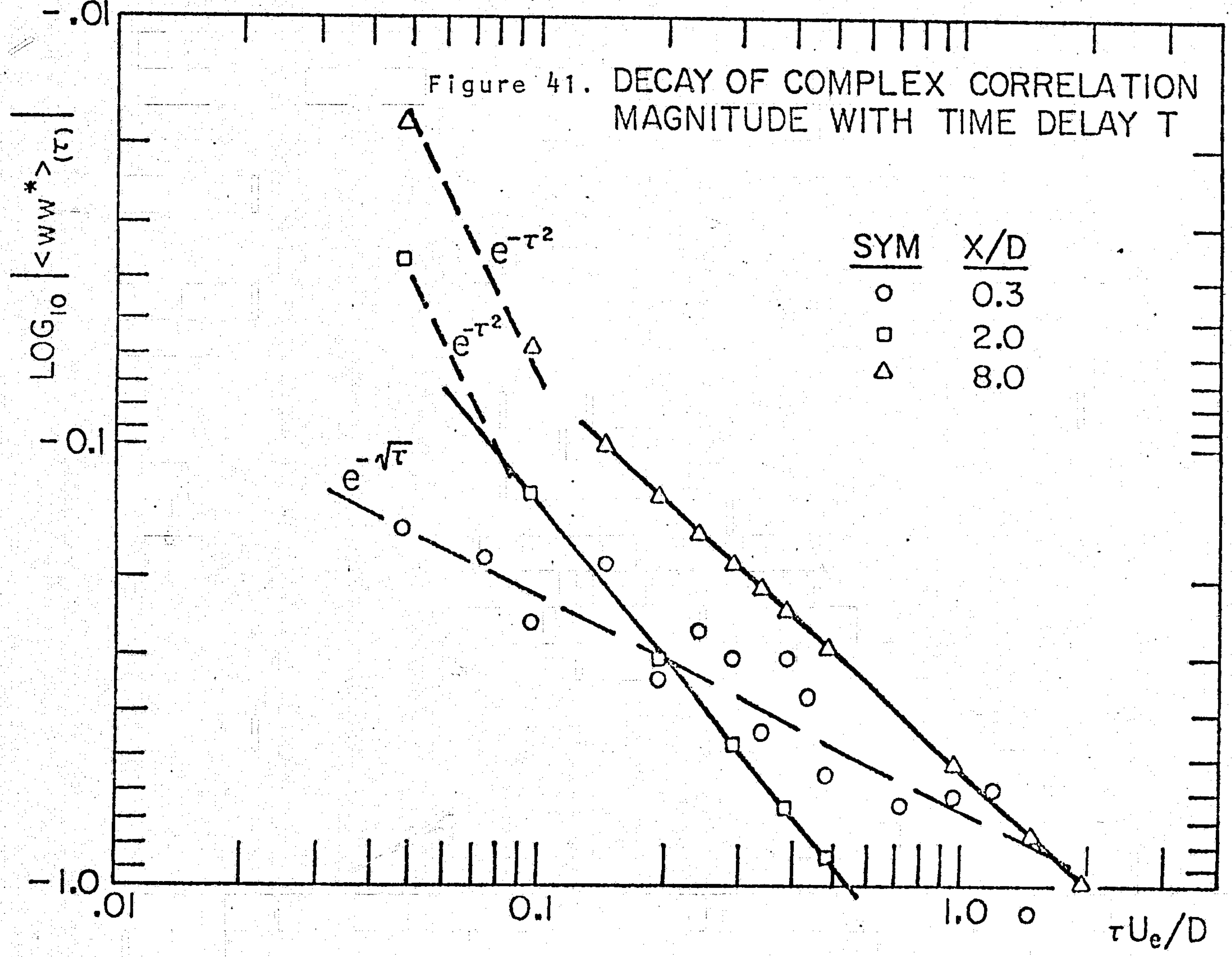

Figure 41. DECAY OF COMPLEX CORRELATION MAGNITUDE WITH TIME DELAY T

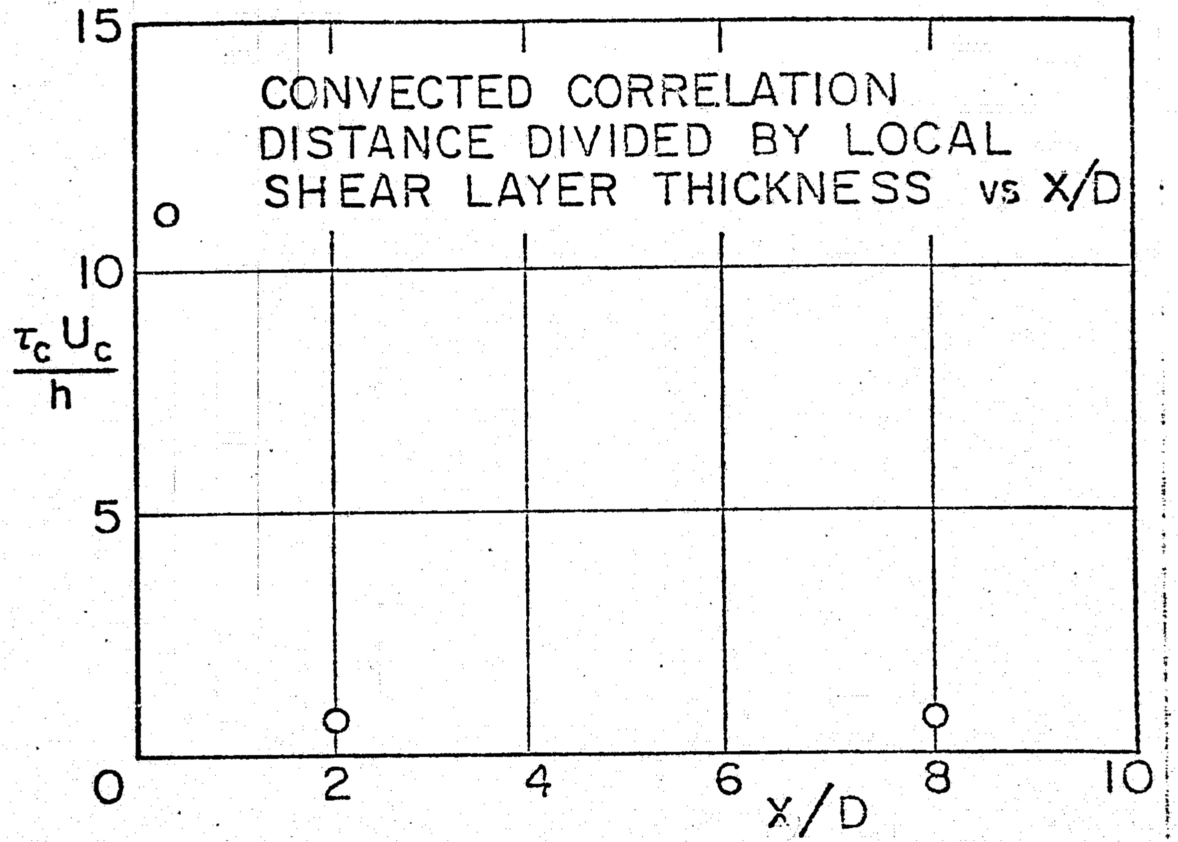

Figure 42. Correlation length scale $\tau_c U_c/h$ vs. x/D

the position (x/D=8, r/D=.5) the local jet radius was chosen as the shear layer thickness. The correlation length scale decreases from about 11 shear layer thicknesses at (x/D=.3, r/D=.5) to about 0.7 shear layer thicknesses at subsequent axial positions.

It is an interesting question whether there is enough information in the drift field measured over one time step τ_o to estimate the drift field and hence the complex correlation $<WW^*>(\tau)$ for arbitrary time delay $\tau=n\tau_o$. Whatever scheme is selected, there are constraints on the drift field as well as on the correlation itself that serve as checks on the reliability of the estimate:

1) as the time step τ is increased the drift vectors must increasingly point towards the mean $\{<u>,<v>\}$,

2) since the statistics are stationary, the integral $\iint <d\underline{q}>(u,v)\ P(u,v)\ dudv$ must add up to zero,

3) from physical arguments the magnitude $S(\tau)$ must generally decrease.

The simplest scheme that comes to mind is to associate a direction and magnitude with each cell (u,v) in the hodograph plane based on the measured drifts, to note in which cell the tip of each $<d\underline{q}>$ vector falls, and to then add the corresponding magnitude and direction. According to this scheme of course the time delays are restricted to integer multiples of the original sampling rate. The vector arithmetic is shown schematically in figure 43. The resulting estimate of the complex correlation is shown in figure 44 for the position (x/D=8, r/D=.5). The correct, measured correlation appears in figure 40b. Comparison between the two indicates that the scheme doesn't provide a good estimate. Unless a more elaborate estimation technique would provide more accurate results, the most efficient method of measuring complex correlations is to use a Fast Fourier Transform algorithm and measure the individual elements of the two-dimensional correlation matrix R_{mn}.

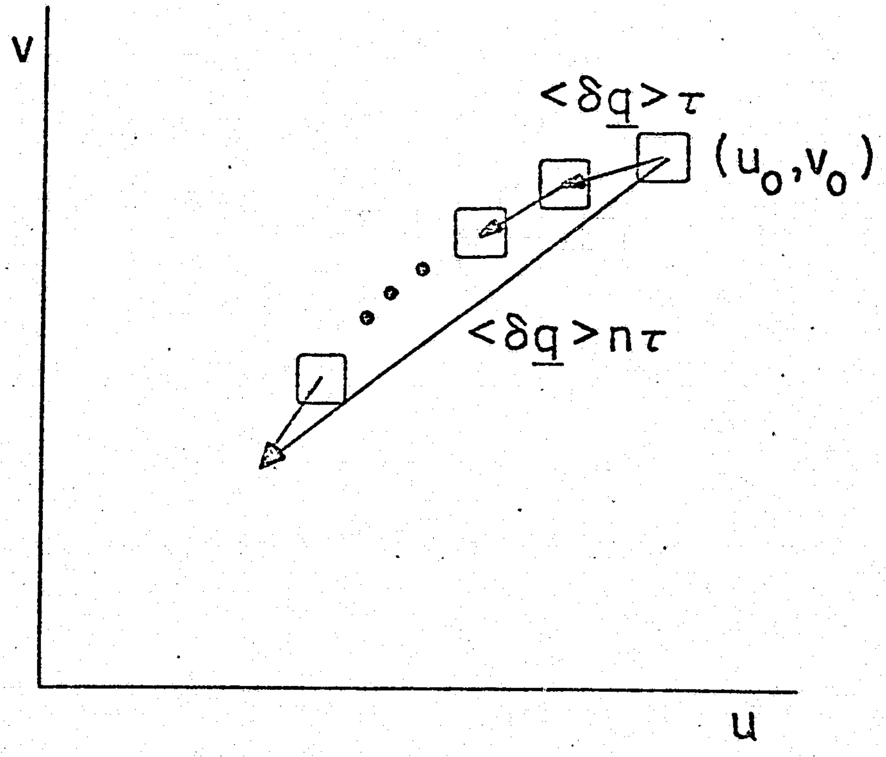

Figure 43. Synthesis of forward differences for arbitrary time step $\tau = n\tau_o$: schematic.

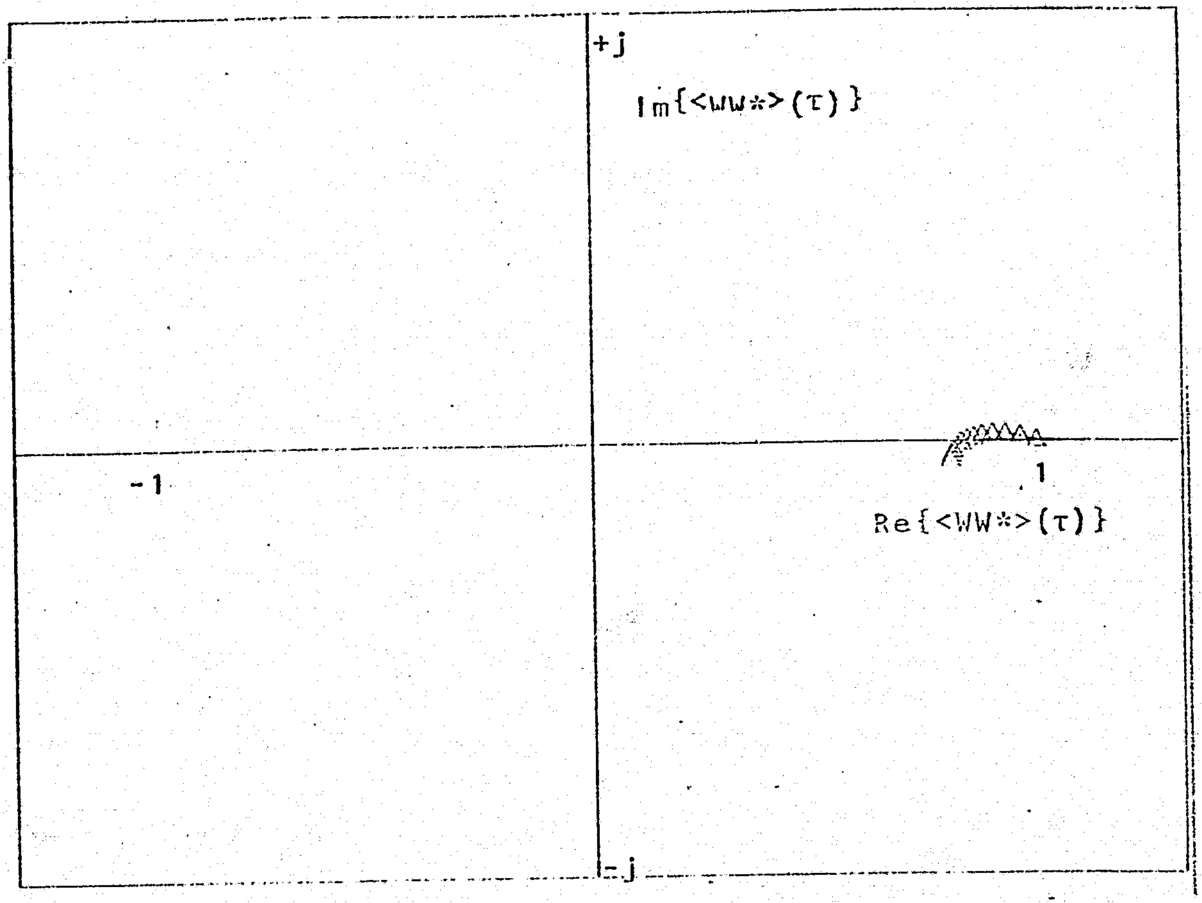

Figure 44. Estimated complex correlation:
$x/D = 8.0$, $r/D = 0.5$

7. EVIDENCE FOR PAIRING HYPOTHESIS

7.1 Conceptual basis

The role that vortex pairing plays in the growth of a turbulent shear layer has been demonstrated by Winant and Browand (1974). Vortex pairing is considered to play a similar function in a turbulent circular jet. However the mechanism is complicated by the fact that unlike the free shear layer the jet has two length scales: the exit diameter as well as the local shear layer thickness. Certainly in the early stages of growth the jet shear layer is similar to a free shear layer. In fact since a cylindrical vortex sheet lacks a most amplified mode of instability, the laminar instability is probably two-dimensional. Analogous to a two dimensional shear layer, the jet instability rolls up into lumps of concentrated vorticity which coalesce into rings of vorticity which interact to cause the initial mixing layer spreading. This much is evident from the flow visualization studies (e.g. Browand, Chu, and Laufer, 1975) at least for low and moderate Reynolds numbers. The nature of the interaction between turbulent vortex rings is suggested by the kinematics of vortex rings idealized from potential flow theory and is indicated diagrammatically in figure 45. Consider the case of a ring where all of the

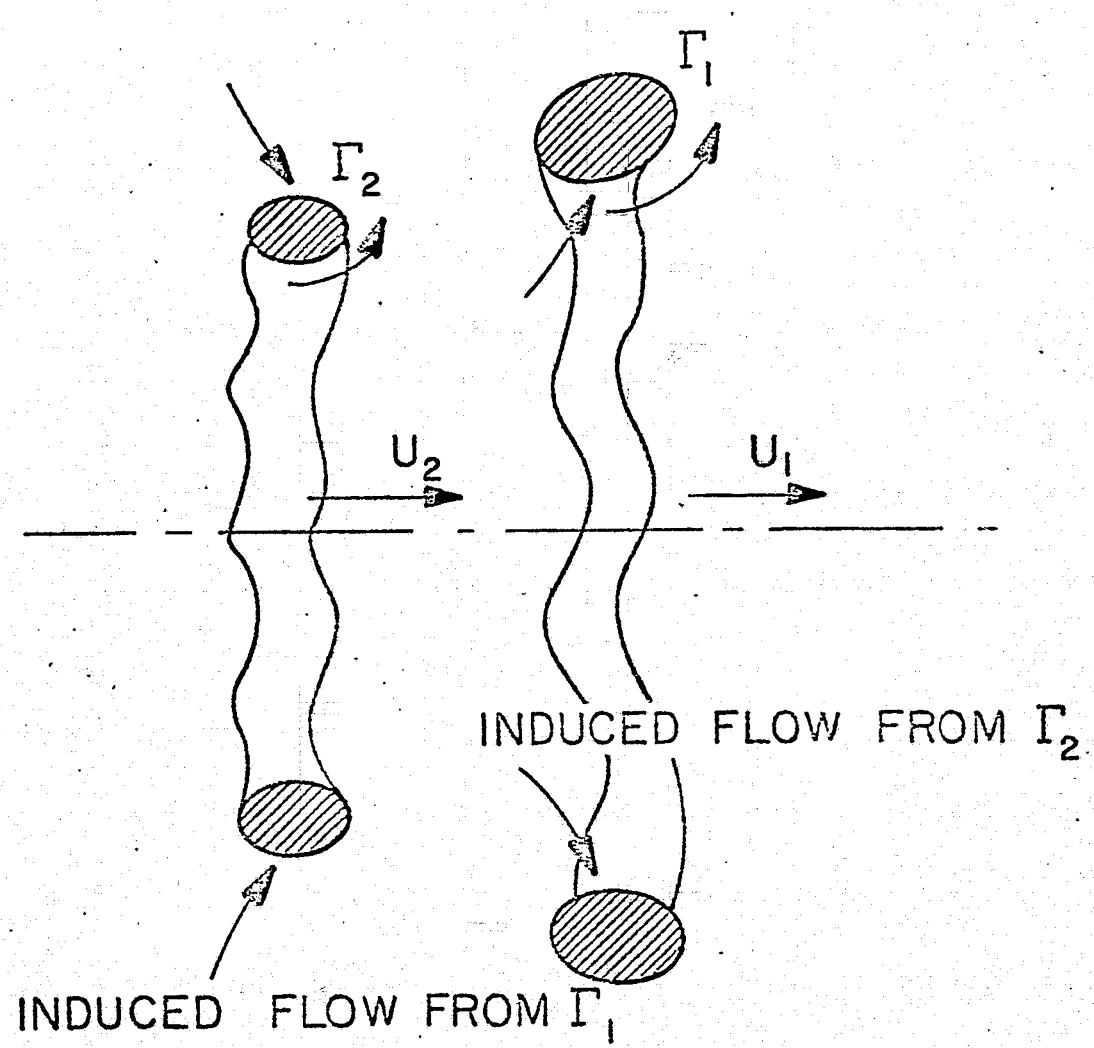

Figure 45. Vortex ring pairing: conceptual.

vorticity is confined to an annular core of radius a which is small in comparison with the ring radius R. Then the speed of the ring U_c depends only on R and the circulation Γ (Batchelor, 1967):

$$U_c = \frac{\Gamma}{4\pi R}\ln(R/a) \qquad (21)$$

Note that for constant circulation the ring moves faster as the radius becomes smaller. Now consider two rings one behind the other: the induced flow from the forward ring is radially inwards tending to compress the rear ring, causing it to accelerate, while the flow induced by the rear ring causes the forward ring to spread out and decelerate. The rear ring will overtake and pass through the forward ring. According to potential flow theory this "threading" process would repeat itself indefinitely. In practice the cores of the rings are observed to coalesce producing a single ring with twice the circulation. Unlike the free shear layer there are two scales involved in ring pairing: the ring diameter (i.e. jet diameter) and the core diameter (i.e. shear layer thickness). It is an open question whether pairing continues when the core has grown to a large fraction of the jet radius. The flow visualization studies do not help here because there is so much mixing that the dye or hydrogen bubbles are obscured.

In the sections to follow, eduction experiments are described that are designed to detect pairing, and to detect its signature in the near field. It is an easy matter to detect the roll up of the laminar instability and the occurrence of the first pairing. It is more difficult to detect subsequent pairings, although our attempts are described. Finally time averaged near field measurements are interpreted according to the pairing hypothesis to model the mean location and variance of the pairings.

7.2 Correlation measurements inside shear layer

The laminar shear layer instability is sufficiently amplified at about $x/D = 0.2$ that it can be easily detected with a hot wire probe. The probe was placed into the shear layer at the radial position corresponding to maximum turbulence level and autocorrelations of the signal over a range of downstream positions are shown in figure 46. For axial stations less that 0.4 diameters the autocorrelations appear like damped oscillations with constant frequency. Normalized by the initial shear layer thickness of .05 diameters (from figure 12), and velocity $U = U_e/2$, this frequency corresponds to a Strouhal number of 0.2. Two-dimensional linear stability theory (e.g. Lessen, 1949) predicts the Strouhal number of the preferentially amplified mode to be between .2 and .3. So the data is so far

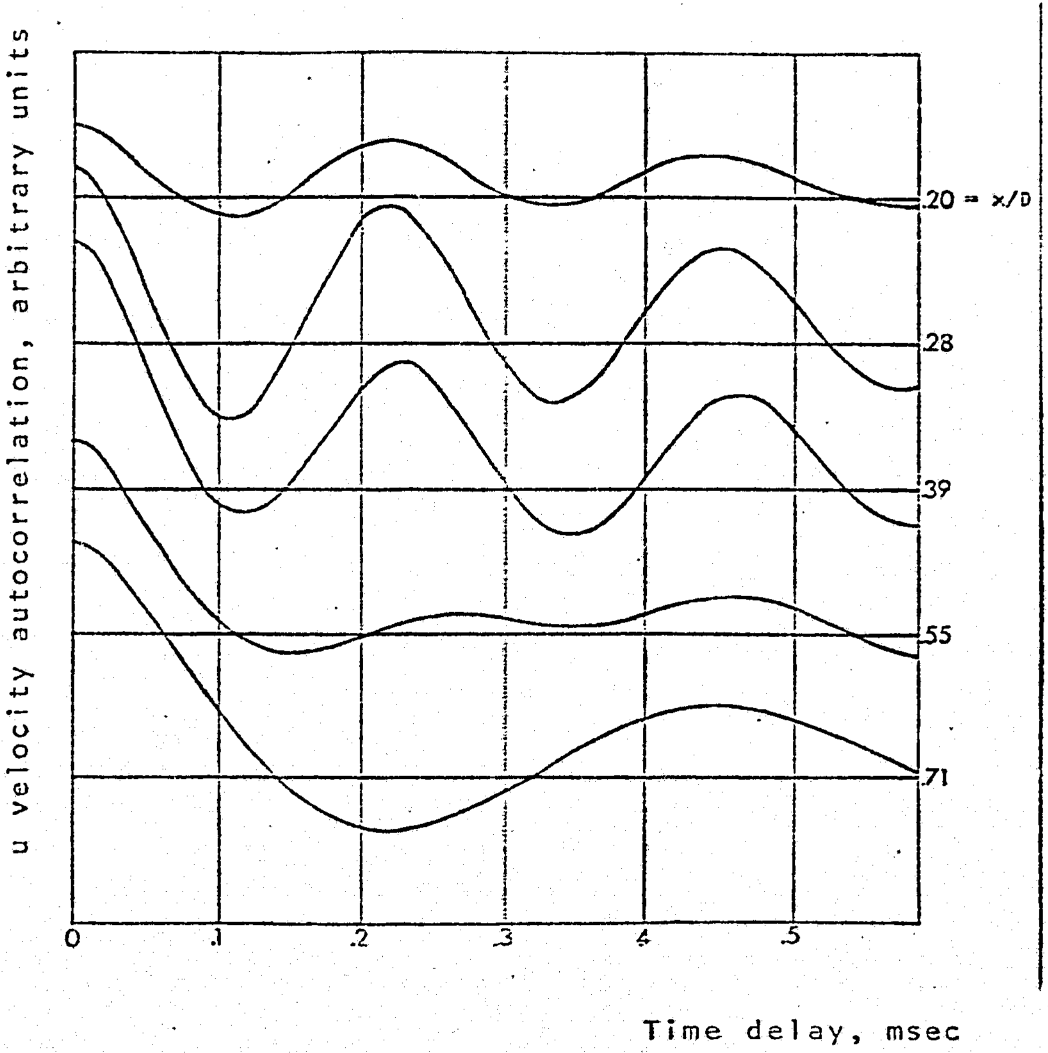

Figure 46. Turbulence autocorrelations inside mixing layer. (r/D ≃ .5)

consistent with the model.

There is sufficient temporal coherence at these early upstream positions that there is evidence of the first pairing in the autocorrelations. Between stations x/D=.4 and x/D=.7 every other wave in the autocorrelations disappears. This amounts to a discrete shift in frequency to the exact subharmonic of the eigenmode. The implication is that there is a discontinuous doubling in length scale somewhere between x/D=.4 and x/D=.7. This is certainly consistent with vortex pairing. Beyond x/D = .7 the autocorrelations exhibit a continuous increase in the time scale associated with the periodicity. As it turns out there is at least one more pairing that can be distinguished using conditional sampling. The continuous shift in frequency observed in the autocorrelations is the result of the statistical variation of the location of the subsequent pairing (or pairings).

7.3 Two point eduction techniques

In order to derive some spatial information about the first and subsequent pairings, simple two point eductions were performed across the shear layer at various axial locations as far downstream as x/D=9. Two constant temperature single wire probes were used: the triggering probe was placed in the core next to the shear layer and the probe whose signal was being educted was placed in the shear layer at the same axial station as the triggering probe but at varying radial positions. A pulse was generated whenever the trigger probe signal exhibited a positive slope and a level above the mean greater than one r.m.s. of the fluctuation. This condition is a standard first attempt in conditional sampling of turbulent shear flows (e.g. Willmarth and Lu, 1972).

The educted waveforms appear in figure 47. Each subfigure corresponds to a particular downstream station, and in each case the indicated radial positions are relative, with positive r pointing in the direction of the entrainment region. Closest to the nozzle (x/D=.20, figure 47a) there is an abrupt 180° phase shift in the center of the shear layer accompanied by small fluctuation amplitudes. This behavior is suggestive of a simple vortex sheet. Another 0.1 diameters downstream, however, the behavior has changed. The phase shift is spread out over 15% of the shear layer thickness, and in the center there are twice as many crests (figure 47b). The corresponding harmonic frequency is absent in the power spectra (e.g. figure 46), which indicates that instead of a frequency doubling there is a double valued phase relationship between the trigger condition and the educted waveform at this radial location.

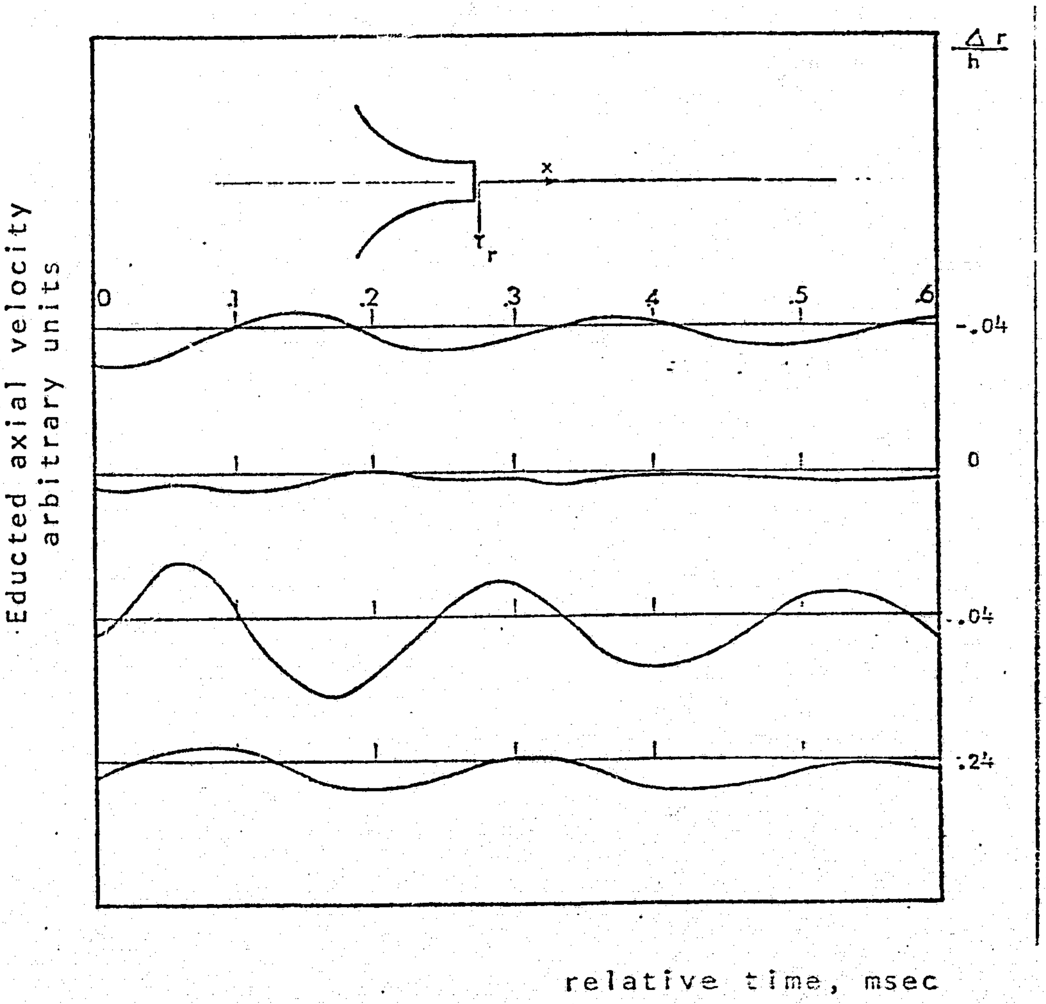

(a) x/D = .20, Δr/h = -.04 to .24

Figure 47. Educted velocity signatures across mixing layer.

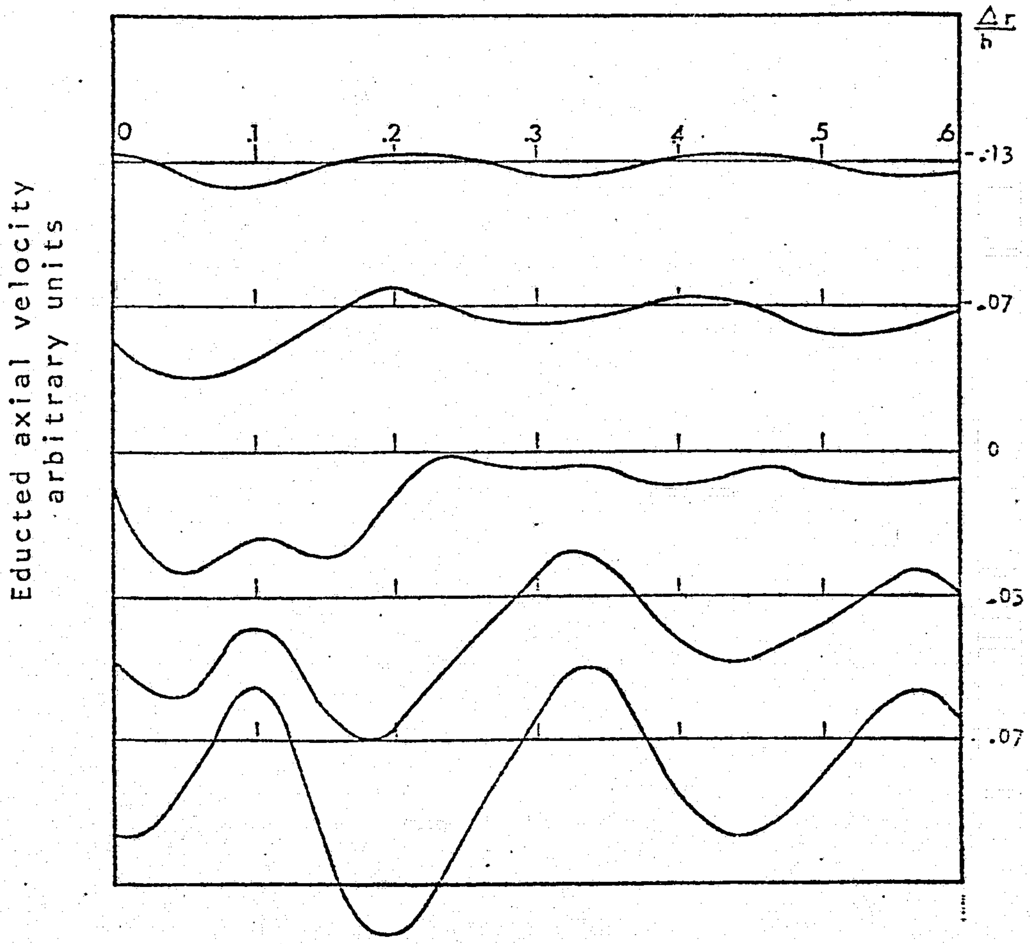

(b) x/D = .28, Δr/h = -.13 to .07

Figure 47. Continued.

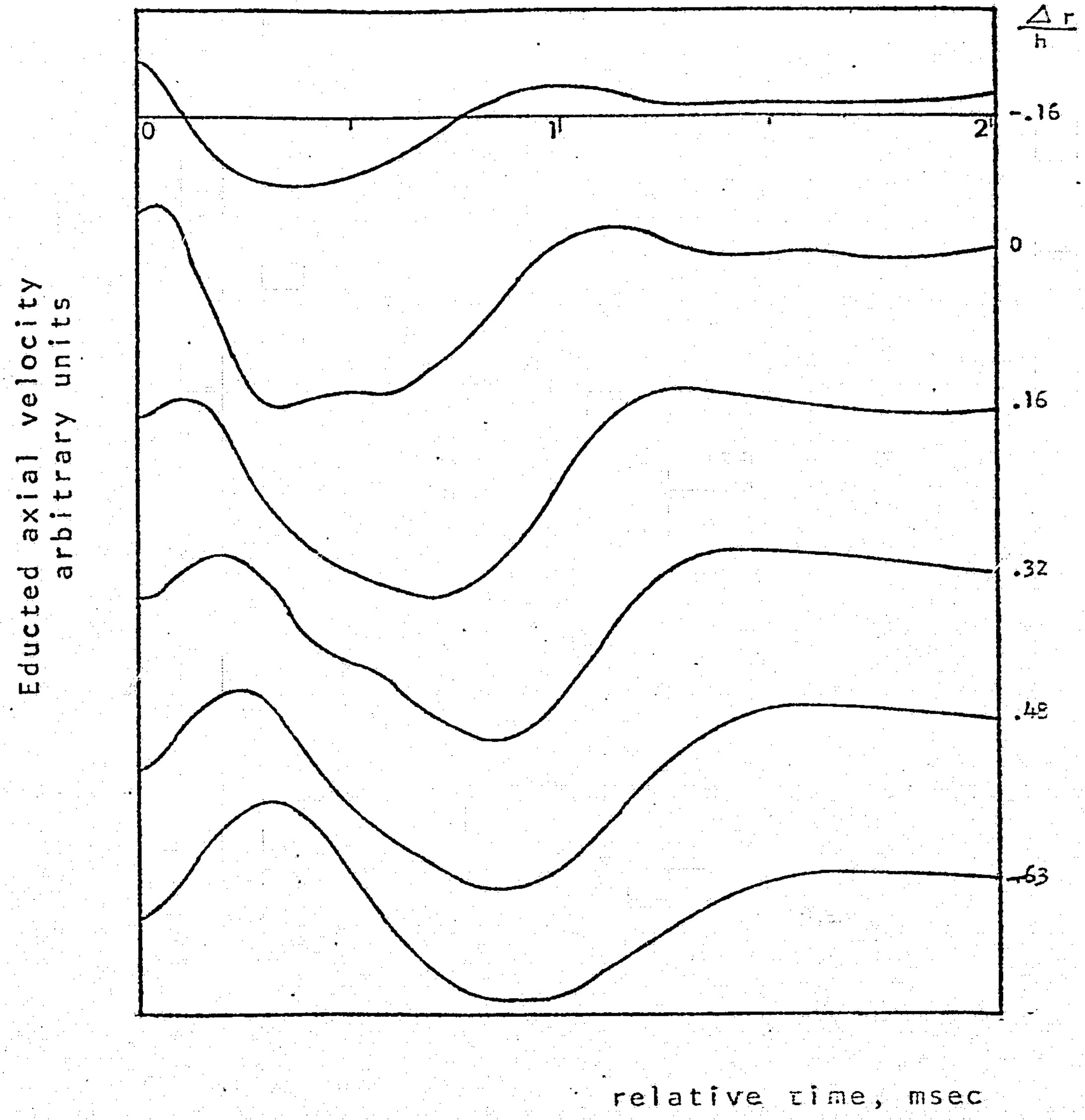

(c) x/D = 0.9, Δr/h = -.16 to .63

Figure 47. Continued.

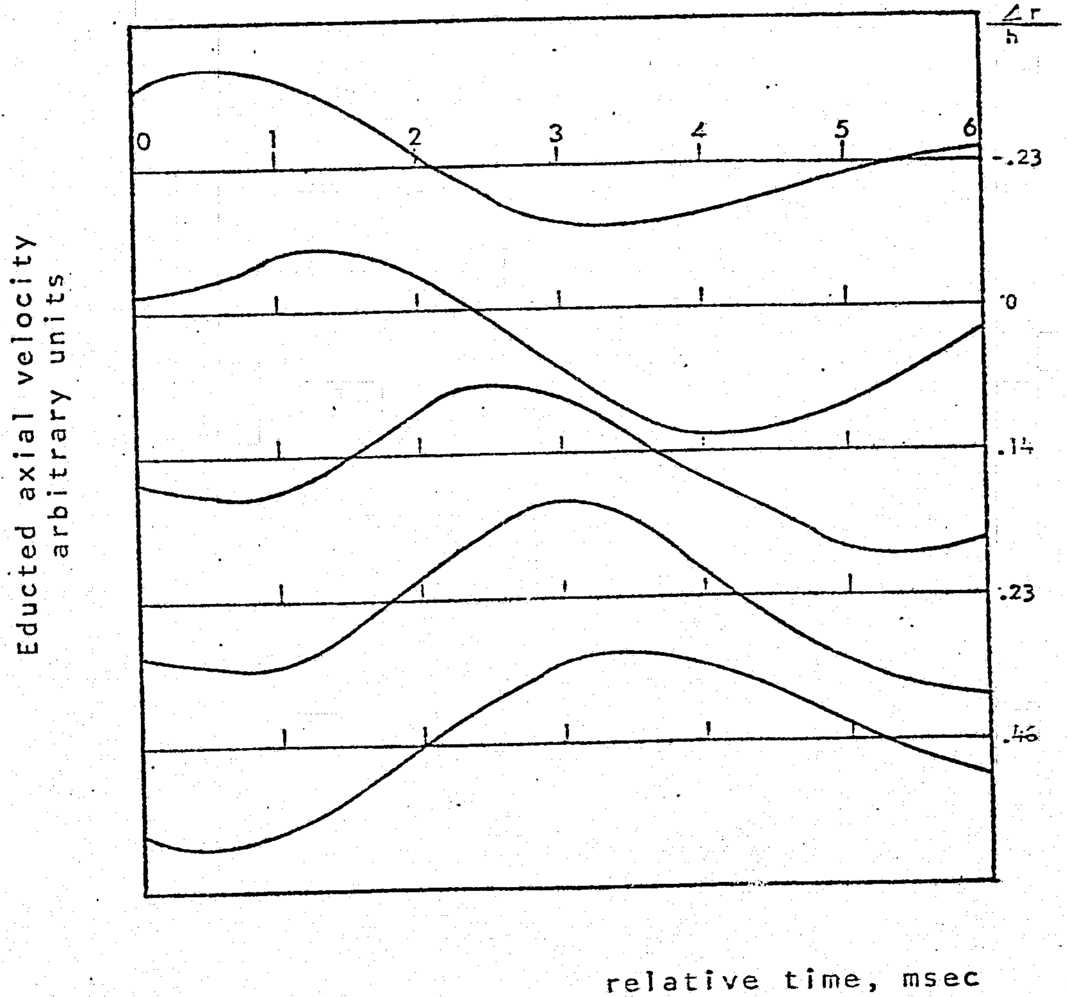

(d) x/D = 4.0, Δr/h = -.23 to .46

Figure 47. Continued.

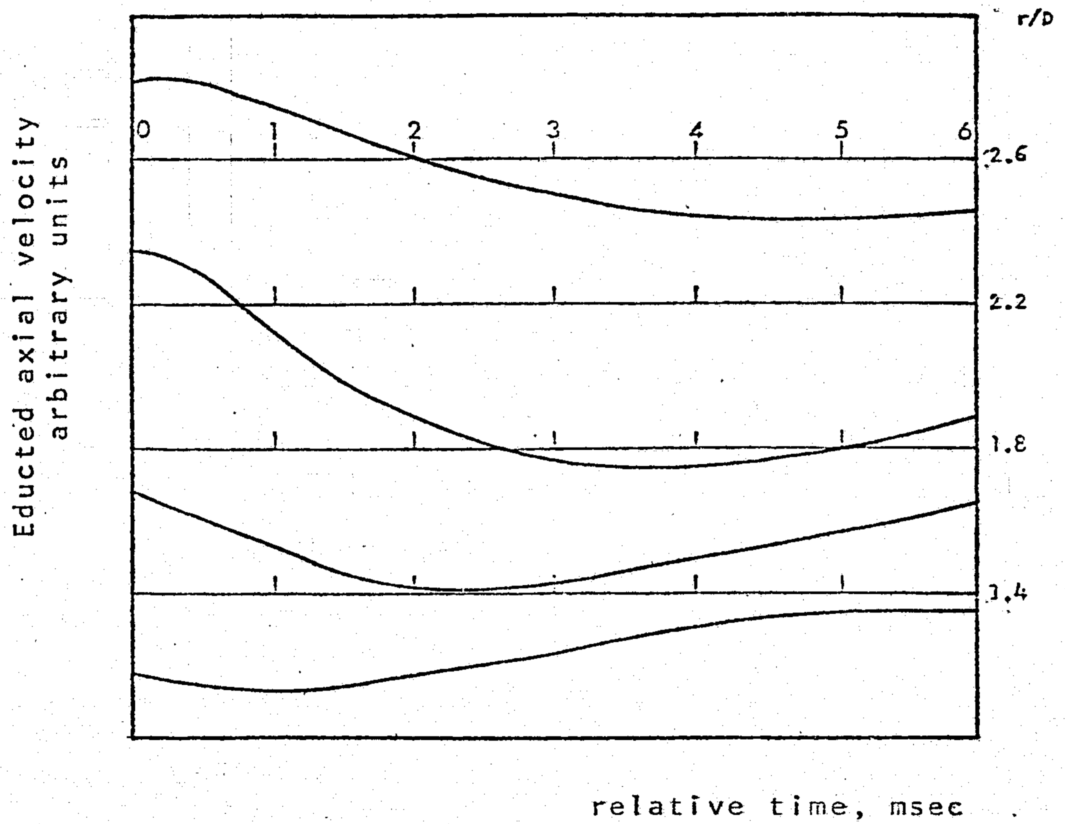

(e) x/D = 9.0, r/D = 1.4 to 2.6

Figure 47. Concluded.

This double valued phase relationship is observed in the eduction measurements of Winant and Browand (1974) in the free shear layer and is caused by the pairings. The double structure is barely discernable at x/D=.9 (figure 47c) where the associated time scale is the second subharmonic of the eigenmode. The double structure here probably corresponds to a third pairing. At farther downstream positions, x/D = 4 and 9 which are positions of interest acoustically, it is unclear whether the waveforms represent a phase shift across a coherent structure or an increasing phase delay due to the variation of mean velocity across the layer.

A more sophisticated trigger condition must be developed before pairings can be detected farther downstream than about a diameter. Since the ultimate intention is to be able to detect the pairings from the near field, a reasonable first step is to generate various kinds of conditionally averaged near field pressure waveforms based on different sampling conditions with the goal of selecting a subprocess suggestive of a vortex pairing. Accordingly, an x-wire probe was placed in the shear layer at the position (x/D = 2.0, r/D=.60), which is slightly towards the entrainment side of the turbulence peak and at an axial station where the coherence across the jet is still high. Two microphones were placed in the near field of the jet at the same downstream location, x/D=2.0. One was positioned immediately next to the x-wire probe and the other 180° opposite. The turbulence and near fields were recorded simultaneously, digitized, and various sampling conditions derived from the u,v record were investigated. On the whole, the attempt was not very successful. The main difficulty is that the jet, unlike a boundary layer, is not constrained by fixed surfaces, and the spatial wandering of the jet probably obscures the subprocesses of interest. The types of trigger conditions investigated and the results are summarized:

1) Various kinds of VITA (Variable Interval Time Averages) averages of the sort pioneered by Kaplan and Laufer (1969) in connection with the turbulent sublayer were applied to both the u signal and the uv product signal, but produced no interesting educted signatures.

2) Positions (u,v) were selected in the hodograph plane that were associated with trajectories of high turbulent kinetic energy, and educed signatures were computed for the uv record as well as for the pressure records. The trajectories were computed by looking forward 10 time steps and backwards 10 time steps whenever the u,v record occupied the cell (u,v) being investigated. The kinetic energy was averaged simultaneously with the trajectories. No consistent trend was observed in either the educted pressure

signatures or in the educted uv signature.

3) Educted u and v signatures along with educted pressure signatures are shown in figure 48, and were educted from the triggering condition $(uv - \langle u \rangle \langle v \rangle)/u'v'$ greater than 1.5. The upper two curves are the educted u and v signals, the center curve is the ensemble averaged uv product, and the lower two curves are the near and far microphone signals. Note that there is a clear phase relationship between the conditionally averaged pressure signals and the condition of large uv product. However the time scale of the educted pressure waveform is clearly that of the mean structure, which implies that the trigger condition is sensitive to the mean structure rather than interactions between structures. This outcome is typical for the types of triggering conditions investigated.

7.4 Estimation of mean pairing locations

As things now stand the pairing process, clearly observable by visual techniques, can be detected only in the earliest stages of shear layer spreading. More sophisticated sampling techniques such as u,v space statistics have been ineffective in identifying the occurrence of pairings farther downstream.

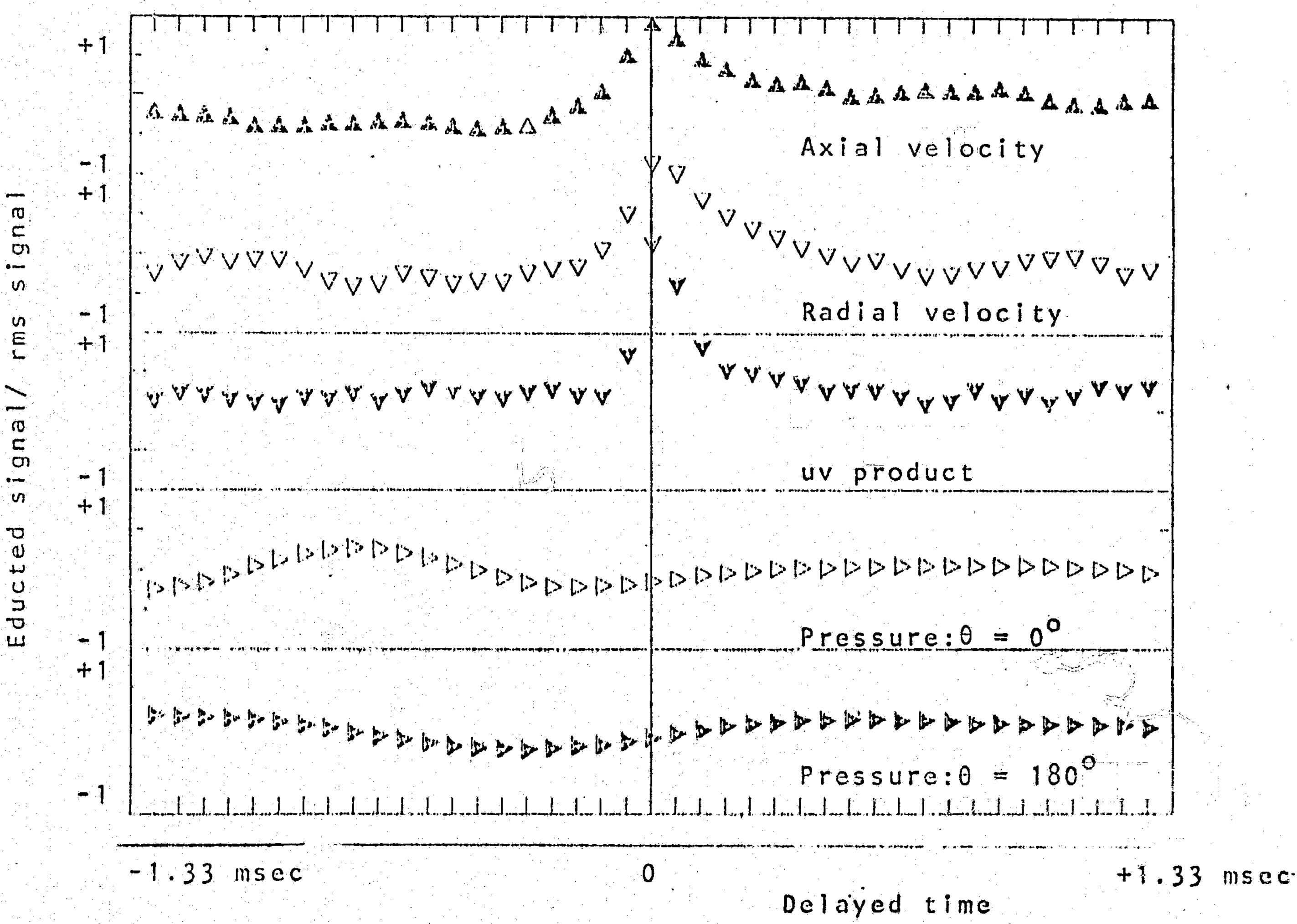

Figure 48. Educted near field pressure signatures: triggering from uv product inside mixing layer. $x/D = 2.0$, $r/D = 0.6$

It is instructive nevertheless to model the near field measurements according to the pairing hypothesis to deduce what the mean locations and variances of the pairings would have to be. If the near field time scales represent the periodicity of vortex ring passages, then the mean locations of the pairings can be deduced deduced directly from the time scales using conservation of waves. Within a given interval (x_1,x_2) the rate, $\dot{n}$, at which vortex rings disappear is

$$\dot{n} = f(x_1) - f(x_2) \tag{22}$$

where f(x) is the frequency of vortex ring passage past position x. If X_i is the mean location of the "i"th pairing, then half of the rings passing $x=X_i$ will have disappeared due to pairings before reaching $x=X_{i+1}$, the mean location of the "i+1"st pairing:

$$f(X_{i+1}) = \tfrac{1}{2}f(X_i) \tag{23}$$

From the two-point eductions across the shear layer it appears that the first pairing takes place at about x/D = .2. Then based on the wave counting measurements, the mean vortex passage frequency as a function of x is:

$$f(x) = f_o/x \tag{24}$$

It follows from equation (23) that

$$X_{i+1} = 2X_i \tag{25}$$

So based on this model the mean positions of the first seven pairings are summarized in table 2.

Pairing # n	Mean location Xn/D
1	.2
2	.4
3	.8
4	1.6
5	3.2
6	6.4
7	12.8

Table 2. Distribution of pairing locations

Since directional microphone measurements by Chu, Laufer, and Kaplan (1975) have localized the noise producing region of subsonic jets within the range four to ten diameters downstream, the point of this exercise is that two or at most three pairings would have to be responsible for most of the radiated noise if pairings are in fact the important acoustic sources.

According to the model, vortex pairing is the mechanism for the spreading of turbulent shear layers. The fact that the spreading is observed to be linear permits an estimate of the the variance associated with pairing locations. For the purposes of this crude estimate, the nth pairing is

X_n. The resulting shear layer thickness, $h(x)$, is:

$$h(x) = h_o\left(1+\sum_{n=1}^{\infty}2^{n-1}A_n\int_o^x \exp\{-(\xi-X_n)^2/2(\sigma\ell_n)^2\}\,d\xi\right) \qquad (26a)$$

$$A_n = \left(\int_o^{\infty}\exp\{-(\xi-X_n)^2/2(\sigma\ell_n)^2\}\,d\xi\right)^{-1} \qquad (26b)$$

ℓ_n = vortex spacing $X_{n+1} - X_n$, and σ^2 = variance in the pairing location as a fraction of the local spacing ℓ. Figure 49 shows the shear layer growth computed from equation (26) for three different values of the parameter σ. For values of σ less than .5 the spreading is not smooth, and for values greater than 1.5 the spreading is no longer linear. On the basis of these simple arguments it would appear that the dispersion in pairing location would have to be of the order of the mean distance between pairings, and that this distance would grow exponentially with downstream distance. This large "phase jitter" in pairing location relative to the mean structure would certainly account for the difficulty in detection.

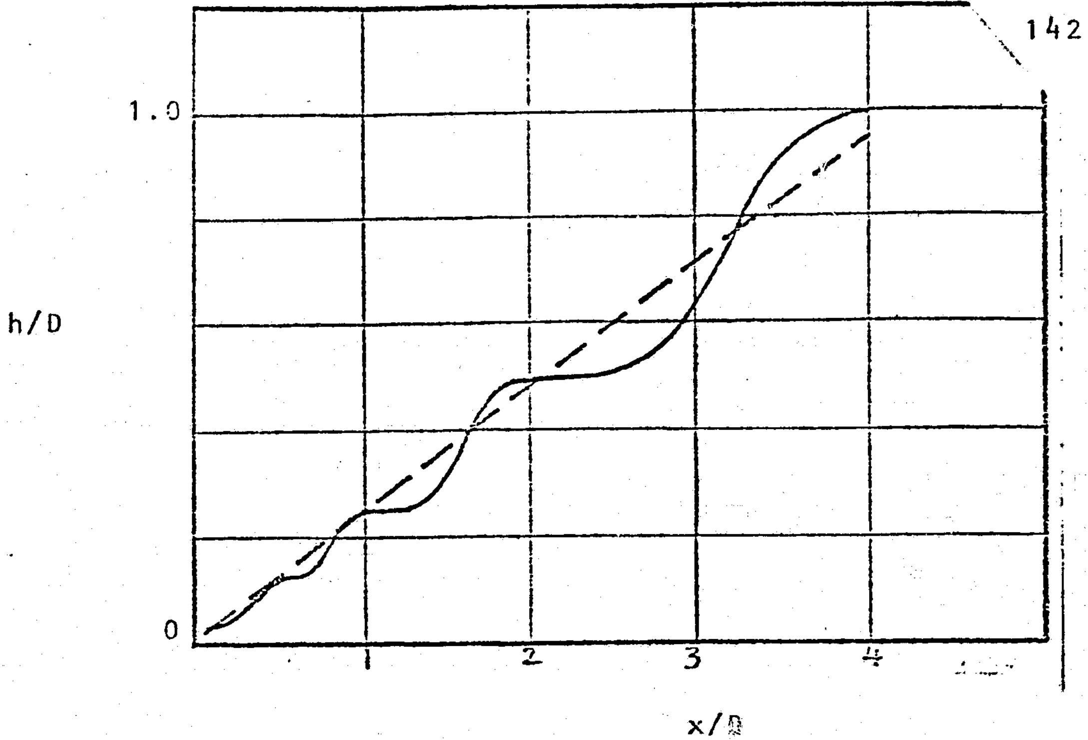

(a) σ = 0.2

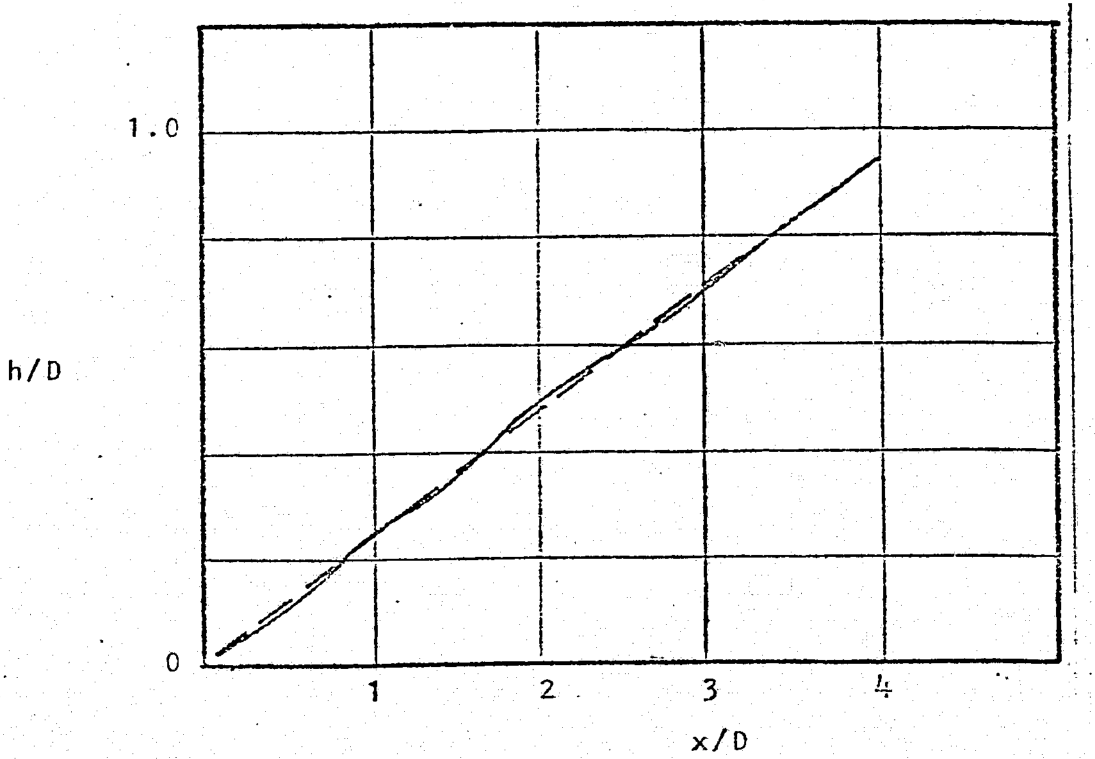

(b) σ = 0.5

Figure 49. Model shear layer spreading with parameter: variance in pairing location divided by spacing between pairings (σ).

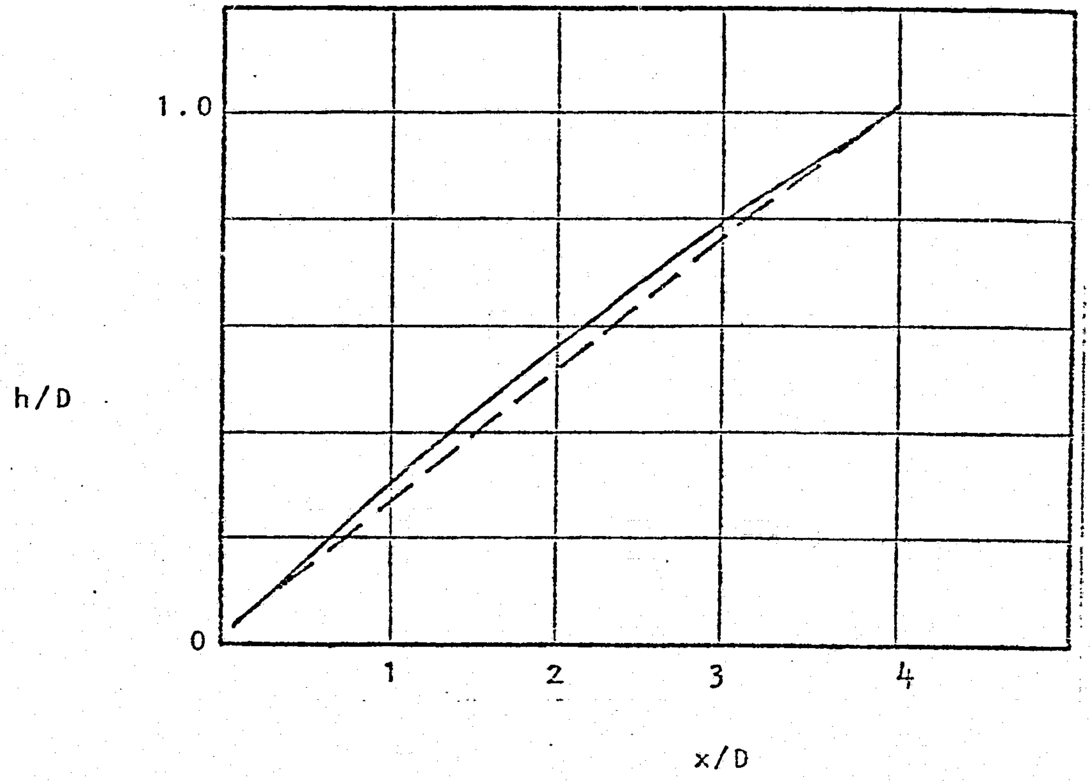

(c) σ = 1.0

Figure 49. Concluded.

8. CONCLUSIONS

1) Correlation methods are adequate for detecting the regularly spaced vortex rings along the potential core of the jet. Simple two point eduction techniques are adequate for detecting the initial one or two pairings near the nozzle exit. Even more sophisticated eduction techniques were unable to detect subsequent pairings from their near field signatures. Consequently the role played by vortex pairing in turbulent mixing layer spreading in moderate and high Reynolds number jets is still in question, as is the contribution of pairing to far field noise.

2) The near field autocorrelations indicate a fundamental change in mixing layer structure at the end of the potential core. In particular the decrease in length scale and total disappearance of near field time scale imply a breakdown of the regular structures observed upstream.

3) The transitional mixing region of the jet, which is observed to be the major noise source, is not remarkable in terms of overall statistical parameters such as turbulence levels, shear stress, or statistical 'noisiness'.

4) In terms of the distributive measures of DRIFT and DIFFUSION as defined in this paper, the jet turbulence

appears fairly deterministic. Stochastic models which consider the jet to be noise driven would be most valid for large axial and radial positions.

5) The hodograph plane description of turbulence is rich in statistical information both direct and implied. It seems like a promising pattern recognition tool, and is worthy of further development.

REFERENCES

A.B.C. Anderson (1955), "Structure and velocity of the periodic vortex-ring flow pattern of a pipe tone jet", Journal of the Acoustical Society of America, 27, 1048-1053

G.K. Batchelor, An Introduction to Fluid Mechanics, Cambridge University, 1967

P. Bradshaw, D.H. Ferriss, and R.F. Johnson (1964), "Turbulence in the noise-producing region of a circular jet", Journal of Fluid Mechanics, 19, 591-624

F.K. Browand, W.T. Chu, and J. Laufer (1975), "Exploratory experiments on the entrance effects in subsonic jet flows", USCAE Report 130, University of Southern California

S.C. Crow and F.H. Champagne (1971), "Orderly structure in jet turbulence", Journal of Fluid Mechanics, 48, 547-591

P.O.A.L. Davies, A.L. Yule, J.J. Bruun, and D.R.J. Baxter (1974), "Structure of turbulent jets - second annual report: time domain analysis of turbulent structure", Memorandum no. 506, University of Southampton

H.M. Fitzpatrick and R. Lee (1952), "Measurement of noise radiated by subsonic air jets", Report 835, The David W. Taylor Model Basin

W.L. Howes (1960), "Similarity of far noise fields of jets", NACA TR R-52

T. Jentes (1975), M.S. Thesis, University of Southern California

R.E. Kaplan and J. Laufer (1969), "The intermittently turbulent region of the boundary layer", Proceedings of the 12th International Congress of Applied Mechanics, Springer, 236

N.W.M. Ko and P.O.A.L. Davies (1971), "The near field within the potential core of subsonic cold jets", Journal of Fluid Mechanics, 50, 49-78

J.C. Lau, M.J. Fisher, H.V. Fuchs (1972), "The intrinsic structure of turbulent jets", Journal of Sound and Vibration, 22, 379-406

J. Laufer, W.T. Chu, and R.E. Kaplan (1975), "Axial source strength distribution in subsonic jets", USCAE Report 129, University of Southern California

J.C. Laurence (1955), "Intensity, scale, and spectra of turbulence in mixing region of free subsonic jet", NACA TN 3561

R. Lee (1953), "Free field measurements of sound radiated by subsonic air jets", Report 868, The David W. Taylor Model Basin

M. Lessen (1949), "On the stability of the free laminar boundary layer between parallel streams", NACA TN 1929

H.W. Liepmann and J. Laufer (1947), "Investigation of free turbulent mixing", NACA TN 1257

M.J. Lighthill (1952), "On sound generated aerodynamically: I general theory", Proceedings of the Royal Society, A211, 564-578

E. Mollo-Christensen (1967), "Jet noise and shear flow instability seen from an experimenter's viewpoint", Journal of Applied Mechanics, Transactions of the ASME, 34, 1-7

A. Powell (1964), "Theory of vortex sound", Journal of the Acoustical Society of America, 36, 177-195

D.O. Rockwell and W.O. Niccolls (1972), "Natural breakdown of planar jets", Journal of Basic Engineering, Transactions of the ASME, D94, 720-730

V.G. Rollin (1958), "Effect of jet temperature on jet noise generation", NACA TN 4217

J.M. Tyler and E.C. Perry (1954), "Jet noise", SAE preprint no. 287

R.V. Waterhouse and R.O. Berendt (1958), "Reverberant chamber study of the sound power output of subsonic air jets", Journal of the Acoustical Society of America, 30, 114-121

W.W. Willmarth and S.S. Lu (1972), "Structure of Reynolds stress near the wall", NATO-AGARD Conference

Proceedings *13*, London

C.D. Winant and F.K. Browand (1974), "Vortex pairing: the mechanism of turbulent mixing-layer growth at moderate Reynolds number", *Journal of Fluid Mechanics, 63*, 237-256

APPENDIX A

X-WIRE PROBE CALIBRATION

A.1 Kings law approximation

One point becomes obvious from the joint probability densities measured in chapter 6: the flow spends a considerable fraction of time at rather large flow angles. This fact makes the calibration procedure a very important part of x-wire measurements.

King's law of cooling relates the voltage signal, e(t), of a constant temperature hot wire probe to the velocity component normal to the wire:

$$e^2 = A + B\sqrt{u \sin\alpha + v \cos\alpha} \tag{A1}$$

where u and v are the axial and radial velocities, α is the angle of the wire relative to the x-axis, and A and B are constants of calibration. Equation (A1) can be inverted, yielding:

$$u = a_1 + a_2 e^2 + a_3 e^4 + a_4 v \tag{A2}$$

where the coefficients a_i are functions of A, B, and α. In the case of an x-wire probe where there are two wires equation (A2) assumes the general form:

$$u = a_{i1} + a_{i2}e^2 + a_{i3}e^4 + a_{i4}v \qquad (A3)$$

where a_{ij} is the 'j'th coefficient of the 'i'th wire.

In practice, hot wire voltages, e_i, are recorded over a range of known u and v, produced by placing the probe in the parallel flow region of the jet near the exit plane and then yawing the probe through known angles. Enough calibration points are recorded so that the set of equations (A3) are overdetermined. The equations are least squares fitted to the data to determine the "best fit" coefficient matrix (a_{ij}). Once the coefficients are determined, turbulent hot wire signals $e_1(t)$ and $e_2(t)$ can be linearized to produce velocity records u(t) and v(t):

$$u = \frac{F_1 a_{24} - F_2 a_{14}}{a_{24} - a_{14}} \qquad v = \frac{F_2 - F_1}{a_{14} - a_{24}} \qquad (A4)$$

where the polynomial

$$F_i = \sum_{j=1}^{3} a_{ij}(e_i^2)^{j-1} \qquad (A5)$$

$$= u - a_{i4}v$$

A set of measured calibration polynomials F_i are plotted against e_i in figure A1, and compared with the calibration data $(u-a_{i4}v)$. The trouble here is that the function F(e) always has a single minimum located at the

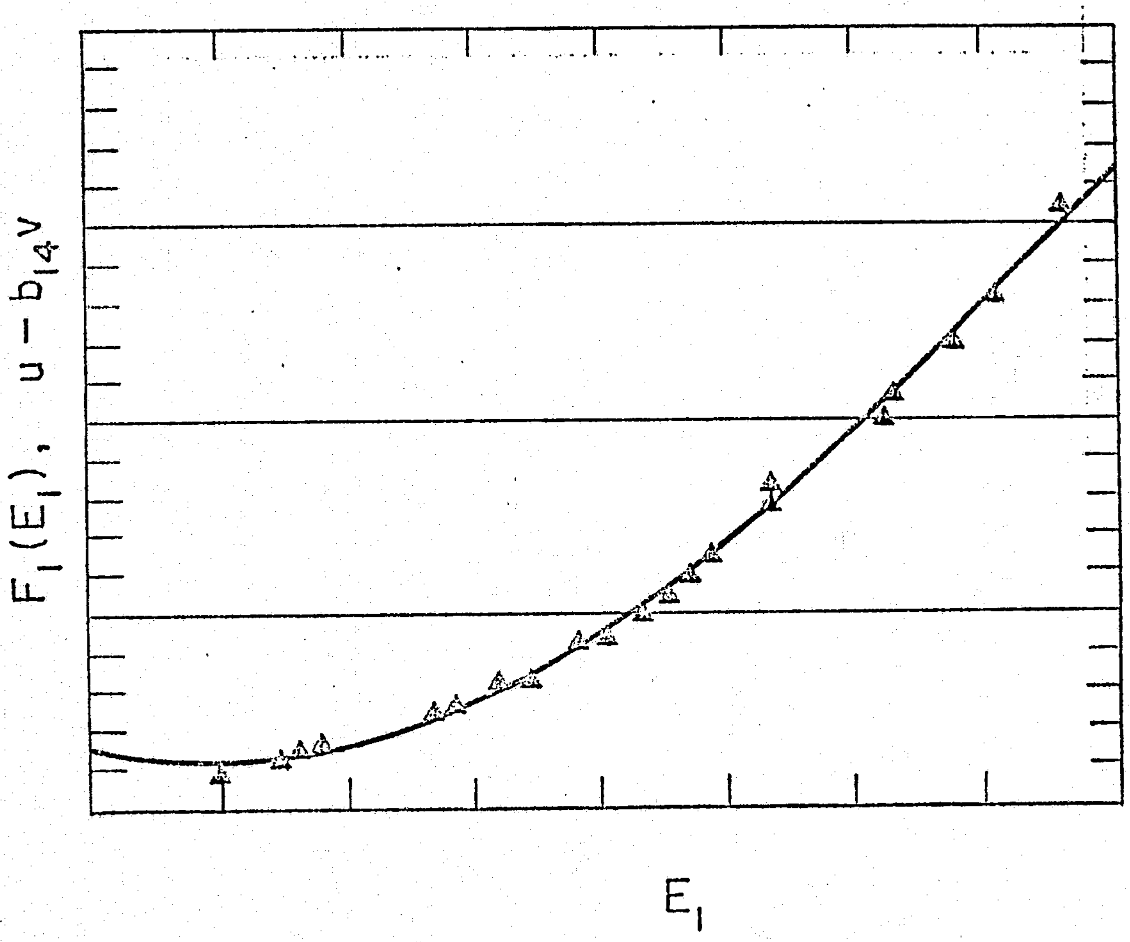

(a) Channel 1

Figure A1. Measured calibration polynomials

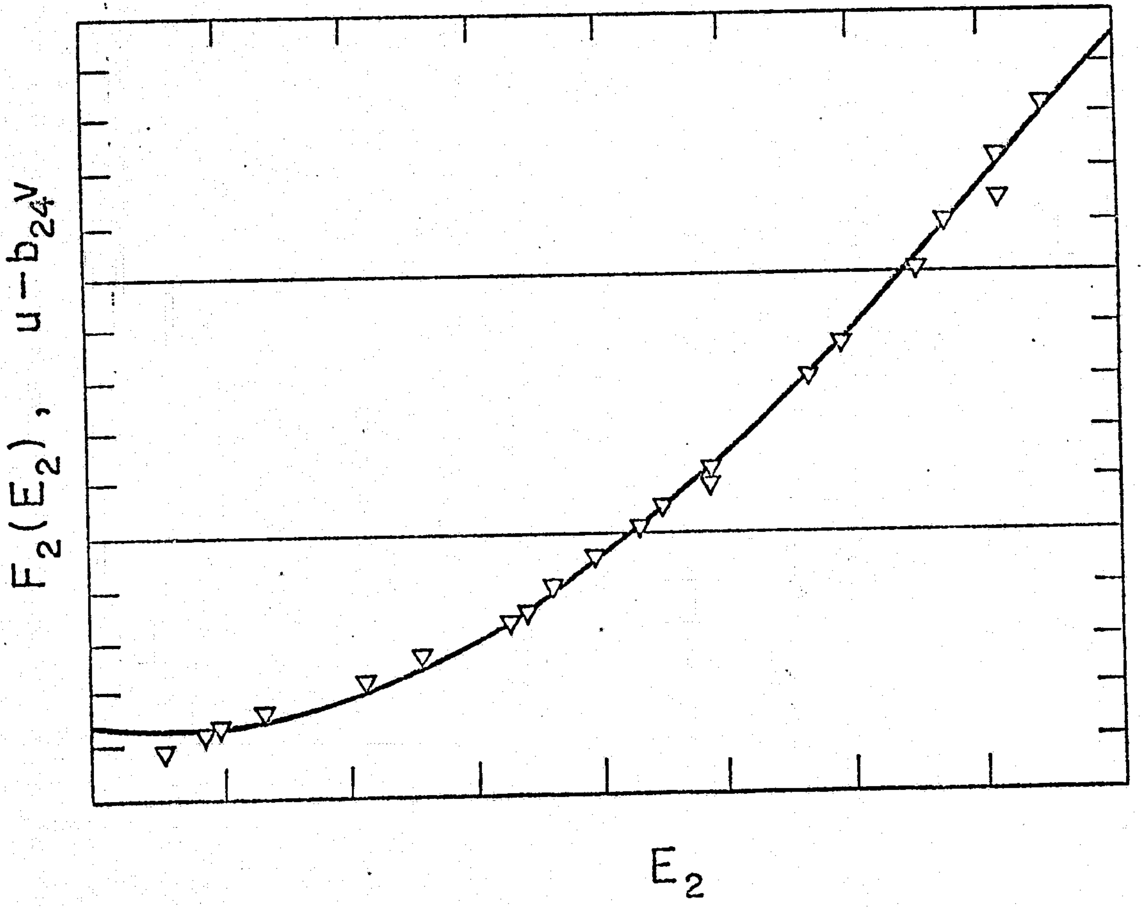

(b) Channel 2

Figure A1. Concluded.

smallest measured value of $(u-a_{i4}v)$, and unless calibration data points can be supplied where $(u-a_{i4}v) = 0$, the magnitude of $F(e)$ at its minimum will be greater than zero. Unfortunately $(u-a_4v)=0$ amounts either to zero flow velocity or to flow parallel to one of the wires. Either case is outside the range of validity of Kings law. This deficiency in the calibration is a serious one when its effect is assesed in the hodograph plane. The set of inequalities $(F_i)\text{min} > 0$ effectively displaces the origin from $(u,v) = (0,0)$ to

$$u_o = \frac{a_{24}(F_1)\text{min}-a_{14}(F_2)\text{min}}{a_{24}-a_{14}} \qquad (A6)$$

$$v_o = \frac{(F_2)\text{min}-(F_1)\text{min}}{a_{14}-a_{24}}$$

For the calibration polynomials in figure A1 the origin would be displaced to (u_o,v_o) = (10 fps, 0 fps), which can be enough to significantly distort the isoprobability contours of the joint probability $P(u,v)$.

A.2 Linearization subject to constraint

The problem of displaced origin can be alleviated by constraining $F_i(e_i)$ to pass through zero at its minimum. Instead of minimizing the sum of the variances, the quantities S_i^2 are defined

$$S_i^2 = \sum_{n=1}^{N} \{(u-a_{i4}v)_n - F_i(e_i)_n\}^2 + \lambda_i F_i(e_{i0}) \qquad \text{(A7)}$$

where the 'n' summation is over the data, λ_i are undetermined multipliers, and e_{i0} is the location of (F_i)min. Each S_i^2 is minimized with respect to the coefficients a_{ij}, resulting in a set of linear equations which when inverted yield solutions of the general form (summation over repeated indices not implied):

$$a_{ij} = B_{ij} + \lambda_i C_{ij} \qquad \text{(A8)}$$

The multipliers λ_i are determined by substitution into the constraint $F_i(e_{i0})$ min = 0. In practice iteration is necessary to finally determine the set (a_{ij}).

The calibration polynomial obtained in this way is plotted in figure A2 along with the calibration data. The polynomial is now well behaved in that it does pass through zero at its minimum. However the fit itself has become unacceptably poor, exhibiting a mean deviation of about 4 fps.

A.3 Linearization subject to correction terms

The fit can be improved while avoiding the problem of origin shift by adding a correction term to the $F_i(e_i)$ polynomials, equation (A5). The correction term adds an

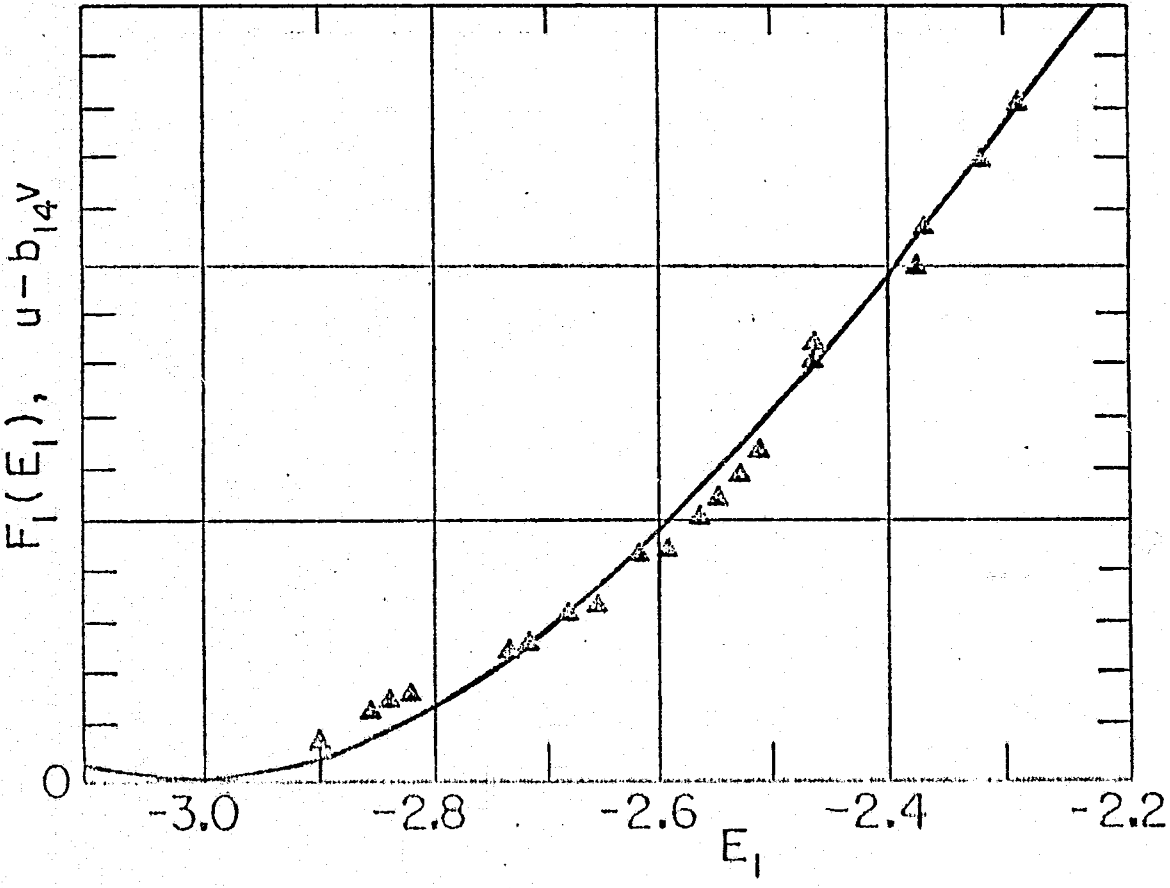

(a) Channel 1

Figure A2. Calibration polynomials subject to constraint: $F(c)_{min} = 0$.

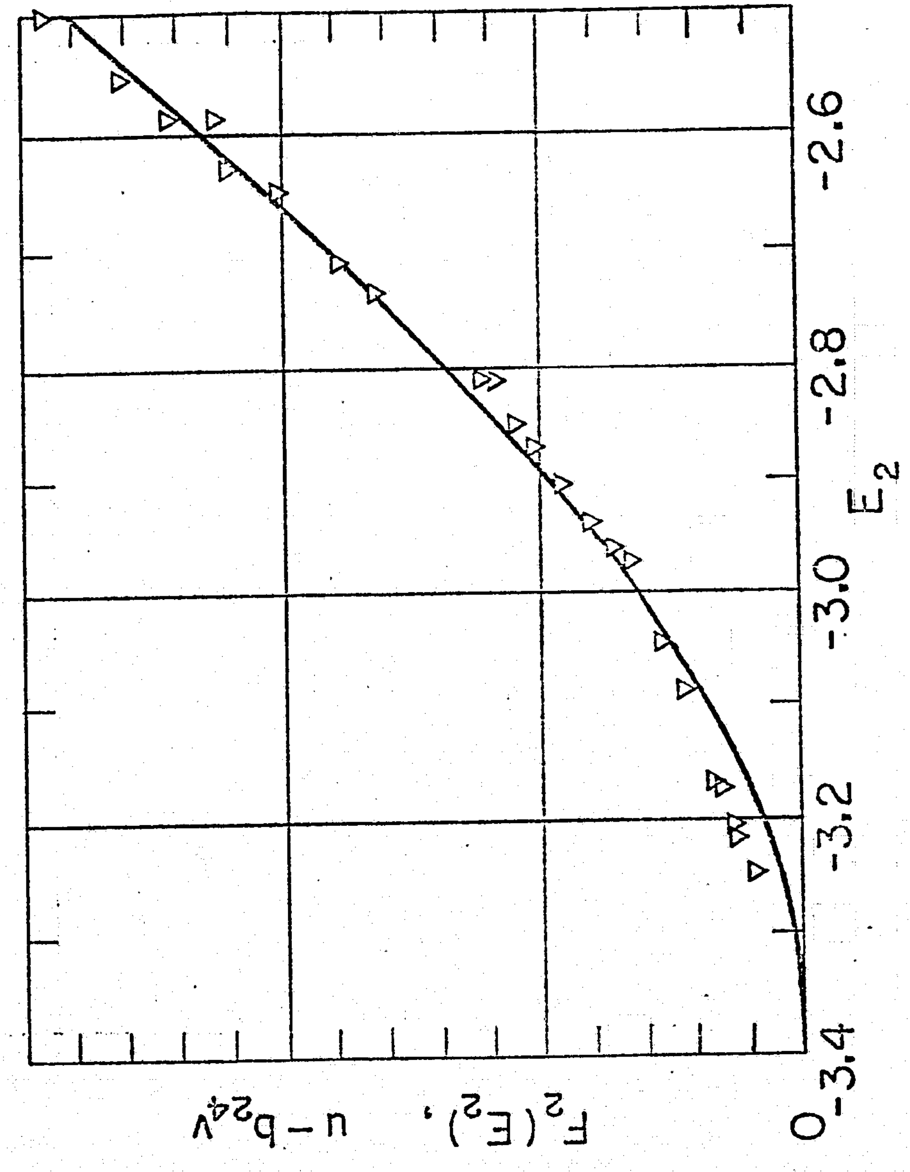

(b) Channel 2

Figure A2. Concluded.

extra degree of freedom, allowing the polynomial to pass through F=0 without constraint. A clue to the form of the correction term is provided by King's law. King's law, equation (A1), can be generalized to:

$$U\ f(\theta) = \left(\frac{e^2-A}{2}\right)^r \qquad (A9)$$

where U and θ are the magnitude and direction of the local velocity, and the exponent r is approximately 2. Empirically e^2 is always larger than A, so that the series expansion for equation (A9) is:

$$U\ f(\theta) = \left(\frac{e^2}{B}\right)^r \sum_{n=0}^{\infty} \frac{r!\ (-)^n\ (A/e^2)^n}{n!\ (r-n)!} \qquad (A10)$$

Consequently, the correction term should be of the order e^{-2}. The new calibration polynomial $H_i(e_i)$ is defined:

$$H_i(e_i) = a_{i1}/e_i^2 + a_{i2} + a_{i3}e^2 + a_{i4}e^4$$

$$= u - a_{i5}v \qquad (A11)$$

The measured calibration polynomials $H_i(e_i)$ are shown in figure A3 along with the data used in the curve fitting. This method produced an acceptable fit (mean deviation = 2 fps), and eventually passes through zero. However the slope becomes quite shallow near $H_i(e_i) = 0$. The slope is steeper if a correction term of the order e^6 is selected instead of e^{-2}. Although such a correction term is not motivated by King's law it has the same effect as the e^{-2} correction,

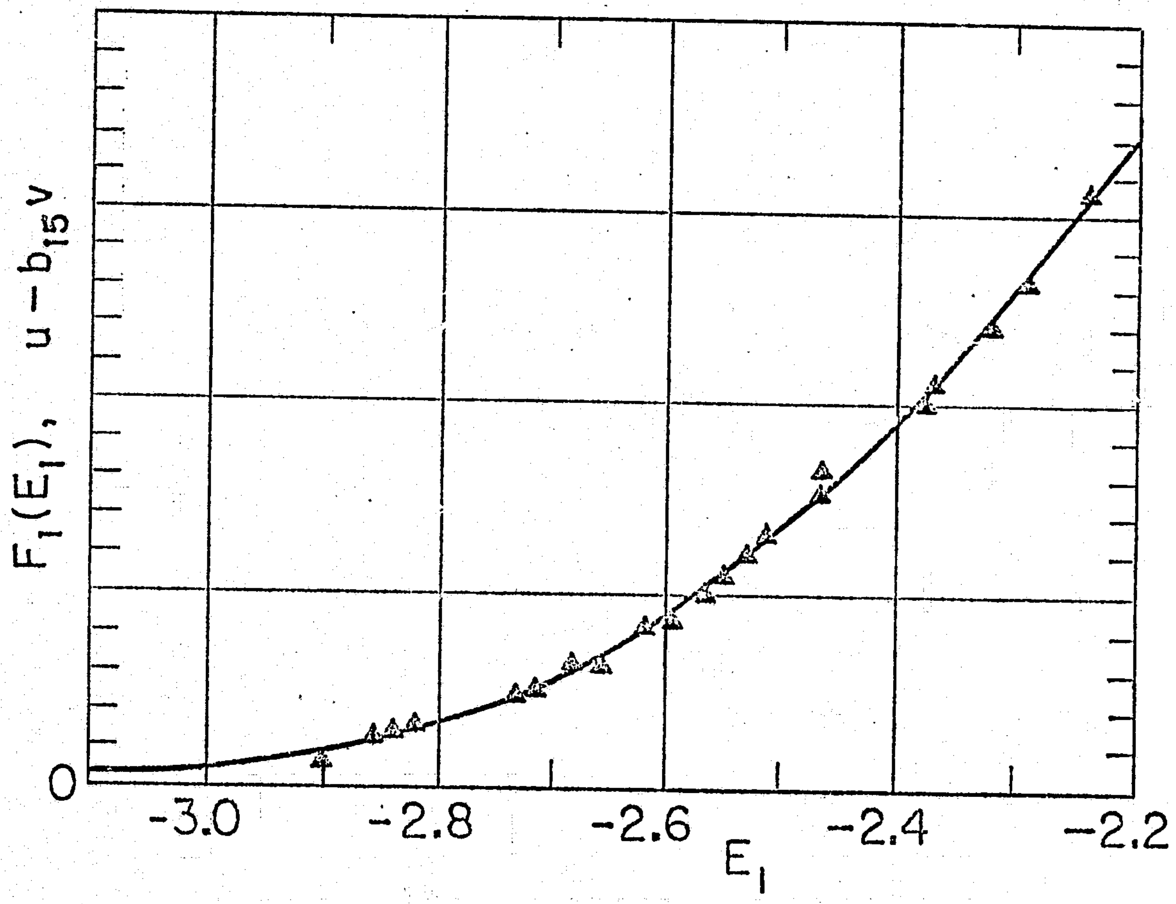

(a) Channel 1

Figure A3.. Calibration polynomials with correction term: $0(e^{-2})$

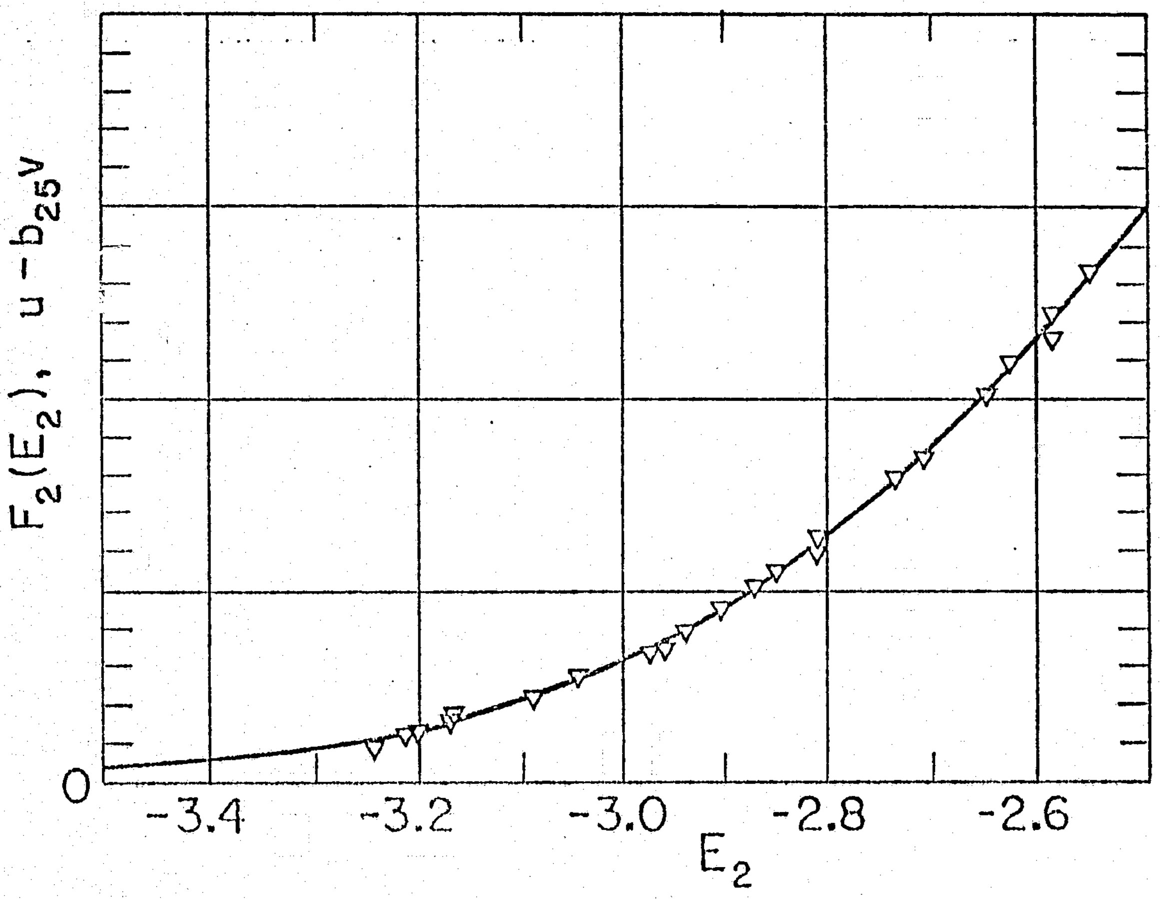

(b) Channel 2

Figure A3. Concluded.

namely it adds an extra degree of freedom to the curve fit. The calibration polynomials are redefined:

$$H_i(e_i) = a_{i1} + a_{i2}e^2 + a_{i3}e^4 + a_{i4}e^6 \qquad \text{(A12)}$$

$$= u - a_{i5}v$$

The resulting fit shown in figure A4 is the polynomial that was finally used in linearizing the x-wire signals to produce the joint statistics discussed in the body of this paper.

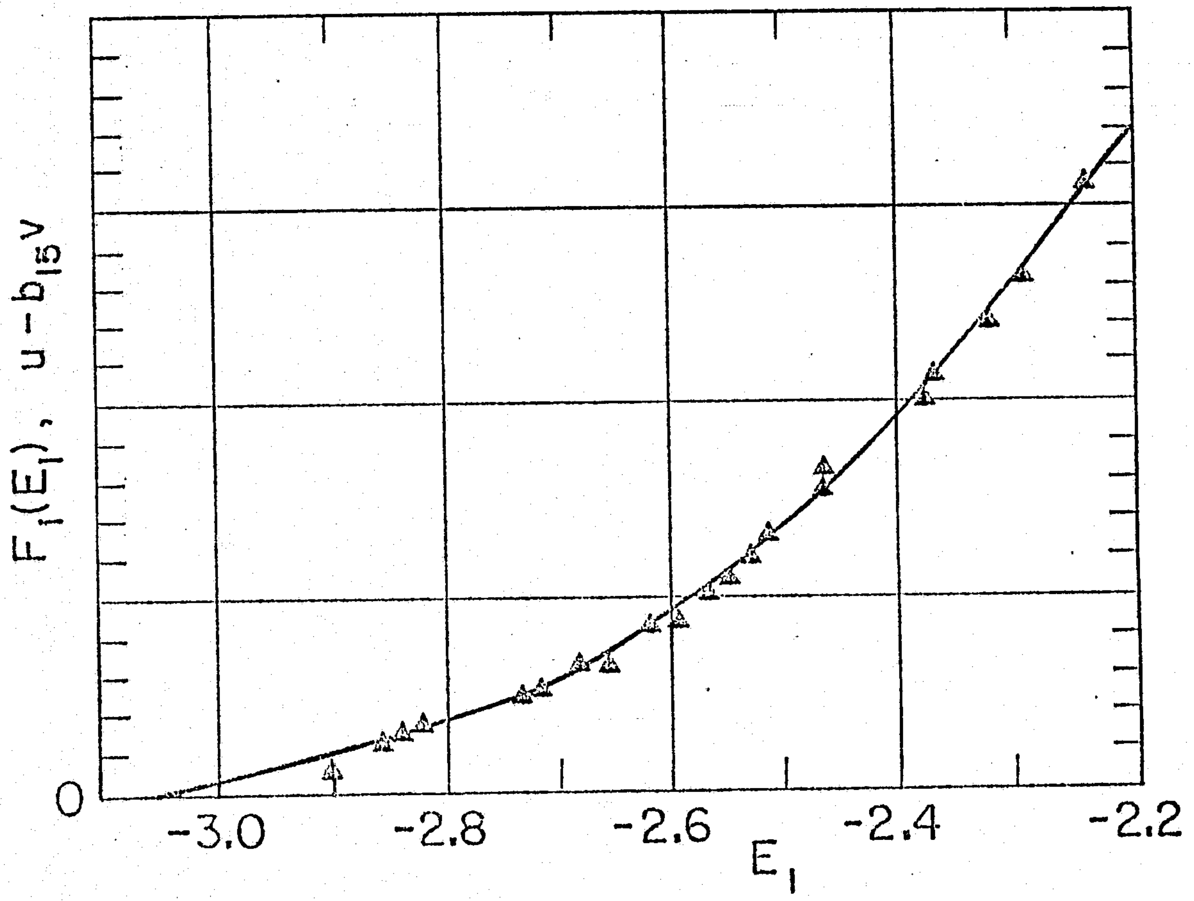

(a) Channel 1

Figure A4. Calibration polynomials with correction term: $O(e^6)$

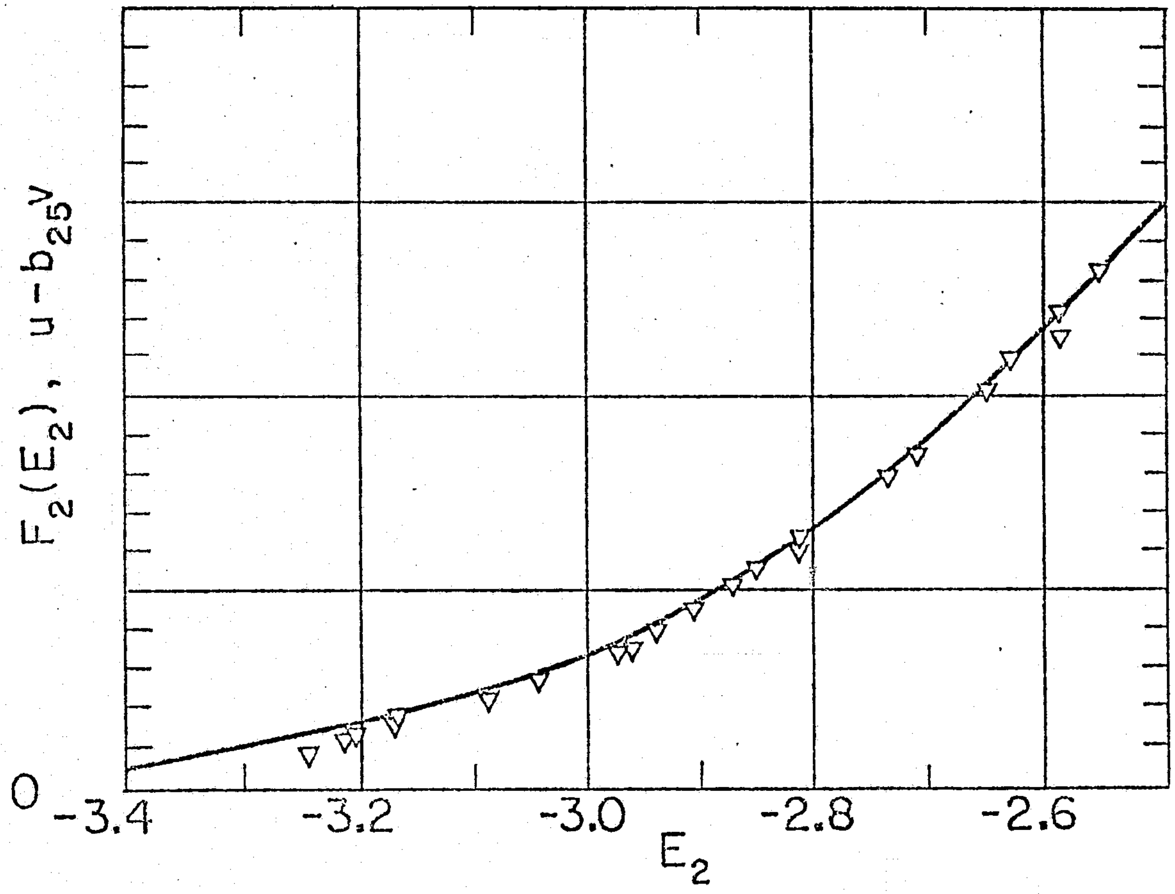

(b) Channel 2

Figure A4. Concluded.